Department of Physics and Astronomy
Heidelberg University

Bachelor Thesis in Physics
submitted by

Phil Lennart Stahlhut

born in Böblingen (Germany)

June 2023

Performance test of the KF Particle package for open heavy-flavour baryon reconstruction with ALICE

This Bachelor Thesis has been carried out by Phil Lennart Stahlhut at the
Physikalisches Institut of the University of Heidelberg
under the supervision of
Prof. Dr. Silvia Masciocchi

Abstract

The study of charm baryon production is crucial to understand charm hadronisation processes in a parton-rich environment. In order to extract signal even in low transverse momentum (p_{T}) regions where the signal-to-background ratio is rapidly decreasing, a precise reconstruction of the entire decay chain is of upmost importance.

The Kalman Filter (KF) Particle package gives a fast reconstruction of complex decay topologies providing a full description of the decay particle both at its production and decay vertex. It is suitable even for high-density track environments. In addition to that, the KF Particle package supports the use of geometrical, mass and topological constraints in the reconstruction process and includes the complete treatment of tracking and vertexing uncertainties.

In this work, the KF Particle package was used to reconstruct the Ξ_{c}^{+} baryon from its decay to $\Xi^{-}\pi^{+}\pi^{+}$ in simulated proton-proton collisions at a centre-of-mass energy of $\sqrt{s}$ = 13 TeV in the ALICE detector at the LHC. In this thesis, the effect of geometrical, mass and topological constraints on the secondary vertex, p_{T} and mass resolution of the reconstructed Ξ_{c}^{+} baryon will be demonstrated.

Zusammenfassung

Messungen des Produktionswirkungsquerschnitts von Baryonen mit Charm-Anteil sind wichtig für das Verständnis von Hadronisierungsmechanismen von Charm-Quarks. Um ein Signal auch bei geringen Transversalimpulsen, bei denen das Verhältnis vom Signal zum kombinatorischen Hintergrund rapide abnimmt, zu detektieren, ist eine präzise Rekonstruktion der gesamten Zerfallskette entscheidend.

Das Kalman Filter (KF) Particle Softwarepaket gewährleistet selbst bei komplexen Zerfallstopologien eine schnelle Rekonstruktion eines zerfallenen Teilchens sowohl an dessen Produktions- als auch Zerfallsvertex. Es eignet sich auch für Bereiche mit hohen Teilchendichten und führt eine vollständige Fehlerabschätzung der zu bestimmenden Parameter durch. Darüber hinaus ermöglicht es Zwangsbedingungen an die Zerfallstopologie und die Masse von kurzlebigen Teichen zu stellen.

In dieser Arbeit wurde die Rekonstruktion des Ξ_c^+-Baryons mit Hilfe des KF Particle Pakets anhand des Zerfalls $\Xi_c^+ \to \Xi^-\pi^+\pi^+$ in simulierten Proton-Proton Kollisionen bei einer Schwerpunktsenergie von $\sqrt{s} = 13\,\text{TeV}$ im ALICE Detektor untersucht. Dabei werden die Auswirkungen von Bedingungen an die Zerfallstopologie und die Masse von Tocherteilchen auf die Auflösung des Zerfallvertex sowie des Transversalimpuls- und Massenspektrum des Ξ_c^+ Baryon untersucht.

Contents

1 Motivation

High-energy hadronic collisions are used to study the fundamental nature of strongly interacting matter and characterise its underlying theory of *Quantum Chromodynamics* (QCD). Hadrons containing charm (c) or beauty (b) quarks are known as *heavy-flavour* hadrons and measurements of their production in proton-proton (pp) collisions provide an important test of pertubative QCD. Moreover, they serve as a valuable reference for production measurements in heavy-ion collisions, where heavy-flavour hadrons can be used as a sensitive probe for the *quark-gluon plasma* (QGP), a hot nuclear matter state predicted at extremely high temperatures and/or densities.

The production cross section ratio of charmed baryons and mesons is sensitive to the so-called *fragmentation functions*, which describe the probability of a charm quark to hadronise into a specific hadron species and have been assumed to be universal across different collision systems. However, measurements at the LHC in pp and p-Pb collisions tend to indicate a deviation from measurements in e^+e^- and e^-p collisions and thus a non-universal charm fragmentation. In order to systematically study the modification of the fragmentation for different collision systems, the measurements need to be as precise as possible over the entire p_T range. Extending the measurements of the production cross section to low p_T would also allow for a more precise measurement of the total charm and beauty cross section[7].

The latest p_T-differential cross section measurement of the Ξ_c^+ baryon [7] (see fig. 1) in pp-collisions at a centre-of-mass energy of $\sqrt{s} = 13\,\mathrm{TeV}$ recorded by the ALICE detector was performed in the transverse momentum range of $3 < p_\mathrm{T} < 12\,\mathrm{GeV}/c$. It used the *KF Particle* package, developed for the CBM experiment at GSI and implemented for ALICE, for the full reconstruction of the Ξ_c^+ decay chain. The reconstructed particle candidates were selected based on the decay topology using the machine learning tool *XGBoost*. Nevertheless, it was not possible to extract signal with high significance from the invariant mass spectrum for $2 < p_\mathrm{T} < 3\,\mathrm{GeV}/c$. For low transverse momentum, the production rates, especially for light primary particles such as pions, kaons and protons, increase dramatically. The event multiplicity is even much higher in heavy-ion collisions. Selecting the right daughter tracks coming from a heavy-flavour decay from thousands of primary tracks is very challenging [7].

In this thesis, a systematic study of the application of mass and topological constraints in the reconstruction of a heavy-flavour decay chain is presented. The effects on the secondary vertex, mass and p_T resolution are shown such that the candidate selection and background rejection can be improved, possibly enabling the analysis of heavy-flavour hadrons for low p_T and heavy-ion collisions.

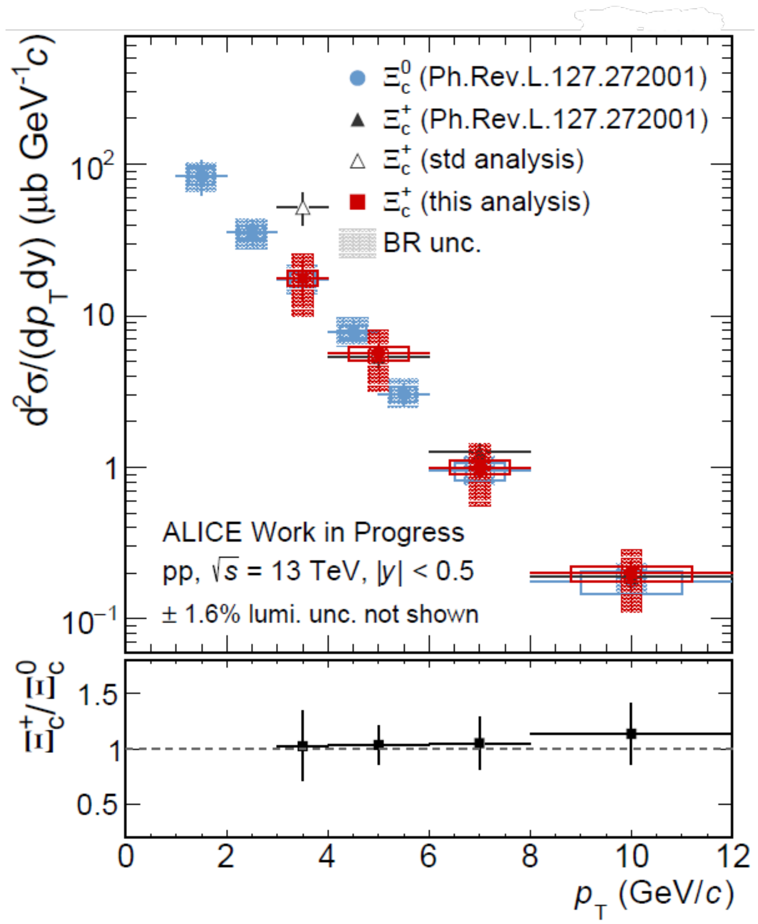

Figure 1: p_T differential cross section of prompt Ξ_c^+ and Ξ_c^0 baryons in pp collisions at $\sqrt{s} = 13\,\text{TeV}$. The Ξ_c^0 production cross section (blue) was obtained from a combined measurement of $\Xi_c^0 \to \Xi^- e^+ \nu_e$ $\Xi_c^0 \to \Xi^- \pi^+$ in the transverse momentum interval $1 < p_T < 12\,\text{GeV}/c$. The black full markers show the published results of the analysis of $\Xi_c^+ \to \Xi^- \pi^+ \pi^+$ in the range $4 < p_T < 12\,\text{GeV}/c$ using standard reconstruction and analysis techniques. The unpublished attempt to extend the measurement to the $3 < p_T < 4\,\text{GeV}/c$ interval is depicted by the black open marker. The results of the analysis from [7] using the KF Particle package and XGBoost is shown by red markers. The obtained production cross section for $3 < p_T < 4\,\text{GeV}/c$ coincides with the published measurement for the Ξ_c^0 production cross section [7].

2 Tracking of charged particles in the ALICE detector

2.1 Overview of the ALICE detector

ALICE (A Large Ion Collider Experiment) is a general-purpose heavy-ion detector at the Large Hadron Collider (LHC) which focuses on the physics of strongly interacting matter. Its dimensions are $16 \times 16 \times 26\,\mathrm{m}^3$ and it weighs in total approximately 10 000 t [1]. It consists of a central barrel part designed to measure hadrons, electrons and photons and a forward muon spectrometer. The entire central barrel module is embedded in a large solenoid magnet reused from the L3 experiment at LEP which provides a magnetic field of 0.5 T. The forward muon spectrometer consists of a dipole magnet, absorbers as well as tracking and triggering chambers [1].

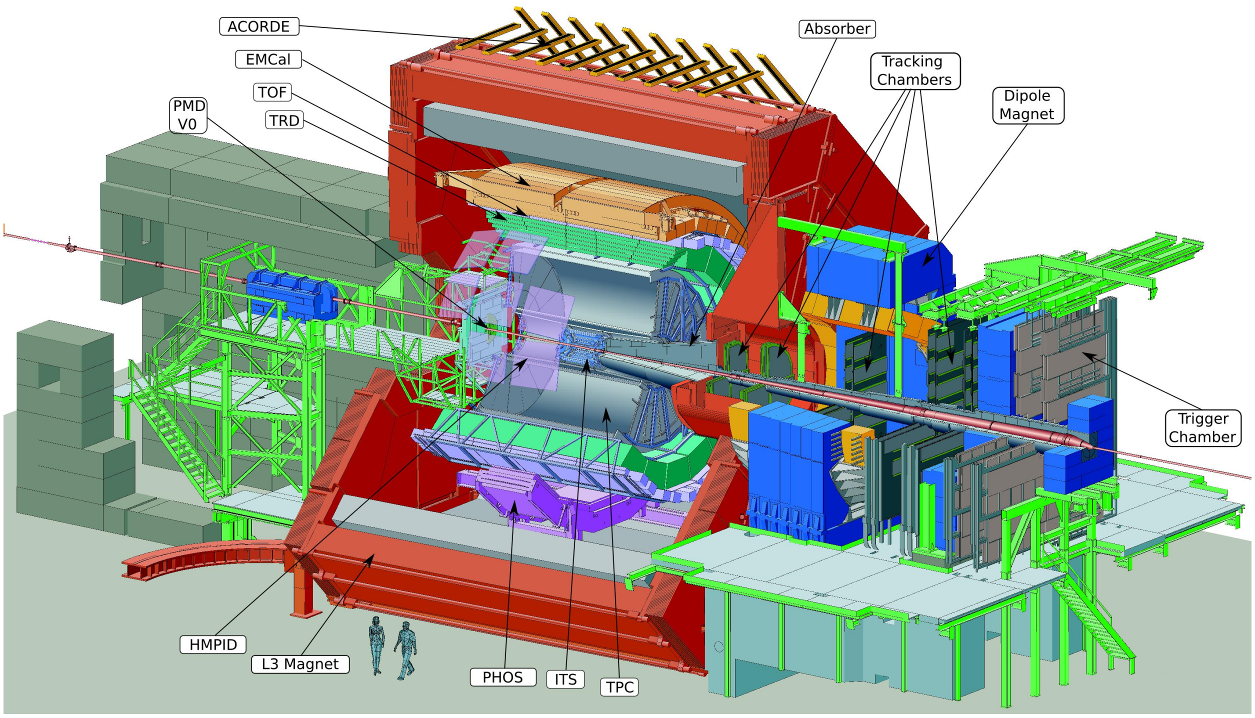

Figure 2: The ALICE experiment at the CERN LHC [10].

In the following, a short description of the central barrel detectors and their main purpose is given, going radially from the inside out. The first four detectors cover the full azimuth, while the latter three share the outer cylindrical volume. Since data simulated for the ALICE setup in the data-taking period from 2016 to 2018, called *Run 2*, is used in the analysis, recent detector upgrades after 2018 are not considered.

- The *Inner Tracking System* (ITS) is a silicon vertex detector and composed of six tracking layers. The first two layers are Silicon Pixel Detectors (SPD), followed by two Silicon Drift Detectors (SDD) and two Silicon Strip Detectors (SDD). It is mainly used for the reconstruction of the *primary vertex* (PV), *secondary vertices* (SV) from heavy-flavour or strange particle decays and particle trajectories. It enables to track particles with momenta down to 80 MeV/c [6] and to improve the angle and momentum resolution for particles reconstructed by the other main tracking detector, the TPC (see below). The analogue readout of the four outer layers can be used for charged particle identification via measurement of the specific ionisation energy loss for low-momentum particles. The position, spatial resolution and main purpose of each ITS detector layer are listed in table 1.

Type	r [cm]	$\pm z$ [cm]	spatial resolution $r\phi$ [μm]	spatial resolution z [μm]	main purpose
pixel	3.9	14.1	12	100	tracking, vertexing
pixel	7.6	14.1	12	100	tracking, vertexing
drift	15.0	22.2	35	25	tracking, PID
drift	23.9	29.7	35	25	tracking, PID
strips	38	43.1	20	830	tracking, PID
strips	43	48.9	20	830	tracking, PID

Table 1: Overview of specifications of the individual ITS layers [1].

- The *Time-Projection Chamber* (TPC) is used for tracking and particle identification via the measurement of the specific ionisation energy loss dE/dx. It is 5 m [1] long and covers the cylindrical volume from $87 < r < 247$ cm [1]. The inner radius of the TPC is determined by the maximum acceptable track density, whereas the outer radius is defined by the length required for achieving a dE/dx resolution of better than $5 - 7\%$. The drift volume of 90 m^3 [1] is filled with a $\mathrm{Ne} - \mathrm{CO_2}$ mixture. The TPC is divided into two parts by a central cathode which is kept at a voltage of -100 kV [6]. Charged particles free electrons by ionising the TPC gas, which then drift towards the segmented end planes of the TPC. For the applied voltage and maximum drift distance of half of the TPC length, the maximum drift time of the electrons is about 90 μs [1]. Using the timing information of the signal to reconstruct the position along the beamline, the three-dimensional position of the charged-particle track can be reconstructed.

- The *Transition Radiation Detector* (TRD) is used to provide electron identification in the central barrel and consists of six layers of $\mathrm{Xe} - \mathrm{CO_2}$-filled gas chambers, each followed by a fibre/foam radiator. Above 1 GeV/c [1], transition radiation from electrons passing the fibre/foam radiator can be used together with the information from the specific energy loss in the gas mixture to differentiate pions from electrons. Below this momentum threshold, electrons can be identified via specific energy loss measurements in the TPC. The TRD is also used for tracking in the central barrel in order to improve the transverse momentum resolution at high momenta.

- The *Time-of-Flight* (TOF) detector is used for particle identification at intermediate momenta, below about 2.5 GeV/c for pions and kaons and up to 4 GeV/c for protons [1].

- The *Photon Spectrometer* (PHOS) is an electromagnetic calorimeter with high resolution and high granularity, which consists of dense scintillating $\mathrm{PbWO_4}$ crystals and is designed to measure photons.

- The *Electromagnetic Calorimeter* (EMCal) is a sampling calorimeter consisting of alternating layers of lead absorbers and scintillators. It is much larger than PHOS, but has a lower granularity and energy resolution. The EMCal is optimised to measure jet production rates and fragmentation functions in conjunction with the other charged particle tracking in the other central barrel detectors.

- The *High Momentum Particle Identification Detector* (HMPID) consists of ring imaging Cherenkov detectors with liquid $\mathrm{C_6F_14}$ radiator. It is used to improve the charged hadron identification towards higher momenta.

In addition to the central barrel detectors, there are also other smaller forward detectors such as the V0 detector, a plastic scintillator mainly used for triggering. For data taking in pp collisions, the so-called *minimum bias* trigger requiring signals in the V0 and, depending on the type of the trigger, the SPD is used. The other forward detectors and the muon spectrometer will not be discussed in detail [1, 6].

The ALICE coordinate system, defined as a right-handed orthogonal Cartesian coordinate system, is illustrated in fig. 3: Its origin lies at the Interaction Point (IP) 2 of the LHC with the z-axis aligned parallel to the magnetic field and mean beam direction. The x-axis points horizontally to the centre of the LHC, the y-axis vertically upwards [6]. Therefore, the central barrel tracking detectors are totally radially symmetrical in the xy-plane.

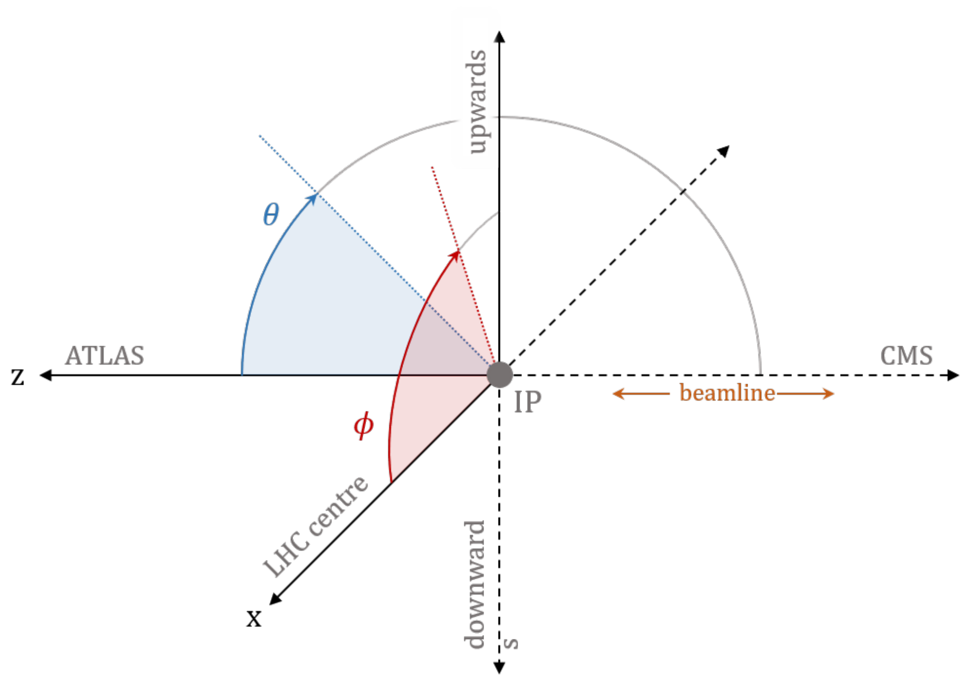

Figure 3: Sketch of the ALICE coordinate system [8].

2.2 Central Barrel Tracking

The procedure of finding tracks in the central barrel starts with the clusterisation step: The data of each detector are separately converted into *clusters* characterised by the positions, signal amplitudes, signal times and their corresponding errors. These clusters are interpreted as the crossing point of an associated track. Using the two innermost ITS layers, the interaction vertex is preliminarily determined as the space point to which the maximum number of tracklets, which are lines defined by two clusters in each SPD layer, converge. The track finding and fitting is then performed in three stages and follows an inward-outward-inward scheme.

The first inward stage starts with finding tracks in the TPC. Since the TPC readout chambers have 159 tangential pad rows, a track can produce 159 clusters within the TPC volume in the ideal case. Track seeds are built from two TPC clusters at large radii and the vertex point. In order to reconstruct tracks which do not originate from the interaction vertex, additional track seeds are built from three TPC cluster at large radii without the vertex constraint. These seeds are then propagated inward and updated with the nearest cluster fulfilling a certain proximity cut using the Kalman filter algorithm (see section 3.2). Only tracks with at least 20 clusters are accepted. Based on the specific energy loss in the TPC gas, a preliminary particle identification is performed such that the most-probable mass can be used for the ionisation energy loss correction calculations in the following tracking steps.

The TPC tracks are then propagated to the outermost ITS layer and used as seeds for track finding in the ITS. These seeds are again propagated inward and updated at each ITS layer by all clusters within a proximity cut with the Kalman filter algorithm. As a result, each TPC track produces a tree of track hypotheses in the ITS which are sorted according to their reduced χ^2. The candidates with the highest quality from each tree are checked for cluster sharing among each other. If shared clusters are found, an attempt is made to find alternative candidates in the involved trees. Finally, the highest quality candidate from each hypothesis tree is added to the reconstructed event. As the reconstruction efficiency in the TPC drops at low transverse momentum due to energy loss and multiple scattering in the detector material (see section 2.3), a standalone ITS reconstruction is performed with the clusters that were not used in the ITS-TPC tracks. The corresponding seeds are created from two cluster in the three innermost ITS layers and the interaction vertex point, propagated to the outer ITS layers and updated with clusters within a proximity cut. All of the track hypotheses are refitted by a Kalman filter and the track with the best fit χ^2 is accepted.

After the reconstruction in the ITS is completed, all tracks are extrapolated to their *point of closest approach* (PCA) to the preliminary interaction vertex. Using the clusters found at the previous stage, the tracks are refitted by the Kalman filter in the outward direction. At each step, the track length integral and the time of flight expected for different particle species (e, μ, π, K, p) are updated. Once the track reaches the outer layers of the TPC, an attempt is made to match tracks reaching the TRD and possibly the TOF with tracklets in the TRD and TOF respectively. The track length integration and time-of-flight calculation used for particle identification are stopped at this point. The tracks are propagated further for matching with signals in the calorimeters and HMPID. Finally, all tracks are propagated inwards from the outer radius of the TPC and refitted with the previously found clusters in the TPC and ITS.

Global tracks reconstructed in the ITS and TPC are used after the track fit to determine the interaction vertex with a higher precision. Therefore, the tracks are extrapolated to the point of closest approach to the nominal beam line. After removing far outliers, a precise vertex fit is performed. The transverse vertex position is improved by adding the so-called *diamond constraint*: The nominal beam position is added as an independent measurement with errors corresponding to the transverse size of the luminous region.

Once the tracks and interaction vertex have been found, a search for photon conversions and *secondary vertices* from particle decays is performed. For this, tracks with a *distance of closest approach* (DCA) to the interaction vertex exceeding a certain minimum value are selected. So-called V^0 *candidates* are identified from unlike-sign pairs of such tracks passing certain cuts on their DCA and PCA. After finding V^0 candidates such as K^0_S and Λ^0, a search of cascade decays (e.g. Ξ^-) is performed by adding a secondary track within a certain proximity cut to a V^0 candidate. More complex secondary vertices from hadronic interactions are later reconstructed at the analysis level by identifying groups of two or more tracks originating from a common space point [6].

2.3 Multiple scattering

When a charged particle is traversing a medium, it is deflected by many small-angle scattering processes. The dominant interaction process is Coulomb scattering from the nuclei of the medium, but the strong interaction will also contribute hadronic projectiles. For many small-angle scatter processes, the net scattering angular distribution is Gaussian according to the central limit theorem. It states that the average of N independent random variables $x_1, ..., x_N$, which are each distributed according to a *probability density function* (PDF) with finite variance, can be approximated by a Gaussian distribution in the limit of $N \to \infty$ regardless of the underlying PDFs. However, so-called *hard* scatter events produce non-Gaussian tails. The *root mean square* (rms) width of the central part covering 98% of the angular distribution projected into the plane perpendicular to the scattering medium is given by

$$\theta_{\mathrm{plane}}^{\mathrm{rms}} = \frac{13.6\,\mathrm{MeV}}{\beta c p} \cdot z \cdot \sqrt{\frac{x}{X_0}} \cdot \left[1 + 0.038 \ln\left(\frac{x z^2}{X_0 \beta^2}\right)\right] \propto \frac{1}{p}. \tag{1}$$

eq. (1) describes a particle with momentum p, velocity βc and charge number z passing through a medium of thickness x/X_0 in units of the radiation length. The radiation length of a material is defined as the mean distance over which a high-energy electron loses all but $\frac{1}{e}$ of its energy by bremsstrahlung. Hence, higher-momentum particles are less affected by multiple scattering than low-momentum particles [11, 4].

2.4 Tracks of charged particles in a magnetic field

The momentum vector of a charged particle can be determined by measuring its trajectory in a magnetic field. A particle with charge $q = z \cdot e$, mass m, velocity $\vec{v}$ and Lorentz factor γ will be deflected by the Lorentz force.

$$\vec{F}_{\mathrm{L}} = \dot{\vec{p}} = q \cdot \left(\vec{v} \times \vec{B}\right) \tag{2}$$

Using $\vec{p} = \gamma m \vec{v}$ and $\dot{\gamma} = 0$ since the magnetic field does not change the energy of the particle $E = \gamma m$, eq. (2) can be rewritten as

$$\dot{\vec{v}} = \frac{q}{\gamma m}\left(\vec{v} \times \vec{B}\right) \tag{3}$$

The solution of the differential equation in eq. (3) describes a rotating velocity vector $\vec{v}_{\mathrm{T}}$ in the plane perpendicular to the magnetic field $\vec{B}$ while the component parallel to $\vec{B}$ remains unchanged. Thus, the particle trajectory in space is given by a helix lying on the surface of a cylinder, which is aligned coaxially with the magnetic field. Its projection on the plane perpendicular to $\vec{B}$ describes a circle with radius

$$R = \frac{p_{\mathrm{T}}}{|q| \cdot B}. \tag{4}$$

Thus, the transverse and absolute momentum of the charged particle are given by the curvature radius R and the angle θ between the instantaneous momentum direction and the direction of the magnetic field:

$$\begin{aligned} p_{\mathrm{T}} &= |q| \cdot B \cdot R \\ p &= \frac{p_{\mathrm{T}}}{\sin\theta} \end{aligned} \tag{5}$$

Since ALICE uses a solenoid magnet with the direction of the magnetic field pointing along the beam axis, θ is simply the polar angle (see fig. 3) of the particle relative to the beam. The resolution of the measured transverse momentum can typically be described by the common parametrisation

$$\frac{\sigma_{p_{\mathrm{T}}}}{p_{\mathrm{T}}} = \sqrt{\left(\frac{\sigma_{p_{\mathrm{T}}}}{p_{\mathrm{T}}}\right)^2_{\mathrm{meas}} + \left(\frac{\sigma_{p_{\mathrm{T}}}}{p_{\mathrm{T}}}\right)^2_{\mathrm{scat}}} \equiv \sqrt{(a p_{\mathrm{T}})^2 + b^2}. \tag{6}$$

The first contribution scales linearly with p_{T} and is caused by the limited resolution of the position measurements, which complicates the measurement of small curvatures of the track corresponding to a high-momentum particle. The second, constant contribution is due to multiple scattering in the detector material and dominates the transverse momentum resolution for low p_{T} [3].

3 Event reconstruction with the KF Particle package

3.1 Event reconstruction in high-energy physics

An *event* is a snapshot recorded by a detector corresponding to one integration time of the detector at a trigger. More than one *collision* of particles can happen within this time interval, but these so-called *pileup events* are typically excluded from physics analysis. Modern experiments in high-energy physics operate at very high track densities with a particular interest for very rare signals. Therefore, the reconstruction of events in high-energy physics requires both high accuracy and high speed in order to analyse large amounts of data with a good probability of detecting these rare signals. The reconstruction of an event includes the finding and fitting of particle tracks, the alignment of detectors and the determination of the event vertices from reconstructed tracks among others. Many of those tasks involve fit problems which can be characterised as finding the most probable value of an unknown quantity using measurements of this quantity [2, 12].

The *Kalman filter* is a recursive fit algorithm for the analysis of linear discrete dynamic systems described by a set of parameters. It gives an optimal estimation of those parameters and can even be applied to nonlinear fit problems provided the model describing the system has been linearised in advance. The most common application of the Kalman filter in high energy physics is the fit of tracks of charged particles. The trajectory of a charged particle is affected by multiple scattering and energy losses by ionisation and excitation in the detector material as well as non-homogeneities of the magnetic field in the detector. Using the least squares method to fit the particle trajectory, it is almost impossible to take all these effects into account since new parameters have to be introduced and fitted for every effect. In contrast, these effects can be easily treated by the Kalman filter as the measurements in high-energy physics experiments are usually done by different sub-detectors separated in space: The particle track is linearised and effects of the detector material are added only in the neighbourhood of each measurement. All the nonlinear effects can be taken into account when transporting a particle from one measurement to the next. In addition to that, measurements can be added and removed independently allowing to refine the estimates of the parameters without repeating the entire fit procedure. This makes the use of the Kalman filter natural for the reconstruction of high-energy physics events [2, 12].

3.2 The Kalman filter algorithm

Let the *state vector* $\mathbf{r}^t$ be the vector of the parameters that should be estimated by the fit algorithm. The so-called *estimator* is the function of the data sample that returns the estimate of the state vector. In practice, estimators can be defined by more or less complex mathematical procedures or numerical algorithms. The goal of the fit procedure is then to find the best linear unbiased *estimator* $\mathbf{r}$ of the *state vector* $\mathbf{r}^t$ according to a given set of measurements $\{\mathbf{m}_k\}_{k=1,\dots,n}$. The properties of this desired optimal estimator are defined in the following way:

- *unbiased*: The mean value of the error of the estimator $\boldsymbol{\epsilon_r} = \mathbf{r} - \mathbf{r}^t$ is $\langle \boldsymbol{\epsilon_r} \rangle = 0$.
- *linear*: The estimator depends linearly on the measurements $\mathbf{m}_k$.
- *best*: The estimator has the minimal mean squared error $\sigma_{\mathbf{r}}^2 = \langle \boldsymbol{\epsilon_r}^{\mathrm{T}} \cdot \boldsymbol{\epsilon_r} \rangle$ among all other estimators.

Here $\langle . \rangle$ denotes the mathematical expectation value [2, 4].

First of all, it is assumed that each measurement $\mathbf{m}_k$ depends linearly on the state vector $\mathbf{r}^t$:

$$\mathbf{m}_k = \mathrm{H}_k \cdot \mathbf{r}^t + \boldsymbol{\eta}_k \tag{7}$$

H_k is a known linear operator represented by a matrix and called *model of measurement*. The *measurement errors* $\boldsymbol{\eta}_k$ are random variables each fulfilling the following assumptions:

$\langle \boldsymbol{\eta}_k \rangle = 0$	$\forall k$	unbiased
$\langle \boldsymbol{\eta}_k \cdot \boldsymbol{\eta}_k^{\mathrm{T}} \rangle = \mathrm{V}_k$	$\forall k$	covariance matrix is known
$\langle \boldsymbol{\eta}_k \cdot \boldsymbol{\eta}_l^{\mathrm{T}} \rangle = 0$	$\forall k \neq l$	errors of different measurements are uncorrelated

Furthermore, random effects may change the values of the physical parameters in the state vector. For example, a charged particle moving through the detector experiences multiple scattering and energy losses altering its track parameters. Therefore the state vector is allowed to change from one measurement to the next in a random way:

$$\mathbf{r}_k^t = \mathrm{A}_k \cdot \mathbf{r}_{k-1}^t + \boldsymbol{\nu}_k \tag{8}$$

A_k is a known linear operator represented by a matrix called *extrapolator* and describes deterministic changes between the state vectors at the $(k-1)$-th measurement $\mathbf{r}_{k-1}^t$ and at the k-th measurement $\mathbf{r}_k^t$. On the contrary, $\boldsymbol{\nu}_k$ is a random variable called *process noise* between the $(k-1)$-th and k-th measurements fulfilling the following assumptions:

$\langle \boldsymbol{\nu}_k \rangle = 0$	$\forall k$	unbiased
$\langle \boldsymbol{\nu}_k \cdot \boldsymbol{\nu}_k^{\mathrm{T}} \rangle = \mathrm{Q}_k$	$\forall k$	covariance matrix is known
$\langle \boldsymbol{\nu}_k \cdot \boldsymbol{\nu}_l^{\mathrm{T}} \rangle = 0$	$\forall k \neq l$	different process noises are uncorrelated
$\langle \boldsymbol{\nu}_k \cdot \boldsymbol{\eta}_l^{\mathrm{T}} \rangle = 0$	$\forall k, l$	process noises and measurement errors are uncorrelated

Since the state vector changes between different measurements, the goal of the fit procedure is to find the best linear unbiased estimator $\mathbf{r}_n$ of the state vector $\mathbf{r}_n^t$, which corresponds to the last measurement $\mathbf{m}_n$ [2].

The Kalman filter algorithm in its most general form consists of the following steps:

1. **Initialisation step**: In this first step, an approximate value $\mathbf{r}_0$ of the state vector is chosen and the covariance matrix and χ^2-deviation is set to

$$\begin{aligned} \mathrm{C}_0 &= \mathrm{I} \cdot \inf \\ \chi_0^2 &= 0 \end{aligned} \tag{9}$$

   where inf represents a large positive number. This choice of covariance matrix minimises the influence of the initial approximation on the final optimum estimation.

2. **Extrapolation step**: When the state vector $\mathbf{r}^t$ changes between the $(k-1)$-th and k-th measurement, the current best estimation $\mathbf{r}_{k-1}$ changes in the same manner upon transfer to the k-th measurement:

$$\begin{aligned} \tilde{\mathbf{r}}_k &= \mathrm{A}_k \cdot \mathbf{r}_{k-1} \\ \tilde{\mathrm{C}}_k &= \mathrm{A}_k \mathrm{C}_{k-1} \mathrm{A}_k^{\mathrm{T}} + \mathrm{Q}_k \end{aligned} \tag{10}$$

   $\tilde{\mathbf{r}}_k$ and $\tilde{\mathrm{C}}_k$ are the best estimator and the corresponding covariance matrix of the state vector $\mathbf{r}_k^t$ obtained in the previous step according to the first $(k-1)$ measurements and extrapolated to the k-th measurement.

3. **Filtration step**: In this final step, the estimator $\tilde{\mathbf{r}}_k$ is updated with the k-th measurement $\mathbf{m}_k$ in order to obtain the estimator $\mathbf{r}_k$ of the state vector $\mathbf{r}_k^t$ according to the first k measurements:

$$\begin{aligned}
\mathrm{S}_k &= \left(\mathrm{V}_k + \mathrm{H}_k\tilde{\mathrm{C}}_k\mathrm{H}_k^{\mathrm{T}}\right)^{-1} && \textit{weighting matrix} \\
\mathrm{K}_k &= \tilde{\mathrm{C}}_k \cdot \mathrm{H}_k^{\mathrm{T}} \cdot \mathrm{S}_k && \textit{gain matrix} \\
\boldsymbol{\zeta}_k &= \mathbf{m}_k - \mathrm{H}_k \cdot \tilde{\mathbf{r}}_k && \textit{residual} \\
\mathbf{r}_k &= \tilde{\mathbf{r}}_k + \mathrm{K}_k \cdot \boldsymbol{\zeta}_k \\
\mathrm{C}_k &= \tilde{\mathrm{C}}_k - \mathrm{K}_k\mathrm{H}_k \cdot \tilde{\mathrm{C}}_k \\
\chi_k^2 &= \chi_{k-1}^2 + \boldsymbol{\zeta}_k^{\mathrm{T}} \cdot \mathrm{S}_k \cdot \boldsymbol{\zeta}_k
\end{aligned} \tag{11}$$

Here the inverse covariance matrix of the residual S_k, also called weighting matrix, is used to calculate the gain matrix K_k. The gain matrix determines the contribution of the residual $\boldsymbol{\zeta}_k$ to the updated estimator $\mathbf{r}_k$: Measurements with larger weight, i.e. smaller covariance matrix V_k, will correct the estimation of the state vector stronger. On the contrary, the correction will be negligible when the state vector is known already with a high accuracy, i.e. small covariance matrix $\tilde{\mathrm{C}}_k$. χ_k^2 is the total χ^2-deviation of the estimator $\mathbf{r}_k$ obtained from the first k measurements following a χ^2-distribution with a specific number of degrees of freedom. It can therefore be used for the characterisation of the fit quality.

The extrapolation and filtration steps are repeated for each measurement such that after the filtration of the last measurement $\mathbf{m}_n$ the desired best estimator $\mathbf{r}_n$ (with the corresponding covariance matrix C_n) is obtained [2, 12].

In practice, the measurement model eq. (7) and the extrapolation eq. (8) are often nonlinear. However, after linearising all the equations the Kalman filter fitting algorithm can be applied unchanged. When for instance the measurement $\mathbf{m}_k$ depends non-linearly on the state vector $\mathbf{r}_k^t$, the model of measurement needs to be linearised (denoted by $\doteq$) at a certain state vector $\mathbf{r}_k^{lin}$ as *point of linearisation*:

$$\begin{aligned}
&\mathbf{m}_k\left(\mathbf{r}_k^t\right) = \mathbf{h}_k\left(\mathbf{r}_k^t\right) + \boldsymbol{\eta}_k \doteq \mathbf{h}_k\left(\mathbf{r}_k^{lin}\right) + \mathrm{H}_k \cdot \left(\mathbf{r}_k^t - \mathbf{r}_k^{lin}\right) + \boldsymbol{\eta}_{\boldsymbol{k}} \\
&\text{with the Jacobian} \qquad \left(\mathrm{H}_k\right)_{ij} = \left(\frac{\partial(\mathbf{h}_k(\mathbf{r}_k))_i}{\partial(\mathbf{r}_k)_j}\right)\Bigg|_{\mathbf{r}_k=\mathbf{r}_k^{lin}}
\end{aligned} \tag{12}$$

The same procedure can be applied to a nonlinear extrapolation equation:

$$\begin{aligned}
&\tilde{\mathbf{r}}_k^t = \mathbf{a}_k\left(\mathbf{r}_{k-1}^t\right) \doteq \mathbf{a}_k\left(\mathbf{r}_{k-1}^{lin}\right) + \mathrm{A}_k \cdot \left(\mathbf{r}_{k-1}^t - \mathbf{r}_{k-1}^{lin}\right) \\
&\text{with the Jacobian} \qquad \left(\mathrm{A}_k\right)_{ij} = \left(\frac{\partial(\mathbf{a}_k(\mathbf{r}_{k-1}))_i}{\partial(\mathbf{r}_{k-1})_j}\right)\Bigg|_{\mathbf{r}_{k-1}=\mathbf{r}_{k-1}^{lin}}
\end{aligned} \tag{13}$$

The Kalman filter with the nonlinear model of measurement is called the *extended Kalman filter*. Only the equation for the residual $\boldsymbol{\zeta}_k$ of the equations of filtration (11) then has to be modified with regards to the linear case:

$$\boldsymbol{\zeta}_k = \mathbf{m}_k - \left[\mathbf{h}_k\left(\mathbf{r}_k^{lin}\right) + \mathrm{H}_k \cdot \left(\tilde{\mathbf{r}}_k - \mathbf{r}_k^{lin}\right)\right] \tag{14}$$

The result of a fit with the extended Kalman filter depends on the choice of the point of linearisation. There are two different approaches: The point of linearisation does not explicitly appear in eq. (14)

by being set to the current track estimator $\mathbf{r}_k^{lin} = \tilde{\mathbf{r}}_k$ in the *implicit linearisation*, whereas the point of linearisation $\mathbf{r}_k^{lin}$ is explicitly set in the so-called *explicit linearisation*. The implicit linearisation can be very imprecise since the estimator depends only on $k-1$ measurements and thus can be very far from the true values. In addition to that, the linearisation cannot be improved by using better initial parameters as the initial information is already lost when processing the second measurement. Using the explicit linearisation, however, the fit can be iterated using the best estimator $\mathbf{r}_n$ from the previous iteration as point of linearisation for the next one. As a result, the fit is more accurate without requiring extra time or complexity within one iteration [2].

3.3 The KF Particle package

The *KF Particle* package is a specific software package for the complete reconstruction of short-lived particles and decay chains based on the Kalman filter mathematics. The major advantage of this package is that mother and daughter particles are described with the same state vector

$$\mathbf{r} = (x, y, z, p_x, p_y, p_z, E, s)^{\mathrm{T}}, \qquad s = \frac{L}{p} \tag{15}$$

which contains the three components of momentum (p_x, p_y, p_z) and the energy E of the respective particle parameterised at the coordinates (x, y, z). If the production vertex is known, the distance between the production and decay vertex of the particle in the laboratory coordinate system L normalised to its momentum p is added to the state vector. This parameter s is used to transport the particle between the decay and production vertices. The chosen normalisation of s is convenient since the direction of the particle motion is assigned to the momentum vector. As these parameters describe the real particles themselves, the KF Particle Package is independent from the geometry or operational conditions of the experiment. After the optimal estimator of the state vector in eq. (15) is obtained, additional physical parameters of the particle such as mass, momentum, decay length, life time and rapidity can be easily calculated with the KF Particle package [12, 2].

In order to optimally use the computing resources and achieve a high speed of calculations, the KF Particle package is implemented in single precision (float32 format) and fully SIMDized: SIMD stands for *Single Instruction, Multiple Data*, meaning that the same instruction is performed on a set of data simultaneously [12].

The KF Particle package was implemented in the following analysis for the reconstruction of short-lived particles. The information of the event characteristics, reconstructed tracks, primary vertex as well as V^0 and cascade candidates obtained from the central barrel tracking described in section 2.2 are stored in the so-called *Analysis Object Data* (AOD). The track objects were not refitted with the KF Particle package, but simply copied from the AOD file and transformed into a KF Particle object with the parametrisation of eq. (15). All the secondary vertices and the parameters of short-lived particles were then once again reconstructed with the KF Particle package (see section 3.4). The primary vertex stored in the AOD file was not refitted with the KF Particle package for this analysis. However, the KF Particle package was used once to add a charmed hadron to the primary vertex and remove the measurements of its daughter particles without repeating the entire fit procedure. For aligning a reconstructed mother particle with the primary event vertex, the default AOD PV was used.

3.4 Reconstruction of short-lived particles

Long-lived particles have a lifetime large enough to cross the tracking detector system of the experiment and to be registered directly. In contrast, *short-lived* particles decay before or short within the tracking system and can only be registered indirectly by measuring the daughter particles. Therefore, the position, momentum and energy of the mother particle at the decay vertex have to be reconstructed using the estimates of all n daughter particles obtained after the track fit. For this purpose, the mother particle is described by the state vector of the KF Particle package eq. (15) without the parameter $s = \frac{L}{p}$,

$$\mathbf{r} = (x, y, z, p_x, p_y, p_z, E)^{\mathrm{T}} = \begin{pmatrix} \mathbf{v} \\ \underline{\mathbf{p}} \end{pmatrix}, \tag{16}$$

where the variables have been summarised in the vector of the decay vertex position $\mathbf{v}$ and the 4-momentum vector of the mother particle $\underline{\mathbf{p}}$ [2, 12].

The parameters of the k-th daughter particle given at a certain parametrisation point $\mathbf{v}_k^{\mathrm{d}}$ are denoted by:

$$\mathbf{r}_k^{\mathrm{d}} = \begin{pmatrix} \mathbf{v}_k^{\mathrm{d}} \\ \underline{\mathbf{p}}_k^{\mathrm{d}} \end{pmatrix} \tag{17}$$

All daughter particles are then transported to the decay vertex position in order to be used as measurements $\mathbf{m}_k$ by the Kalman filter algorithm:

$$\mathbf{m}_k = \mathbf{r}_k^{\mathrm{d}} + \begin{pmatrix} \mathbf{p}_k^{\mathrm{d}} \\ \mathbf{p}_k^{\mathrm{d}} \times B \cdot q_k \\ 0 \end{pmatrix} \cdot s_k^{\mathrm{d}} + \mathcal{O}\left((s_k^{\mathrm{d}})^2\right) \tag{18}$$

Here $s_k^{\mathrm{d}} = \frac{l_k^{\mathrm{d}}}{p_k^{\mathrm{d}}}$ is the unknown length from the parametrisation point $\mathbf{v}_k^{\mathrm{d}}$ of the daughter particle to the decay vertex $\mathbf{v}$, B the magnetic field value at $\mathbf{v}_k^{\mathrm{d}}$ and q_k the charge of the daughter particle. $\mathcal{O}\left((s_k^{\mathrm{d}})^2\right)$ describes higher order deviations of the daughter particle trajectory from a straight line in a magnetic field.
Linearising at $s_k^{\mathrm{d}} = 0$, the measurement $\mathbf{m}_k$ and the corresponding covariance matrix V_k of the daughter particle parameters at the decay vertex are given by:

$$\begin{aligned} \mathbf{m}_k &= \mathbf{r}_k^{\mathrm{d}} \\ \mathrm{V}_k &= \begin{pmatrix} \mathrm{V}_k^{\mathrm{v}} & \left(\mathrm{V}_k^{\mathrm{vp}}\right)^{\mathrm{T}} \\ \mathrm{V}_k^{\mathrm{vp}} & \mathrm{V}_k^{\mathrm{p}} \end{pmatrix} = \mathrm{C}_k^{\mathrm{d}} + \begin{pmatrix} \mathbf{p}_k^{\mathrm{d}} \\ \mathbf{p}_k^{\mathrm{d}} \times B \cdot q_k \\ 0 \end{pmatrix} \cdot \begin{pmatrix} \mathbf{p}_k^{\mathrm{d}} \\ \mathbf{p}_k^{\mathrm{d}} \times B \cdot q_k \\ 0 \end{pmatrix}^{\mathrm{T}} \cdot \sigma_s^2 \end{aligned} \tag{19}$$

It is sufficient to take 10-times the distance between the parametrisation point $\mathbf{v}_k^{\mathrm{d}}$ and an initially assumed decay vertex position $\mathbf{v}^0$ divided by the daughter particle momentum p_k^{d} as σ_s [2].
Moreover, daughter particles can be selected by calculating the χ^2 probability that the k-th particle $\mathbf{r}_k^{\mathrm{d}}$ originated from the initially assumed decay vertex $\mathbf{v}^0$ and thus is likely to be a daughter particle:

$$\chi_{\mathrm{d}}^2 = \left(\mathbf{v}_k^{\mathrm{d}} - \mathbf{v}^0\right)^{\mathrm{T}} \cdot \left(\mathrm{C}^{\mathbf{v}^0} + \mathrm{V}_k^{\mathrm{v}}\right)^{-1} \cdot \left(\mathbf{v}_k^{\mathrm{d}} - \mathbf{v}^0\right) \tag{20}$$

Here, $\mathrm{C}^{\mathbf{v}^0}$ is the corresponding covariance matrix of the initial vertex guess $\mathbf{v}^0$. Then, only particles passing the χ^2 cut are added to the mother particle [2].

Since the measurement of the k-th daughter particle and the state vector of the mother particle contain the coordinates of the decay vertex, their true values are related via the following measurement equation:

$$(\mathrm{I}, \mathrm{O}) \cdot \mathbf{m}_k^t = (\mathrm{I}, \mathrm{O}) \cdot \mathbf{r}_{k-1}^t \tag{21}$$

Thus, the estimator of the state vector from the first k particles $\mathbf{r}_{k-1}$ is filtered by the measurement $\mathbf{m}_k$ according to the filtration eq. (11) with

$$\begin{aligned}
\tilde{\mathbf{r}}_k &\equiv \mathbf{r}_{k-1} \\
\tilde{\mathrm{C}}_k &\equiv \mathrm{C}_{k-1} \\
\mathbf{m}_k &\equiv (\mathrm{I}, \mathrm{O}) \cdot \mathbf{r}_k^{\mathrm{d}} = \mathbf{v}_k^{\mathrm{d}} \\
\mathrm{V}_k &\equiv (\mathrm{I}, \mathrm{O}) \cdot \mathrm{V}_k \cdot (\mathrm{I}, \mathrm{O})^{\mathrm{T}} = \mathrm{V}_k^{\mathrm{v}}
\end{aligned} \tag{22}$$

After this filtration step, the 4-momentum of the daughter particle is added to the 4-momentum of the mother particle (see [2] for details). This process is repeated for all daughter particles. For the first daughter particle, the measurement $\mathbf{m}_1$ is simply copied into the state vector $\mathbf{r}_1$ since the parameters of the mother particle have not yet been determined [2].

After the mother particle is reconstructed at the decay vertex, the parameter

$$s = \frac{L}{p} \tag{23}$$

is added to the the state vector when the production vertex of the mother particle is known. L is the length of the particle trajectory in the laboratory system between the decay vertex and a given production vertex: This can either be the primary event vertex or a secondary vertex of a prior decay. In the latter case, the secondary vertex is fitted first using the mother particle and then the mother particle is fitted to the reconstructed vertex. Then all parameters of the mother particle are transported from the decay to the production vertex where it is filtered using the production vertex as a measurement [2].

3.5 Mass and topological constraint

The precision of a particle's parameters and its decay vertex resolution can be improved by taking assumptions, expressed in terms of constraints applied on the state vector, into account. Two constraints are implemented in the KF Particle package: The *topological constraint*, aligning a mother particle with the already known primary (or more general parent) vertex, and the *mass constraint*, setting the mass of the mother particle to a specific value when a combination of particles originating from the secondary vertex are known to originate from a narrow width mass state [2].

Constraints are in general applied after the filtration of the state vector by the measurements. Typically, every constraint is treated as a one-dimensional measurement with the value zero and null error:

$$0 = \mathrm{H}_c \cdot \mathbf{r}_c + 0 \tag{24}$$

This measurement is then filtered in an additional filtration step of the Kalman filter algorithm according to eq. (11) with a corresponding measurement model H_c. In the case of nonlinear constraints, the penalty, eq. (24), is linearised as any other model of measurement and the filtering equations are applied. When a mother particle decays close to its parent vertex for example, the curvature of the trajectory in the magnetic field of the detector can be neglected and the topological constraint then connects the mother particle with the parent vertex by a straight line [2].

The mass constraint in case of the state vector of the KF Particle Package eq. (15) in particular is a nonlinear problem:

$$f(\mathbf{r}) = E^2 - \left(p_x^2 + p_y^2 + p_z^2\right) - M^2 = 0 \tag{25}$$

Here M^2 is the invariant mass to be set. By linearising the condition in eq. (25), the distribution of the mass of reconstructed mother particles will follow a broadened distribution centred at M^2

with tails around the peak. Therefore a nonlinear mass constraint based on the *Lagrange method* has been implemented in the KF Particle package guaranteeing the exact constraint on the particle mass. The mass constraint can also be written as

$$f(\mathbf{r}) = \left(\mathbf{x}^{\mathrm{T}}, \mathbf{p}^{\mathrm{T}}, E\right) \cdot \begin{pmatrix} \mathrm{O} & \mathrm{O} & 0 \\ \mathrm{O} & -\mathrm{I} & 0 \\ 0 & 0 & 1 \end{pmatrix} \cdot \begin{pmatrix} \mathbf{x} \\ \mathbf{p} \\ E \end{pmatrix} - m_0^2 = \mathbf{r}^{\mathrm{T}} \cdot \mathrm{M} \cdot \mathbf{r} - m_0^2 = 0 \tag{26}$$

with $\mathbf{x} = (x, y, z)^{\mathrm{T}}$ and $\mathbf{p} = (p_x, p_y, p_z)^{\mathrm{T}}$. The Lagrangian for the mass constraint can then be defined as

$$L = (\mathbf{r}_c - \mathbf{r})^{\mathrm{T}}(\mathbf{r}_c - \mathbf{r}) + \lambda \cdot f(\mathbf{r}_c) \tag{27}$$

where $\mathbf{r}$ is an initial state vector and $\mathbf{r}_c$ is the final state vector with a mass constraint set on. By minimising the Lagrangian with regards to $\mathbf{r}_c$, one obtains an expression for the updated state vector $\mathbf{r}_c$:

$$\frac{\partial L}{\partial \mathbf{r}_c} \stackrel{!}{=} 0 \quad \Rightarrow \quad \mathbf{r}_c = (\mathrm{I} + \lambda \mathrm{M})^{-1} \cdot \mathbf{r} \tag{28}$$

Inserting this expression for $\mathbf{r}_c$ into eq. (26) results in the following equation for the Lagrange multiplier λ with $p^2 = p_x^2 + p_y^2 + p_z^2$:

$$f(\lambda) = -M^2 \cdot \lambda^4 + (E^2 - p^2 + 2M^2) \cdot \lambda^2 - 2(E^2 + p^2) \cdot \lambda + (E^2 - p^2 - M^2) = 0 \tag{29}$$

This equation cannot be solved analytically in general, but numerically with Newton's method: The solution is found iteratively according to

$$\lambda_n = \lambda_{n-1} - \frac{f(\lambda_{n-1})}{f'(\lambda_{n-1})} \tag{30}$$

starting with the solution of the quadratic equation without the λ^4-term in eq. (29) as initial value λ_0 since the mass correction is assumed to be small [12].

In order to fully appreciate the effect of applying a mass constraint in the reconstruction of a decay chain, consider the case where a daughter particle B of a mother particle A decays itself into multiple daughter particles. The B-candidate has itself a broadened mass distribution with Gaussian contributions due to the measurement uncertainties of its daughter particles. This introduces an additional uncertainty to the mass of the reconstructed A-candidate. However, the mass resolution of the A-candidate can be significantly improved by setting a mass constraint on particle B. Moreover, the more reliably the mass of candidate B is exactly set to its true value, the better is the mass resolution of particle A [12].

4 Methodology for the analysis

4.1 Residuals and pulls

The quality check of a track or vertex fit is performed on simulated events by comparing the fitted parameters to their corresponding simulated values. For each parameter two histograms for the so-called *residuals* and *pulls* are produced: The residual is the difference between the fitted value p and simulated value p^t of the parameter under consideration, the pull is the residual normalised to the expected uncertainty σ_p obtained from the covariance matrix of the fit:

$$\begin{aligned} \text{residual} &= p - p^t \\ \text{pull} &= \frac{p - p^t}{\sigma_p} \end{aligned} \tag{31}$$

The residual has the dimension of the parameter under consideration whereas the pull is dimensionless. If the residual and pull distribution of a parameter are centred at zero, the parameter has been reconstructed without a bias. Moreover, if the pull distribution follows approximately a Gaussian distribution with standard deviation $\sigma = 1$ (and $\mu = 0$), also called *standard normal distribution*, the uncertainties of the fitted parameters have been estimated correctly. The dispersion of the residual is called *resolution*. It characterises rather the detector than the precision of the fit algorithm since the effects of approximations and linearsations of the measurement and extrapolation equations in the Kalman filter become negligible after several iterations of the fit [2, 4].

In order to estimate the resolution of the reconstructed primary event vertex as well as the decay vertex and parameters of a short-lived charmed hadron reconstructed with the KF Particle package, the residual and pull distribution of the PV, SV and transverse momentum of the heavy-flavour hadron are analysed. For this, multi-Gaussian fit functions are examined in section 4.3. Different fit functions for the parameter estimation of the mass distribution of the charmed hadron are discussed in section 4.4.

4.2 Least squares method for binned histograms

The most frequently adopted method to estimate parameters of a distribution according to a set of measurements is the so-called *maximum likelihood method*: Given a sample $(x_1, ..., x_n)$ of n random variables whose probability density function (PDF) has a known form depending on m parameters $\boldsymbol{\theta} = (\theta_1, ..., \theta_m)$, the *likelihood function* $L(x_1, ..., x_n|\boldsymbol{\theta})$ is defined as the probability density at the point $(x_1, ...x_n)$ for certain values of the parameters $\boldsymbol{\theta}$. The maximum likelihood estimator returns the values $\hat{\boldsymbol{\theta}} = (\hat{\theta}_1, ..., \hat{\theta}_m)$ for which the likelihood function evaluated at the measured sample $(x_1, ..., x_n)$ is maximum [4].

Consider a set of n measurements $(y_1 \pm \sigma_1, ..., y_n \pm \sigma_n)$ where each measurement corresponds to a value x_i of a variable x. It is assumed that the model for the dependence of y on the variable x is given by a function $f(x, \boldsymbol{\theta})$. If the measurements y_i are distributed around the value $f(x_i, \boldsymbol{\theta})$ according to a Gaussian distribution with standard deviation equal to the measurement error, maximising the Likelihood $L\,(y_1, ..y_n|\boldsymbol{\theta})$ is equivalent to minimising

$$\chi^2(\boldsymbol{\theta}) = \sum_{i=1}^{n} \frac{(y_i - f(x_i, \boldsymbol{\theta}))^2}{\sigma_i^2}. \tag{32}$$

The method of minimising the χ^2 variable in eq. (32) in order to obtain an estimate of the parameters $\boldsymbol{\theta}$ is referred to as *least squares method*. The minimum χ^2 value obtained in a fit of the data sample,

$\hat{\chi}^2$, is expected to follow a χ^2 distribution with a number of degrees of freedom k equal to the number of measurements n minus the number of fit parameters m, $k = n - m$:

$$\begin{aligned} f_{\chi^2}(x;k) &= \frac{x^{\frac{k}{2}-1} \cdot e^{-\frac{x}{2}}}{2^{\frac{k}{2}} \cdot \Gamma\left(\frac{k}{2}\right)} \\ \mathrm{E}(x) &= \langle x \rangle = k \\ \mathrm{Var}(x) &= \langle x^2 \rangle - \langle x \rangle^2 = 2k \end{aligned} \tag{33}$$

One advantage of the least squares method is that the minimum χ^2 value can be used as measurement of the goodness of fit, for instance by calculating the *reduced* χ^2 *value*:

$$\hat{\chi}^2_{\text{red}} = \frac{\hat{\chi}^2}{k} \tag{34}$$

Since $\hat{\chi}^2$ is known to follow a χ^2 distribution with k degrees of freedom, the expectation value and variance of the reduced χ^2-value are given by:

$$E\left(\hat{\chi}^2_{\text{red}}\right) = \frac{E(\hat{\chi}^2)}{k} = \frac{k}{k} = 1 \tag{35}$$

$$\mathrm{Var}(\hat{\chi}^2_{\text{red}}) = \frac{\mathrm{Var}(\hat{\chi}^2)}{k^2} = \frac{2k}{k^2} = \frac{2}{k} \tag{36}$$

For a large number of of degrees of freedom k due to a large number of measurements n a, the χ^2-distribution becomes approximately Gaussian. Taking the square root of the variance of the reduced χ^2 value as standard deviation of this approximately Gaussian peak, $\sigma = \sqrt{2/k}$, it can be tested whether the deviation of the χ^2_{red} value from 1 is statistically significant [4].

The maximum likelihood method uses the complete set of information given by the entire measurement sample. This may cause problems with regards to the necessary computing power and machine precision or it is simply not preferable to use the entire sample. Thus, the sample's information is frequently summarised by binning the distribution of the random variable and using the number of entries in each single bin as information $(n_i, ..., n_N)$, where the number of intervals N is typically significantly smaller than the number of measurements n. If the measurement sample is composed of independent extractions from a given random distribution, the number of entries in each interval follows a *Poisson distribution*:

$$\begin{aligned} f_{\mathrm{P}}(n;\nu) &= e^{-\nu} \cdot \frac{\nu^n}{n!} \\ \mathrm{E}(n) &= \langle n \rangle = \nu \\ \mathrm{Var}(n) &= \langle n^2 \rangle - \langle n \rangle^2 = \nu \end{aligned} \tag{37}$$

The corresponding mean ν is given by the expected number of entries in that bin:

$$\mu_i(\boldsymbol{\theta}) = \int_{x_i^{\text{low}}}^{x_i^{\text{up}}} f(x;\boldsymbol{\theta})\,dx \approx f(\bar{x}_i;\boldsymbol{\theta}) \cdot \Delta x_i \tag{38}$$

Here $\left[x_i^{\text{low}}, x_i^{\text{up}}\right]$ is the interval corresponding to the i^{th} bin. For sufficiently fine binning, the expected number of entries can be approximated by multiplying the value of the PDF at the centre of the bin $\bar{x}_i = (x_i^{\text{up}} + x_i^{\text{low}})/2$ with width Δx_i. Furthermore, the Poisson distributions can be approximated by Gaussian distributions for sufficiently large number of entries in each bin: Using the *expected* number of entries $\mu_i(\boldsymbol{\theta})$ or the *observed* number of entries n_i respectively as variances, the following χ^2 variables can be defined:

$$\chi^2_{\mathrm{P}} = \sum_{i=1}^{N} \frac{(n_i - \mu_i(\boldsymbol{\theta}))^2}{\mu_i(\boldsymbol{\theta})} \qquad \textit{Pearson's } \chi^2 \tag{39}$$

$$\chi^2_{\mathrm{N}} = \sum_{i=1}^{N} \frac{(n_i - \mu_i(\boldsymbol{\theta}))^2}{n_i} \qquad \textit{Neyman's } \chi^2 \tag{40}$$

The minimum (Pearson's or Neyman's) χ^2 values obtained in a least squares fit of the histogram follow a χ^2 distribution with the number of degrees of freedom k equal to the number of bins N minus the number of fit parameters m. Therefore, they can be used for parameter estimation and determination of the goodness of fit as described above. In the following analysis, the optimal set of parameters and the corresponding covariance matrix are estimated with a nonlinear least squares fit using the *scipy.optimize.curve_fit* function. Since *scipy.optimize.curve_fit* uses the observed numbers of entries n_i as variances, only Neyman's χ^2 values will be calculated for the estimation of the goodness of fit [4].

The Gaussian approximation does not hold for small number of entries and a Poissonian model should be applied in this case: If the number of measurements is sufficiently large and the assumed model correct,

$$\chi^2_{\lambda} = -2 \ln \left(\prod_{i=1}^{N} \frac{f_{\mathrm{P}}\left(n_i | \mu_i(\boldsymbol{\theta})\right)}{f_{\mathrm{P}}(n_i | n_i)} \right) \tag{41}$$

follows a χ^2-distribution the number of degrees of freedom k equal to the number of bins N minus the number of fit parameters m. However, the Gaussian approximation is assumed to be sufficient since the number of entries is sufficiently large in the peak region of the distributions under consideration in this analysis. Moreover, only bins with 5 or more entries will be used for fitting in order to avoid problems with the Gaussian approximation in bins with few entries. The bins with small number of entries lie only in the tails of the distributions under consideration and thus, only statistical outliers will be omitted from the fit. Furthermore, the ratio of the number of entries in each bin n_i to the expected values $\mu_i(\boldsymbol{\theta})$ will be checked in order to determine in which part of the distribution possible deviations arise: The ratios should be consistent with one within their uncertainties in the peak region, but small deviations in the tail where the statistical fluctuations are high are not significant [4].

4.3 Multi-Gaussian fits

In order to detect a possible dependency from the resolution of one parameter on another one, the analysis of the pull and residual distributions has been performed in different intervals of this parameter. For instance, the primary vertex resolution is determined as a function of the number of tracks contributing to the vertex fit, the so-called *number of contributors.* For events with short-lived particles on the other hand, the secondary vertex resolution and parameters of the mother particle are analysed as a function of the transverse momentum p_{T} of the mother particle. One might expect that the residual and pull distributions of a parameter for a single interval are distributed according to a Gaussian function. However, a single Gaussian function is not sufficient to properly describe the underlying distribution, as its tails in particular are underestimated. Therefore a sum of multiple Gaussians is fitted to the corresponding distributions. Since the resolution of a vertex or physical parameter of a decayed particle depends on the uncertainty of the individual tracks used for their reconstruction, the resolution of the parameter under consideration might differ significantly even for the exact same interval of number of contributors or transverse momentum:

- Short-lived particles decaying before or shortly within the tracking system have to be reconstructed from their daughter particles. Having none or only few direct measurements, the uncertainties of the track parameters of the mother particle are comparably large.

- Since multiple scattering is a random process, one or more track used for reconstruction of a vertex or short-lived particle might be extraordinarily affected and its uncertainty increased. This might especially be the case when events with similar number of contributors are selected, but the number of low-momentum particles, which are affected more by multiple scattering, varies.

- Particles passing through dead areas or outside the acceptance of a sub-detector have a reduced number of measurements and possibly a shorter length of measured track, increasing the uncertainties of the corresponding track parameters. For a small number of tracks used for reconstruction of a vertex or decayed particle, the resolution of the fitted parameters may be decisively determined by the number of tracks reconstructed from very few measurements.

As a result, events from the exact same interval of number of contributors or transverse momentum can be divided into different classes characterised by e.g. the number of short-lived particles or tracks with very poor resolution. However, not for every possible combination of the effects described above an additional Gaussian distribution is fitted as many of these classes have a similar resolution or the statistics are insufficient such that only outliers in the tails of the distribution might be noticeable. With regards to computing effort and in order to avoid overfitting (especially of statistical fluctuations in the tails of the residual and pull distributions), an additional Gaussian is added to the fit function until it properly describes the data.

Let n be the number of individual Gaussian distributions, then the overall fit function is given by

$$f_n\left(x; A_1, ..., A_n, \mu_1, ..., \mu_n, \sigma_1, ..., \sigma_n\right) = \sum_{i=1}^{n} \frac{A_i}{\sqrt{2\pi} \cdot \sigma_i} \cdot \exp\left(-\frac{(x-\mu_i)^2}{2\sigma_i^2}\right) \tag{42}$$

The A_i are normalisation factors with the dimension of *number of events* $N_i \times$ *binwidth* b, μ_i the mean values and σ_i the standard deviations of the individual Gaussians.

The mean values μ_i and standard deviations σ_i of the individual Gaussians are weighted with the normalisation constants A_i in order to estimate the position and width of the peak of the underlying distribution:

$$\begin{aligned} \mu_w &= \frac{\sum_{i=1}^{n} A_i \cdot \mu_i}{\sum_{i=1}^{n} A_i} \\ \sigma_w &= \frac{\sum_{i=1}^{n} A_i \cdot \sigma_i}{\sum_{i=1}^{n} A_i} \end{aligned} \tag{43}$$

This is equivalent to using the number of events associated to each Gaussian

$$N_i = \frac{A_i}{b} \tag{44}$$

as weights since the factor $1/b$ cancels from eq. (43). The uncertainties of the weighted parameters are calculated with Gaussian error propagation taking all the correlations of the various variables

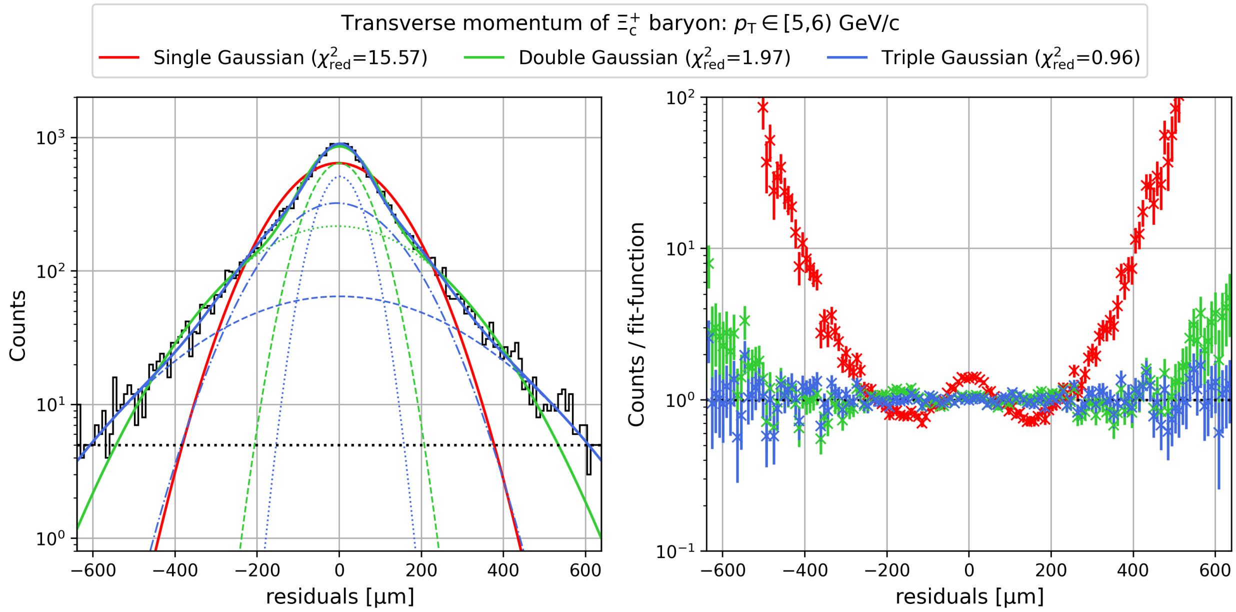

Figure 4: Fit of a single-Gaussian, double-Gaussian and triple-Gaussian to the SV residual distribution for Ξ_c^+ candidates (corresponding to case 5 in table 3) with transverse momentum $5 \leq p_T < 6\,\mathrm{GeV}/c$ (left). The ratio of the histogram with respect to the value of the corresponding fit function is plotted on the right.

into account. By writing

$$\mathbf{x} = (A_1, ..., A_n, \sigma_1, ..., \sigma_n)$$

$$V = \left(\begin{array}{ccc|ccc} (\Delta A_1)^2 & \mathrm{cov}(A_1,A_2) & \mathrm{cov}(A_1,A_3) & \mathrm{cov}(A_1,\sigma_1) & \mathrm{cov}(A_1,\sigma_2) & \mathrm{cov}(A_1,\sigma_3) \\ \mathrm{cov}(A_1,A_2) & (\Delta A_2)^2 & \mathrm{cov}(A_2,A_3) & \mathrm{cov}(A_2,\sigma_1) & \mathrm{cov}(A_2,\sigma_2) & \mathrm{cov}(A_2,\sigma_3) \\ \mathrm{cov}(A_1,A_3) & \mathrm{cov}(A_2,A_3) & (\Delta A_3)^2 & \mathrm{cov}(A_3,\sigma_1) & \mathrm{cov}(A_3,\sigma_2) & \mathrm{cov}(A_3,\sigma_3) \\ \hline \mathrm{cov}(A_1,\sigma_1) & \mathrm{cov}(A_2,\sigma_1) & \mathrm{cov}(A_3,\sigma_1) & (\Delta\sigma_1)^2 & \mathrm{cov}(\sigma_1,\sigma_2) & \mathrm{cov}(\sigma_1,\sigma_3) \\ \mathrm{cov}(A_1,\sigma_2) & \mathrm{cov}(A_2,\sigma_2) & \mathrm{cov}(A_3,\sigma_2) & \mathrm{cov}(\sigma_1,\sigma_2) & (\Delta\sigma_2)^2 & \mathrm{cov}(\sigma_2,\sigma_3) \\ \mathrm{cov}(A_1,\sigma_3) & \mathrm{cov}(A_2,\sigma_3) & \mathrm{cov}(A_3,\sigma_3) & \mathrm{cov}(\sigma_1,\sigma_3) & \mathrm{cov}(\sigma_2,\sigma_3) & (\Delta\sigma_3)^2 \end{array}\right) \tag{45}$$

the uncertainty can be calculated in the following way:

$$(\Delta\sigma_w)^2 = \sum_{i,j=1}^{n} \frac{\partial\sigma_w}{\partial\mathbf{x}_i} \cdot \frac{\partial\sigma_w}{\partial\mathbf{x}_j} \cdot \mathrm{V}_{ij} \tag{46}$$

The additional terms in the 6×6 dimensional covariance matrix for a triple-Gaussian in eq. (45) with respect to the 4×4 dimensional covariance matrix for a double-Gaussian are marked in red. As a result, the uncertainty of the weighted standard deviation for the double-Gaussian distribution

σ_w^{DG} is given by:

$$\begin{aligned}
s_2 &= A_1 + A_2 \\
w_2 &= A_1\sigma_1 + A_2\sigma_2 \\
s_2^4 \cdot \left(\Delta\sigma_w^{\mathrm{DG}}\right)^2 &= (\sigma_1 - \sigma_2)^2 \left[(A_1\Delta A_2)^2 + (A_2\Delta A_1)^2\right] \\
&\quad + 2\,\mathrm{cov}(A_1, A_2) \cdot (w_2 - s_2 \cdot \sigma_1) \cdot (w_2 - s_2 \cdot \sigma_2) \\
&\quad + s_2^2 \cdot \left[(A_1\Delta\sigma_1)^2 + (A_2\Delta\sigma_2)^2 + 2A_1A_2 \cdot \mathrm{cov}(\sigma_1, \sigma_2)\right] \\
&\quad - 2\,s_2 \cdot \big\{A_1 \cdot [\mathrm{cov}(A_1, \sigma_1) \cdot (w_2 - s_2 \cdot \sigma_1) + \mathrm{cov}(A_2, \sigma_1) \cdot (w_2 - s_2 \cdot \sigma_2)] \\
&\qquad\quad + A_2 \cdot [\mathrm{cov}(A_1, \sigma_2) \cdot (w_2 - s_2 \cdot \sigma_1) + \mathrm{cov}(A_2, \sigma_2) \cdot (w_2 - s_2 \cdot \sigma_2)]\,\big\}
\end{aligned} \tag{47}$$

The formula of the uncertainty of the weighted standard deviation of a triple-Gaussian distribution is given in the appendix, eq. (59), and the corresponding formulas for the weighted mean are easily obtained by replacing $\sigma_i \longleftrightarrow \mu_i$.

4.4 Fit functions for the mass distribution

The mass of the reconstructed Ξ_c^+ baryon is analysed in different transverse momentum intervals of the Ξ_c^+ baryon. If the detector resolution is much smaller than the particles decay width, the mass distribution of a decayed particle follows a so-called *Breit-Wigner distribution*: It arises from the square of the propagator of the virtual particle which mediates the decay. However, if the decay width of the particle cannot be resolved by the detector, its mass distribution follows a *Gaussian distribution* which width is determined by the detector resolution. The convolution of the Breit-Wigner and Gaussian distribution, the *Voigt profile*, takes both of these effects into account when the particle's decay width and the detector resolution are similar in magnitude. In order to obtain a suitable description of the underlying mass distribution, all of these three fit functions were examined [4].

Firstly, the Gaussian distribution (**G**) is defined by

$$f_{\mathrm{G}}(x; N_{\mathrm{G}}, \mu_{\mathrm{G}}, \sigma) = \frac{N_{\mathrm{G}}}{\sqrt{2\pi} \cdot \sigma} \cdot \exp\left(-\frac{(x - \mu_{\mathrm{G}})^2}{2\sigma^2}\right) \tag{48}$$

with the parameters μ_{G} and σ being the mean and standard deviation respectively. It is normalised to unity for $N_{\mathrm{G}} = 1$ and its full width at half maximum (FWHM) is given by

$$\mathrm{FWHM}_{\mathrm{G}} = 2\sqrt{2\ln(2)} \cdot \sigma \tag{49}$$

Secondly, the *Breit-Wigner* distribution (**BW**) is given by

$$f_{\mathrm{BW}}(x; N_{\mathrm{BW}}, x_0, \gamma) = \frac{N_{\mathrm{BW}}}{\pi} \frac{\gamma}{(x - x_0)^2 + \gamma^2} \tag{50}$$

and normalised to unity for $N_{\mathrm{BW}} = 1$. The parameter x_0 determines the position of the maximum of the distribution and the parameter γ determines the half width at half maximum (HWHM) such that

$$\mathrm{FWHM}_{\mathrm{BW}} = 2\gamma \tag{51}$$

The mean and variance of a Breit-Wigner distribution are undefined since the integrals of $x \cdot f_{\mathrm{BW}}(x)$ and $x^2 \cdot f_{\mathrm{BW}}(x)$ themselves are undefined [4].

Finally, the *Voigt profile* (**V**) is a convolution of a Gaussian and a Breit-Wigner distribution:

$$
\begin{aligned}
f_{\mathrm{V}}(x;\mu_{\mathrm{G}},\sigma,x_0,\gamma) &= \int_{-\infty}^{+\infty} d\tilde{\nu}\;\; f_{\mathrm{G}}(\tilde{\nu})\cdot f_{\mathrm{BW}}(x-\tilde{\nu})\,d\tilde{\nu} \\
&= \int_{-\infty}^{+\infty} d\tilde{\nu}\;\; \frac{1}{\sqrt{2\pi}\sigma}\exp\left(-\frac{(\tilde{\nu}-\mu_G)^2}{2\sigma^2}\right)\cdot\frac{1}{\pi}\frac{\gamma}{(x-\tilde{\nu}-x_0)^2+\gamma^2}
\end{aligned}
\tag{52}
$$

The convolution integral defining the Voigt profile in eq. (52) cannot be evaluated analytically. Therefore eq. (52) has to be rewritten: Starting with the variable transformation $\tilde{\nu}=\nu+\mu_{\mathrm{G}}$ with $d\tilde{\nu}=d\nu$ and defining $\mu_{\mathrm{V}}:=\mu_{\mathrm{G}}+x_0$ as the centre of the Voigt profile results in:

$$
\begin{aligned}
f_{\mathrm{V}}(x;\mu_{\mathrm{V}},\sigma,\gamma) &= \frac{\gamma}{\pi^{3/2}}\int_{-\infty}^{+\infty} d\nu\;\; \frac{1}{\sqrt{2}\sigma}\exp\left(-\frac{\nu^2}{2\sigma^2}\right)\cdot\frac{1}{(x-\nu-\mu_{\mathrm{V}})^2+\gamma^2} \\
&= \frac{\gamma}{\pi^{3/2}}\int_{-\infty}^{+\infty} d\nu\;\; \frac{1}{\sqrt{2}\sigma}\exp\left(-\frac{\nu^2}{2\sigma^2}\right)\cdot\frac{1}{2\sigma^2\cdot\left[\left(\frac{x-\mu_{\mathrm{V}}}{\sqrt{2}\sigma}-\frac{\nu}{\sqrt{2}\sigma}\right)^2+\frac{\gamma^2}{2\sigma^2}\right]}
\end{aligned}
$$

Performing the additional variable transformation $t:=\frac{\nu}{\sqrt{2}\sigma}$ with $dt=\frac{d\nu}{\sqrt{2}\sigma}$ and introducing the dimensionless variables

$$
\begin{aligned}
a &= \frac{x-\mu_{\mathrm{V}}}{\sqrt{2}\sigma} \\
b &= \frac{\gamma}{\sqrt{2}\sigma}
\end{aligned}
\tag{53}
$$

leads to

$$
f_{\mathrm{V}}(a,b) = \frac{1}{\sqrt{2\pi}\sigma}\cdot\frac{b}{\pi}\int_{-\infty}^{+\infty} dt\;\; \frac{e^{-t^2}}{(a-t)^2+b^2} = \frac{1}{\sqrt{2\pi}\sigma}\cdot K(a,b) \tag{54}
$$

By defining the complex number $z:=a+ib$ the function $K(a,b)$ can be identified as the real part of the complex function

$$
\begin{aligned}
W(z) &= \frac{i}{\pi}\int_{-\infty}^{+\infty} dt\;\; \frac{e^{-t^2}}{z-t} \\
&= \frac{i}{\pi}\int_{-\infty}^{+\infty} dt\;\; \frac{e^{-t^2}}{a+ib-t} \\
&= \frac{i}{\pi}\int_{-\infty}^{+\infty} dt\;\; \frac{e^{-t^2}\cdot[(a-t)-ib]}{[(a-t)+ib]\,[(a-t)-ib]} \\
&= \underbrace{\frac{b}{\pi}\int_{-\infty}^{+\infty} dt\;\; \frac{e^{-t^2}}{(a-t)^2+b^2}}_{=\mathrm{Re(W(z))}} + i\cdot\underbrace{\frac{1}{\pi}\int_{-\infty}^{+\infty} dt\;\; \frac{e^{-t^2}\cdot(a-t)}{(a-t)^2+b^2}}_{=\mathrm{Im(W(z))}}
\end{aligned}
$$

which is related to the *complex error function* $\mathrm{erf}(z)$ via

$$
\begin{aligned}
w(z) &= e^{-z^2}\cdot[1-\mathrm{erf}(-iz)] \\
w(z) &= \begin{cases} W(z) & y>0 \\ W(z)+2e^{-z^2} & y<0 \end{cases}
\end{aligned}
$$

All in all, the convolution integral defining the Voigt profile in eq. (52) can be related to the complex error function. Although it cannot be evaluated analytically as well, robust numerical algorithms for the complex error function can be used to evaluate the Voigt profile enabling a fit of the Voigt function to data in the following way:

$$f_{\mathrm{V}}(x; N_{\mathrm{V}}, \mu_{\mathrm{V}}, \sigma, \gamma) = \frac{N_{\mathrm{V}}}{\sqrt{2\pi} \cdot \sigma} \cdot \mathrm{Re}\left[\mathrm{w}\left(\frac{\mathrm{x} - \mu_{\mathrm{V}} + \mathrm{i}\gamma}{\sqrt{2} \cdot \sigma}\right)\right] \tag{55}$$

Again, eq. (55) is normalised to unity for $N_{\mathrm{V}} = 1$ [9].

The Gaussian and Breit-Wigner distributions (eq. (48) and eq. (50), respectively) as well as the Voigt profile eq. (55) were fitted to the mass distribution of the reconstructed Ξ_{c}^{+} baryon for each p_{T} interval (see as an example fig. 5). On the left panel of fig. 5 the histogram of the mass and the corresponding fit functions are plotted, whereas on the right panel of fig. 5 the ratio of the histogram and the fit function is shown. In addition, the corresponding reduced χ^2_{red} values are reported in the legend as an overall measure of the fit quality. The fitted Breit-Wigner distribution is too narrow and too high in the peak region and overestimates the tails. In contrast, the Gaussian distribution describes the peak very well, but largely underestimates the tails of the mass distribution. This is also reflected by the large deviations of $\chi^2_{\mathrm{red,BW}} = 33.12$ and $\chi^2_{\mathrm{red,G}} = 6.56$ from 1. The Voigt profile however describes the underlying distribution over the entire range of the mass distribution with a χ^2_{red} value of 1.46. Taking $\sigma = \sqrt{2/100} \approx 0.14$ as standard deviation of the χ^2_{red} value, its deviation from 1 corresponds to 3.25σ. One could argue that this is statistically significant, but the deviations mainly arise from the tail of the mass distribution with low statistics. Moreover, the ratio of the histogram to the fit function almost always overlap with one within their uncertainties and therefore does not deviate more than 3σ from one. fig. 5 shows one of the cases with a higher χ^2_{red} value, in fact almost all other χ^2_{red} values are smaller. The fitted Voigt profiles provide the best description of the mass distributions and are therefore used for the following analysis.

The position of the centre of the Voigt profile μ_{V} is directly obtained from the fit and the corresponding error from the estimated covariance matrix of the fit parameters. The FWHM of the Voigt profile can be estimated from the fit parameters for σ and γ according to the so-called *Kielkopf approximation*

$$\begin{aligned} \mathrm{FWHM}_{\mathrm{V}} &= 0.5343 \cdot \mathrm{FWHM}_{\mathrm{BW}} + \sqrt{0.2169 \cdot \mathrm{FWHM}_{\mathrm{BW}}{}^2 + \mathrm{FWHM}_{\mathrm{G}}{}^2} \\ &= 1.0686\gamma + 2\sqrt{0.2169\gamma^2 + 2\ln(2) \cdot \sigma^2} \end{aligned} \tag{56}$$

which is accurate up to 0.023% [5].

In order to obtain an estimate for the maximum total uncertainty of the FWHM of the Voigt profile, the error for the FWHM of the Voigt profile due to the (co-) variances of the parameters of the fit function calculated analogue to eq. (46) is added in quadrature to the maximum uncertainty of the approximation formula marked in red:

$$\begin{aligned} (\Delta \mathrm{FWHM}_{\mathrm{V}})^2 = &\frac{(4\ln(2)\sigma)^2 \cdot (\Delta\sigma)^2}{0.2169\gamma^2 + 2\ln(2) \cdot \sigma^2} + \frac{(1.0686 + 2 \cdot 0.2169\gamma)^2 \cdot (\Delta\gamma)^2}{0.2169\gamma^2 + 2\ln(2) \cdot \sigma^2} \\ &+ \frac{2\,(1.0686 + 2 \cdot 0.2169\gamma) \cdot (4\ln(2)\sigma) \cdot \mathrm{cov}(\sigma, \gamma)}{0.2169\gamma^2 + 2\ln(2) \cdot \sigma^2} + 0.0023^2 \end{aligned} \tag{57}$$

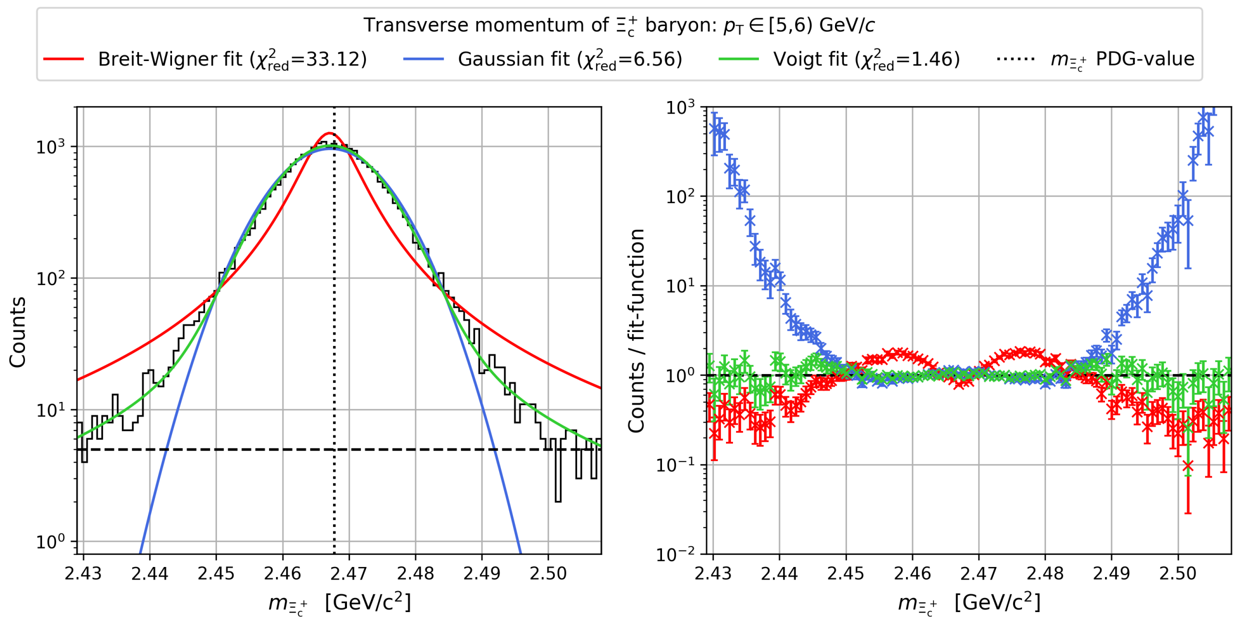

Figure 5: Fits of a Gaussian function, Breit-Wigner distribution and Voigt profile to the mass distribution of Ξ_c^+ candidates (corresponding to case 5 in table 3) with reconstructed transverse momentum of $5 \leq p_T < 6\,\mathrm{GeV}/c$ (left). The ratio of the histogram with respect to the values of the corresponding fit function are plotted on the right.

5 Minimum-bias Monte Carlo data

5.1 Minimum-bias triggered Monte Carlo data

In order to test the reconstruction of the AOD PV by comparing the reconstructed vertex coordinates with their corresponding true values, data generated in *Monte Carlo* (MC) simulations is used. MC simulations are used in particle physics to simulate particle collisions and are based on a great number of random experiments. Using the event generator *PYTHIA8* with the input of branching ratios of particle decays amongst others, primary collisions are simulated including the information of all emerging particles. The interaction with the detector material and the corresponding detector responses of the final state particles were simulated with the detector response simulation code *GEANT3*. Afterwards the simulated clusters created by the simulated particles in the detector are digitised such that the final data sample closely resembles the real recorded data and that it can be reconstructed and analysed in the exact same way [8, 7].

For the first part of the analysis, MC data for minimum-bias triggered pp-collisions at a centre-of-mass energy of $\sqrt{s} = 13\,\mathrm{TeV}$ is used. The simulated data with approximately 54.6 million candidates was modelled using the Run 2 ALICE setup. Since the abundance of heavy-flavour quarks in minimum-bias data is low, it can be used to investigate whether certain systematic effects of the AOD PV resolution in charm-enriched MC data are caused by the presence of the heavy-flavour hadron or whether it is rather an artefact of the vertex reconstruction in general.

5.2 AOD primary vertex resolution

The resolution of the AOD PV is studied in intervals of the number of contributors N_{Cont} given by the variable *PV_NContributors* (see fig. 6). The mean value of the number of contributors for minimum-bias triggered MC data is 14.2, whereas the *median*, defined as the point $\bar{x}$ where $P(x < \bar{x}) = P(x > \bar{x})$ for a given probability distribution [4], is 10.0.

In order to estimate the parameters of the PV residual distribution along the x- and y-axis, a double-Gaussian fit function is used for the six lowest and three highest N_{Cont}-intervals as the contribution of the tails is sufficiently described by one additional Gaussian distribution for small N_{Cont} or the statistics are limited for high N_{Cont}-intervals. For the remaining intervals, a triple-Gaussian fit function is used. For the PV residual distribution along the z-axis, a triple-Gaussian fit function is used for the lower half, whereas a double-Gaussian fit function suffices for the upper half of the N_{Cont}-intervals.

The mean value of the AOD PV residual distribution is depicted in fig. 7: After an increase of the mean residuals along the x- and y-axis, the mean residuals reach their approximately constant value of $3.0\,\mu$m for the x-axis, $0.8\,\mu$m for the y-axis and $-4.4\,\mu$m for the z-axis. Thus, the reconstructed AOD PV coordinates are, on average, slightly overestimated for the x- and y- axis and underestimated for the z-axis. fig. 8 shows that the resolution of the PV along the z-axis is significantly worse than for the x- and y-axis, especially for low number of contributors. In addition to that, the resolution in the transversal plane is asymmetric since the standard deviation for the x-axis is significantly larger than for the y-axis for all N_{Cont} intervals.

The pull distribution does not exactly correspond to a standard normal distribution: The absolute values of the mean pulls increase systematically with increasing N_{Cont} (see fig. 16). Moreover, the weighted standard deviation of the pull distributions along the different coordinate axes in fig. 17 are significantly smaller than 1 and slightly decrease with increasing number of contributors. They range approximately from 0.9 to 0.86 for the x- and y-axis and from 0.96 to 0.92 for the z-axis. Thus, the uncertainties of the AOD PV variables are on average slightly overestimated.

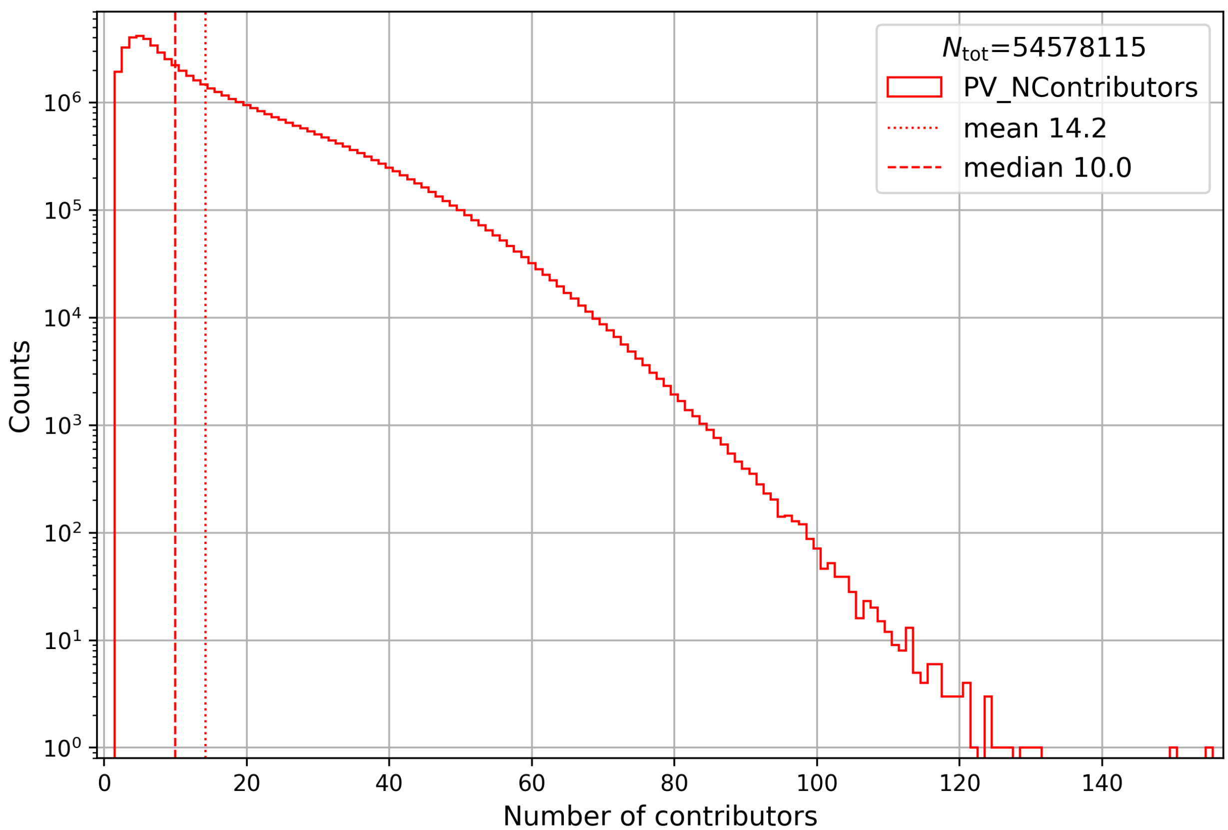

Figure 6: Number of contributors in minimum-bias triggered MC data.

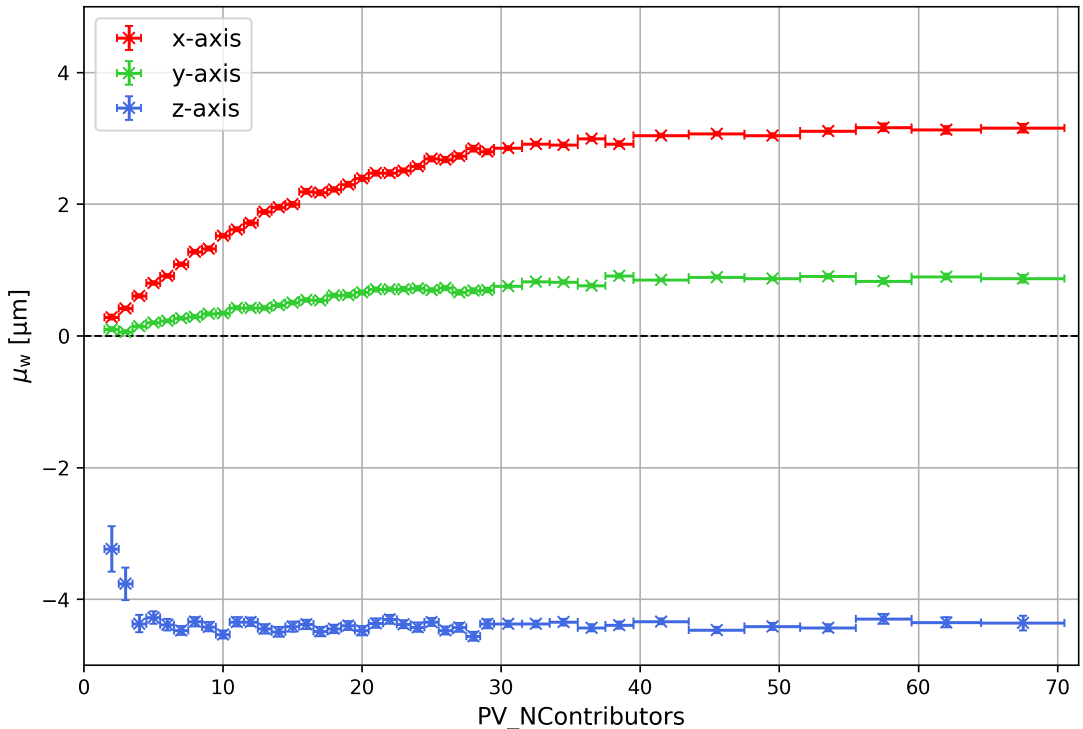

Figure 7: Weighted mean of the PV residual distribution as a function of the number of contributors.

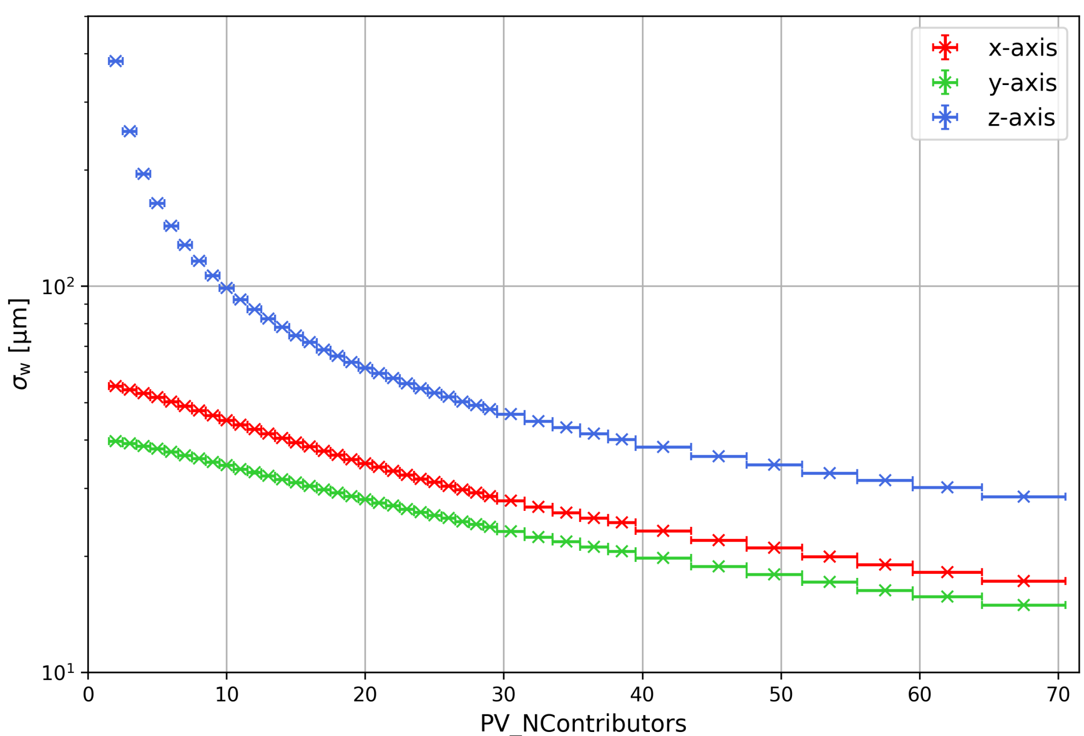

Figure 8: Weighted standard deviation of the PV residual distribution as a function of the number of contributors.

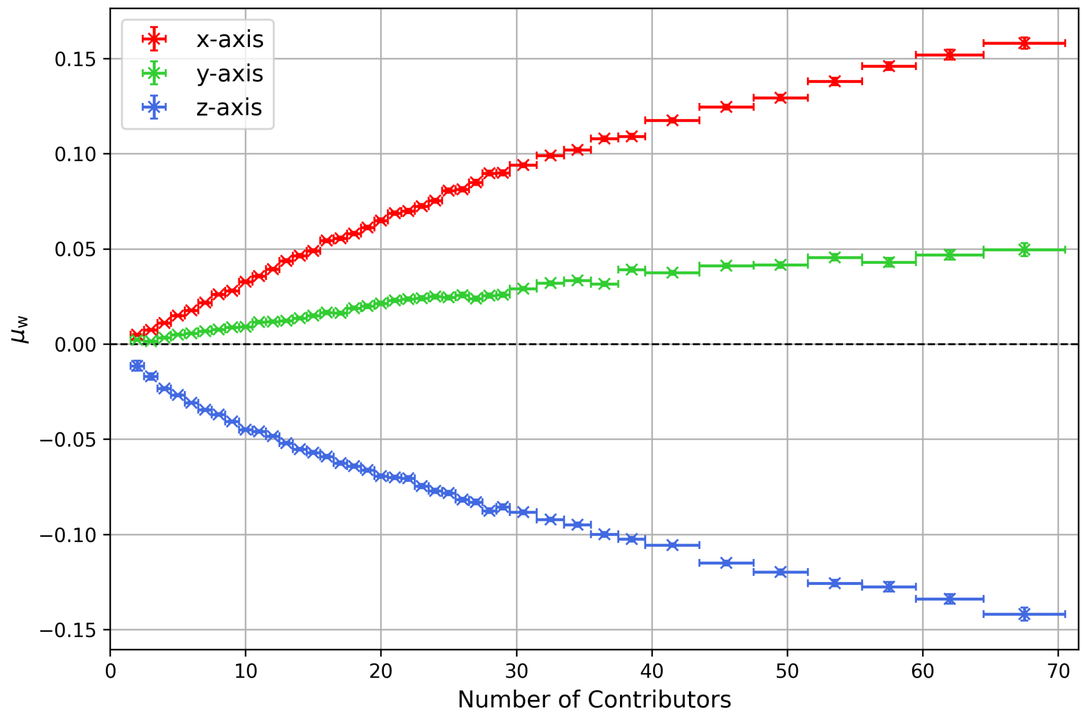

Figure 9: Weighted mean of the PV pull distribution obtained from double-Gaussian fits as a function of the number of contributors.

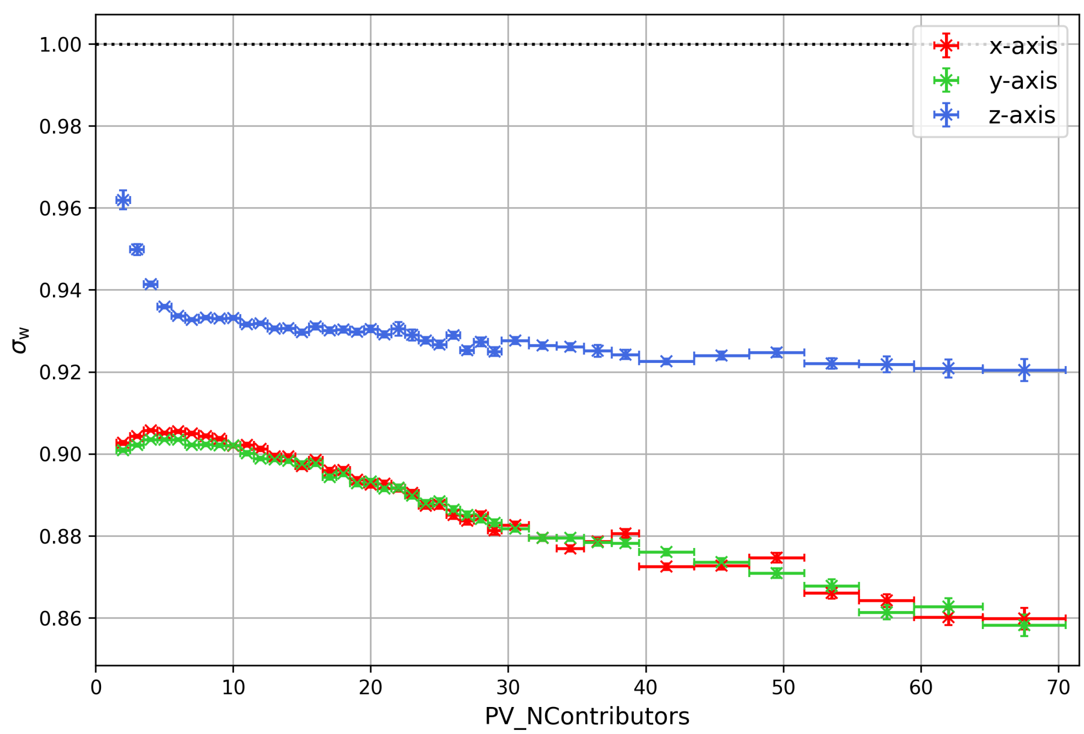

Figure 10: Weighted standard deviation of the PV pull distribution in minimum-bias MC data obtained from double-Gaussian fits as a function of the number of contributors.

6 Charm-enriched Monte Carlo data

6.1 Monte Carlo data for the analysis of $\Xi_c^+ \to \Xi^-\pi^+\pi^+$

In order to test the mass and topological constraints implemented in the KF Particle package, MC data for the decay $\Xi_c^+ \to \Xi^-\pi^+\pi^+$ is used. The analysis is restricted to the case where the Ξ^- decays into a π^- and a Λ^0 baryon, which in turn decays into a proton and a π^- (see fig. 11).

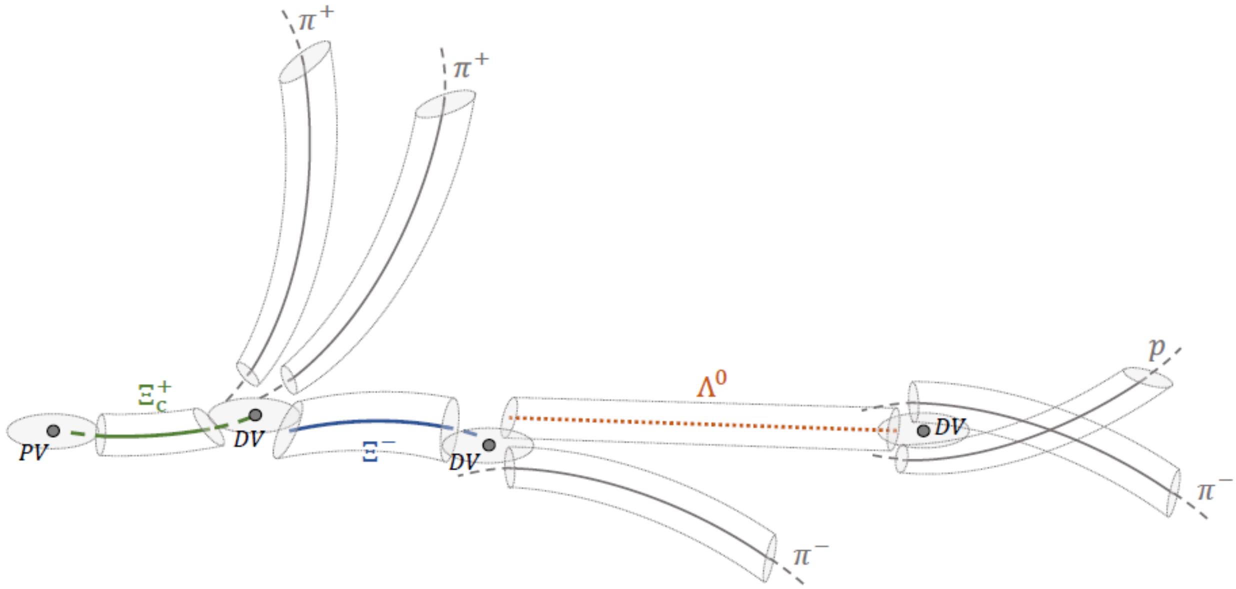

Figure 11: Non-resonant decay chain of a prompt Ξ_c^+ baryon [7].

Due to its very short decay length of 136 μm [11], the Ξ_c^+ baryon will practically never be directly detected by the ITS. In contrast, a significant fraction of the Ξ^- baryon will decay within the ITS and therefore produce hits in (multiple) ITS layers. As the Λ^0 is neutral, it will not generate any signals in the ITS itself, but its charged decay daughters might produce hits in the outer layers of the ITS (compare table 1 with table 2).

The MC data was again generated with the event generator *PYTHIA8* and detector response simulator *GEANT3*. The data was modelled for pp-collisions at $\sqrt{s} = 13\,\text{TeV}$ using the ALICE setup specifically for every year of Run 2. Thus, effects from the accumulated radiation damage for instance are taken into account in order to resemble the real data taken in that period as closely as possible. A $c\bar{c}$-pair was injected in two thirds of the events and a $b\bar{b}$-pair in the remaining events. However, only simulated events containing the decay channel $\Xi_c^+ \to \Xi^-\pi^+\pi^+$ were selected. The Ξ_c^+ baryons originating from the decay of a beauty hadron are called *feed-down* Ξ_c^+, whereas the ones produced directly in the primary collision and therefore originating from the primary vertex are called *prompt* particles. In addition to that, a small fraction of prompt and feed-down candidates were simulated to decay via the resonance $\Xi_c^+ \to \Xi(1530)^0\pi^+ \to \Xi^-\pi^+\pi^+$. Nevertheless, only prompt non-resonant Ξ_c^+ baryons are taken into account in the following analysis.

An overview of the mass and topological constraints is given in table 3. Since the goal of the analysis is to reconstruct the Ξ_c^+ baryon, the mass constraints are only applied on the daughter particles Ξ^- and Λ^0 using the corresponding masses from the *Particle Data Group* (PDG) listed in table 2. The Λ^0 is constrained to its parent vertex, the decay vertex (DV) of the Ξ^-, whereas the Ξ^- is constrained to the PV. This is justified by the fact that the Ξ_c^+ has a very short decay

particle (quark content)	mass $\left[\mathrm{GeV/c^2}\right]$	lifetime [s]	decay length $c\tau$ [cm]
Ξ_c^+ (usc)	2.46771 ± 0.00023	$(453 \pm 5) \cdot 10^{-15}$	0.0136
Ξ^- (dss)	1.32171 ± 0.00007	$(1.639 \pm 0.015) \cdot 10^{-10}$	4.9136
Λ^0 (uds)	1.115683 ± 0.000006	$(2.632 \pm 0.020) \cdot 10^{-10}$	7.8905

Table 2: Properties of the short-lived baryons in the non-resonant Ξ_c^+ decay chain [11].

length of $c\tau = 136\,\mu$m which is comparable to the spatial resolution of ALICE in Run 2 (compare with the PV resolution in fig. 15 for instance) and much smaller than the decay length of the Ξ^- baryon of $c\tau \approx 4.9\,$cm. In addition to that, the PV is known very precisely compared to the SV (see fig. 22), i.e. the DV of the Ξ_c^+, and it is preferable to use the best possible vertex for the topological constraint. Starting from the instance of the Ξ_c^+ reconstructed without any additional physical constraints, the application of the individual constraints follows a bottom-up scheme in order to obtain different instances of the reconstructed Ξ_c^+: The mass constraints are applied first and only then the topological constraints are added. This sequence of constraints in table 3 is natural since the optimal daughter candidate should be used to reconstruct the associated mother particle. The different instances of the reconstructed Ξ_c^+ are then stored in separate data sets such that the resolution of the vertices and physical parameters can be compared afterwards. Overall approximately 170.000 prompt non-resonant Ξ_c^+ candidates are analysed for every data set.

#	mass constraint on Λ^0	mass constraint on Ξ^-	topological constraint of Λ^0 to Ξ^- DV	topological constraint of Ξ^- to PV	topological constraint of Ξ_c^+ to PV
0	-	-	-	-	-
1	x	-	-	-	-
2	x	x	-	-	-
3	x	x	-	-	x
4	x	x	x	-	-
5	x	x	x	x	-
6	x	x	x	x	x

Table 3: Applied constraints in each data set used for the analysis.

The analysis is always performed in intervals of the reconstructed transverse momentum of the Ξ_c^+ with the exception of the analysis of the p_T-residuals since the true MC value of the transverse momentum of the Ξ_c^+ baryon is not stored for case 3 in table 3. In addition to that, the p_T distribution does not change significantly for the different instances of the reconstructed Ξ_c^+ from table 3 (see fig. 12) and the resolution of the reconstructed transverse momentum of the order of $10\,\mathrm{MeV}/c$ is sufficient (see section 6.6). Therefore, $p_\mathrm{T,rec}$ is denoted as p_T in the following. The number of candidates associated to each p_T interval are given in table 4: The number of candidates is maximal for medium transverse momenta and decreases for low and high transverse momenta respectively.

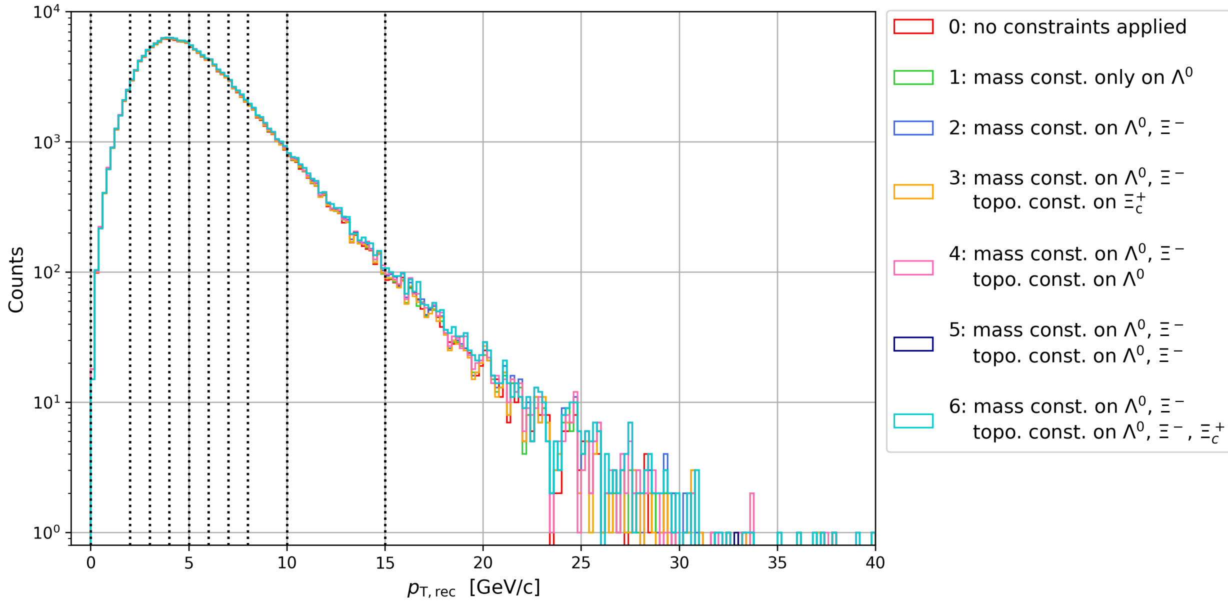

Figure 12: Distribution of the reconstructed transverse momentum of the different instances of the prompt non-resonant Ξ_c^+ baryons. The black, dotted lines indicate the p_T intervals used in the analysis.

$p_{\mathrm{T,rec}}$ [GeV/c]	0-2	2-3	3-4	4-5	5-6	6-7	7-8	8-10	10-15
$\langle N_{\mathrm{Cand}} \rangle$	9712	20357	29529	30177	24456	18251	12380	13504	9011

Table 4: Average number of candidates $\langle N_{\mathrm{Cand}} \rangle$ for every p_T-bin for the different analysis cases given in table 3.

6.2 AOD primary vertex resolution

The following analysis of the AOD PV resolution has been performed for Ξ_c^+ candidates reconstructed with both mass constraints on Λ^0 and Ξ^- and the topological constraint on the Ξ_c^+ to the PV (case 3 in table 3).

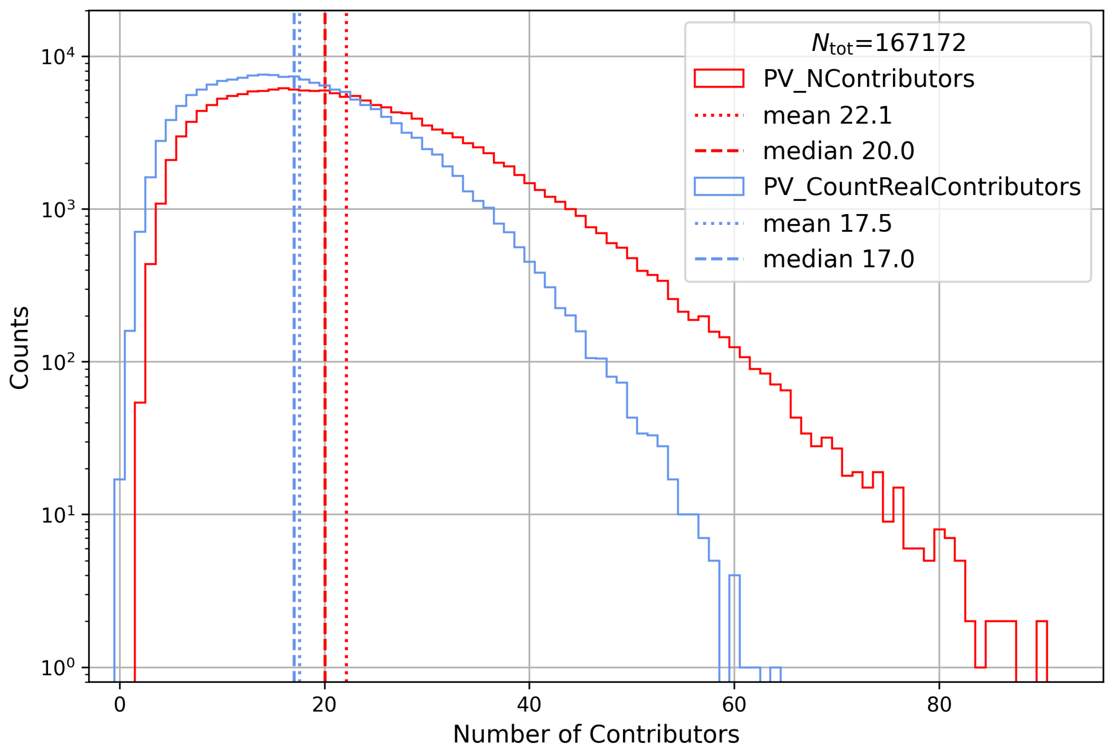

Figure 13: Distribution of the number of contributors as a function of the variables PV_NContributors and PV_CountRealContributors.

The distribution of the number of contributors is shown in fig. 13 as a function of two different variables: In contrast to *PV_CountRealContributors*, PV_NContributors includes some tracks which are not added as direct daughters in the vertex fit, but belong in fact to daughter particles originating from a secondary vertex. Thus, the minimum value of PV_NContributors is 2 as two tracks are needed to fit a vertex. On the contrary, the minimum value of PV_CountRealContributors can be 0 when a mother particle originating from the PV has a very short decay length (as it is the case for the Ξ_c^+) and the PV has therefore been in fact reconstructed using only daughter particles of short-lived particles. Since every candidate in the charm-enriched MC sample contains the decay of $\Xi_c^+ \to \Xi^- \pi^+ \pi^+$ and the charged pions for instance might be used for fitting the PV even though they do not increment the counter of PV_CountRealContributors, the value of PV_CountRealContributors is always smaller than or equal to the value of PV_NContributors. All in all, the number of contributors is increased in comparison to the minimum-bias MC data (compare with fig. 6): The values for mean and median of PV_NContributors increase from 14.2 and 10.0 to 22.1 and 20.0 respectively, but also the values of the mean value of 17.5 and median of 17.0 of PV_CountRealContributors are larger. Since PV_CountRealContributors does not take daughter particles into account, it provides a more robust estimate of the number of contributors and is therefore used for the analysis of the PV resolution.

The mean values of the AOD PV residual distribution are constant over the entire range of the number of contributors and for all three coordinate axes. The mean values of the PV residuals averaged over all N_{cont} intervals are approximately $+2.2\,\mu$m along the x-axis, $+0.8\,\mu$m along the y-axis and $-4.1\,\mu$m in z-direction (see fig. 14). Thus, the mean values of the AOD PV residuals are almost identical for minimum-bias and charm-enriched MC data. However, an increase of the mean PV residuals is not detectable for the x- and y- axis as in the minimum-bias MC data. This is due to the fact that the statistics for the charm-enriched MC data are significantly lower, especially in the first N_{cont}, and the PV_CountRealContributors intervals, including also candidates which would be assigned to higher PV_NContributors intervals, are therefore chosen much larger. The low N_{Cont} increase is therefore mitigated or statistically insignificant.

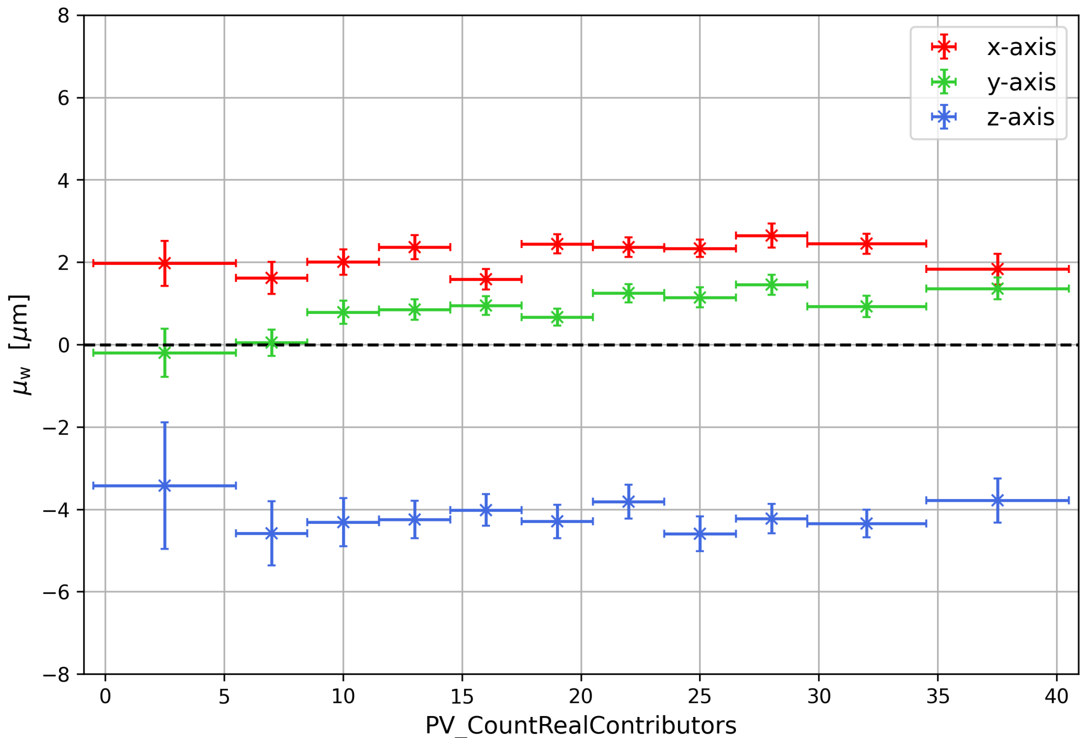

Figure 14: Weighted mean of the PV residual distribution obtained from double-Gaussian fits as a function of the real number of contributors.

For all three coordinate axes, the standard deviation of the PV residuals decreases with increasing number of contributors (see fig. 15) as expected. The AOD PV resolution along the x- and y-axis ranging from approximately $50\,\mu$m or $40\,\mu$m respectively to $20\,\mu$m is almost identical to the obtained AOD PV resolution in minimum-bias MC data. The AOD PV resolution along the beamline (z-axis) ranging from $120\,\mu$m to approximately $30\,\mu$m is again worse than in the transversal xy-plane. In contrast to the first N_{Cont} intervals in minimum-bias MC data, the width of the PV residuals along the z-axis does not increase above $120\,\mu$m since the number of candidates containing only very few primary tracks (PV_CountRealContributors≤ 2) in the first N_{Cont} interval for charm-enriched MC data is small compared to the candidates with $3 \leq \text{PV}_{\text{C}}\text{ountRealContributors} \leq 5$ and a much better vertex resolution. As a result, their impact on the weighted parameters obtained from the double-Gaussian fit is rather small if they are not omitted as statistical outliers from the fit in the first place. Moreover, the xy-asymmetry of the AOD PV resolution is confirmed also for the charm-enriched MC data.

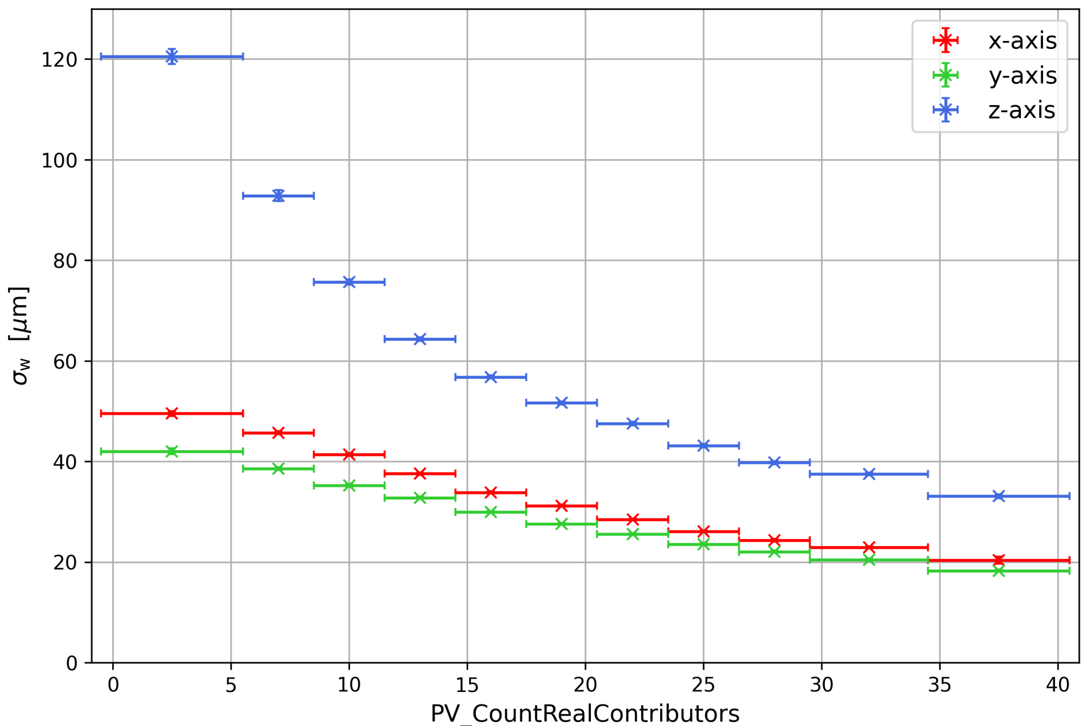

Figure 15: Weighted standard deviation of the PV residual distribution obtained from double-Gaussian fits as a function of the real number of contributors.

Figure 16 shows the mean value of the AOD PV pull distribution. As for minimum-bias MC data, the mean values are close to zero for small N_{Cont} and deviate with the same magnitude (maximum ± 0.1) from zero for large number of contributors. Although the deviations are significant especially for large N_{Cont}, they are comparably small with respect to the width of the pull distribution and can therefore be roughly approximated with zero. The weighted standard deviations of the pull distribution along all three coordinate axes depicted in fig. 17 are consistent with 1 within their uncertainties for small numbers of contributors and decrease significantly up to approximately 0.9 for large number of contributors. Thus, for increasing number of contributors the uncertainties of the reconstructed AOD PV are again slightly overestimated.

To sum up, the resolution of the AOD primary vertex is mainly unaffected by the presence of charmed baryons. The small biases of the respective vertex coordinates are probably rather an intrinsic bias of the reconstruction algorithm than an effect of the Ξ_c^+ decay. The uncertainties of each vertex coordinate appears to be slightly overestimated.

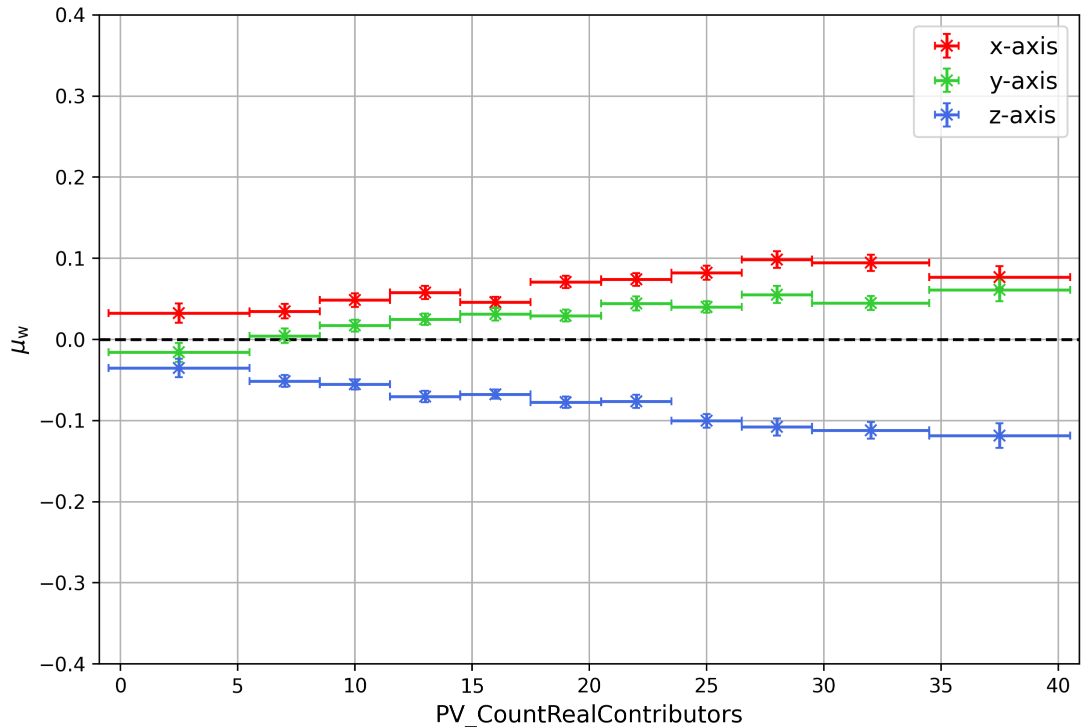

Figure 16: Weighted mean of the PV pull distribution obtained from single-Gaussian fits as a function of the real number of contributors.

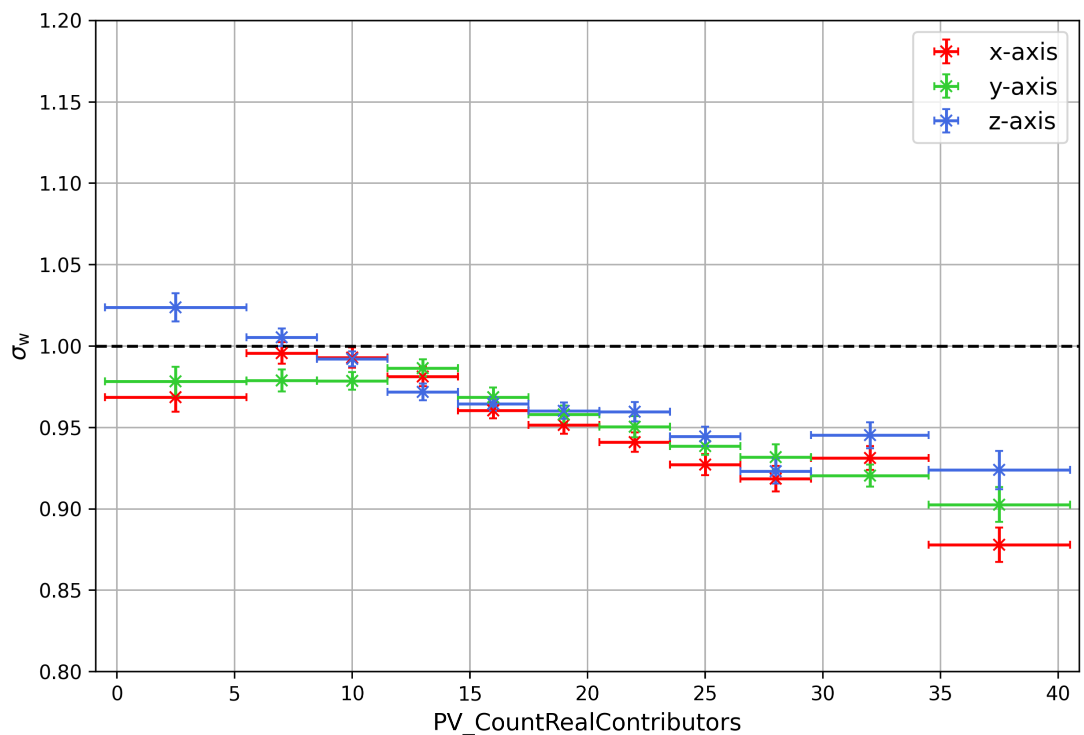

Figure 17: Weighted standard deviation of the PV pull distribution obtained from single-Gaussian fits as a function of the real number of contributors.

6.3 Primary vertex shifts

In order to test whether the primary vertex is systematically biased in the direction of the decay vertex of the Ξ_c^+ baryon due to including its daughter tracks in the PV fit, the PV shift s is calculated: The vector connecting the reconstructed PV with the true MC PV, $\vec{t} - \vec{r}$, is projected on the vector connecting the true MC SV with the true MC PV, $\vec{t}$ (see fig. 18):

$$s = \frac{(\vec{t} - \vec{r}) \cdot \vec{t}}{|\vec{t}|} = (\vec{t} - \vec{r}) \cdot \vec{e}_t \tag{58}$$

Here, $\vec{e}_t$ denotes the normalised vector in direction of $\vec{t}$. Thus, the value of the PV shift is negative when the PV has been reconstructed behind the MC PV looking from the MC SV, and positive when the reconstructed PV is in front of the MC PV. The width of the PV shift distribution can be interpreted as a measure of how far the reconstructed PV spreads around the MC PV and therefore as a measure of the PV resolution.

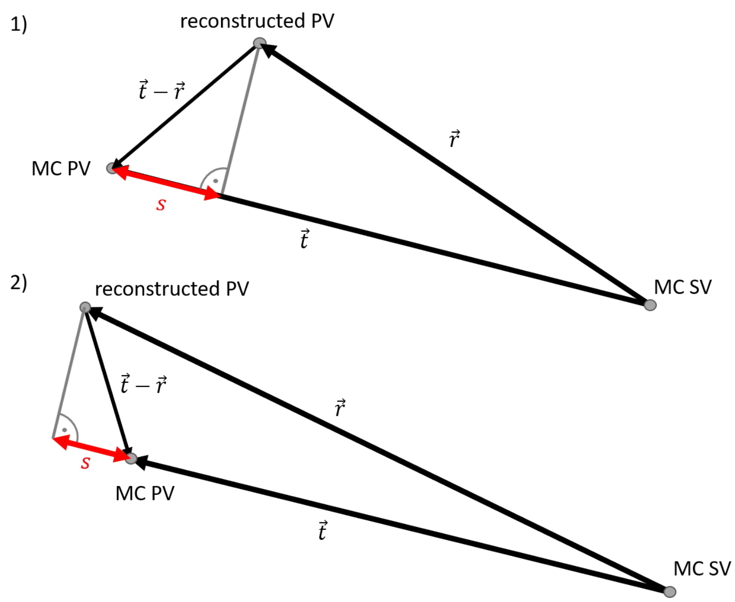

Figure 18: Sketch of the calculation of the primary vertex shifts s. Looking from the MC SV position, the PV has been reconstructed in front of the MC PV in case 1), whereas the PV has been reconstructed behind the MC PV in case 2).

The parameters of the shift distribution have been analysed for different intervals of the transverse momentum of the Ξ_c^+ for two different instances of the reconstructed primary event vertex: The default and a recalculated version of the AOD PV, where the Ξ_c^+ is added and the measurements of its daughter particles are removed from the PV fit. For this, the instance of the Ξ_c^+ reconstructed with mass constraints on both daughter particles, Λ^0 and Ξ^-, and topological constraint of the Ξ_c^+ to the AOD PV (case 3 in table 3) is used. A double-Gaussian distribution has been fitted to the PV shift distributions for both instances of the reconstructed PV and every single p_T interval.

The mean values of the PV shift distributions deviate significantly from zero for every p_T interval. By adding the reconstructed Ξ_c^+ baryon and removing its daughter particles, the mean shifts change from approximately $+4\,\mu$m to approximately $-2.7\,\mu$m (see fig. 19). This might suggest that the PV is on average slightly shifted to the SV before recalculating the AOD PV and a little bit less shifted away from the SV afterwards. However, since the mean value of the AOD PV shift with respect to the SV has the same magnitude as the intrinsic AOD PV shift, i.e. the mean values of the AOD PV residual distribution, it can not be unequivocally attributed to the decay of the Ξ_c^+. The inversion of the mean shifts after recalculating the AOD PV could be caused by daughter particles from the decay of the other heavy-flavour hadron which contains the $\bar{c}$ anti-quark and has not been taken into account in the recalculation of the PV. For the majority of the simulated collisions, it is emitted back-to-back in the centre-of-mass frame and therefore the other charmed hadron and its daughters tend to be on the opposite side of the Ξ_c^+ in the laboratory frame.

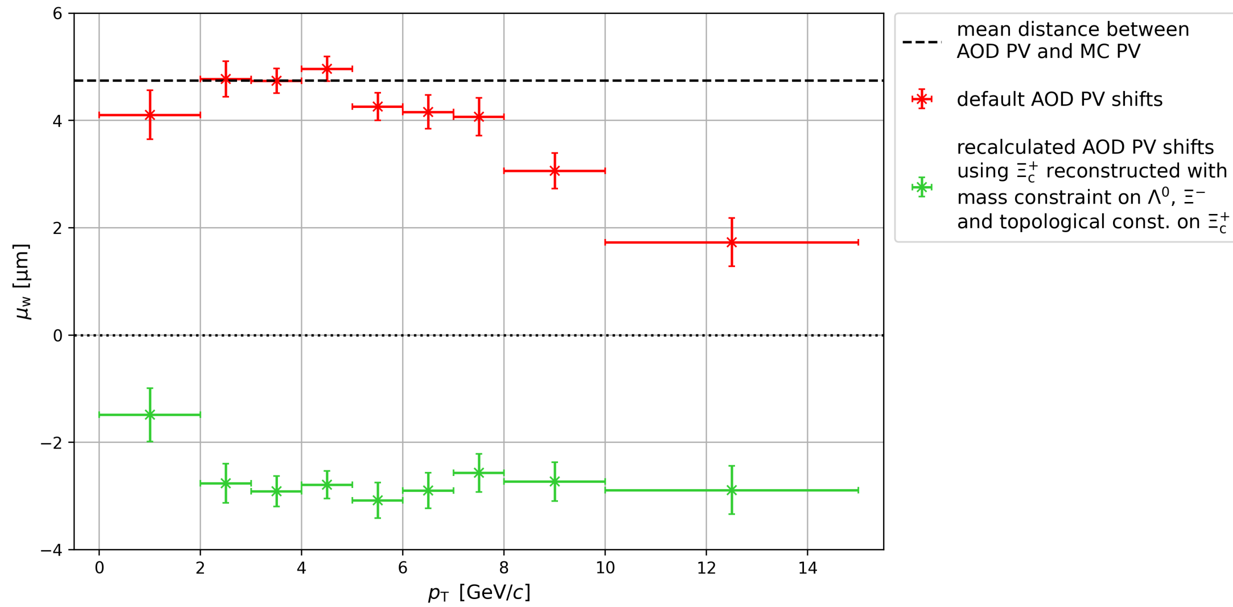

Figure 19: Mean values of the PV shifts obtained from double-Gaussian fits as a function of the transverse momentum of the Ξ_c^+ baryon. The mean distance between the default AOD PV and MC PV, which is calculated by adding the mean AOD PV residual for each coordinate from fig. 14 averaged over all p_T intervals in quadrature, is shown as reference.

The weighted standard deviation σ_w of the PV shift distribution is shown in fig. 20 and is on average 40 μm, which is comparable to the AOD PV resolution. Since σ_w is minimal for the default AOD PV for every p_T interval, the PV resolution appears to be better for the default AOD PV. This could be the case as probably precise measurements of both π^+ originating from the decay of the Ξ_c^+ and possibly a measured Ξ^- are replaced by a poorly reconstructed Ξ_c^+ (see fig. 22 below), therefore increasing the uncertainty of the recalculated PV. However, other versions of the AOD PV recalculated with better reconstructed instances of the Ξ_c^+ were not available in the course of this thesis.

To conclude, it is clear from fig. 19 and fig. 20 that there is no PV shift in direction of the SV in the order of $\mathcal{O}(10\,\mu\text{m})$ which is comparable or larger than the PV (shift) resolution. Further tests, e.g. the number of removed daughter particles, are needed in order to characterise the observed mean shifts as a result of the Ξ_c^+ baryon or intrinsic biases.

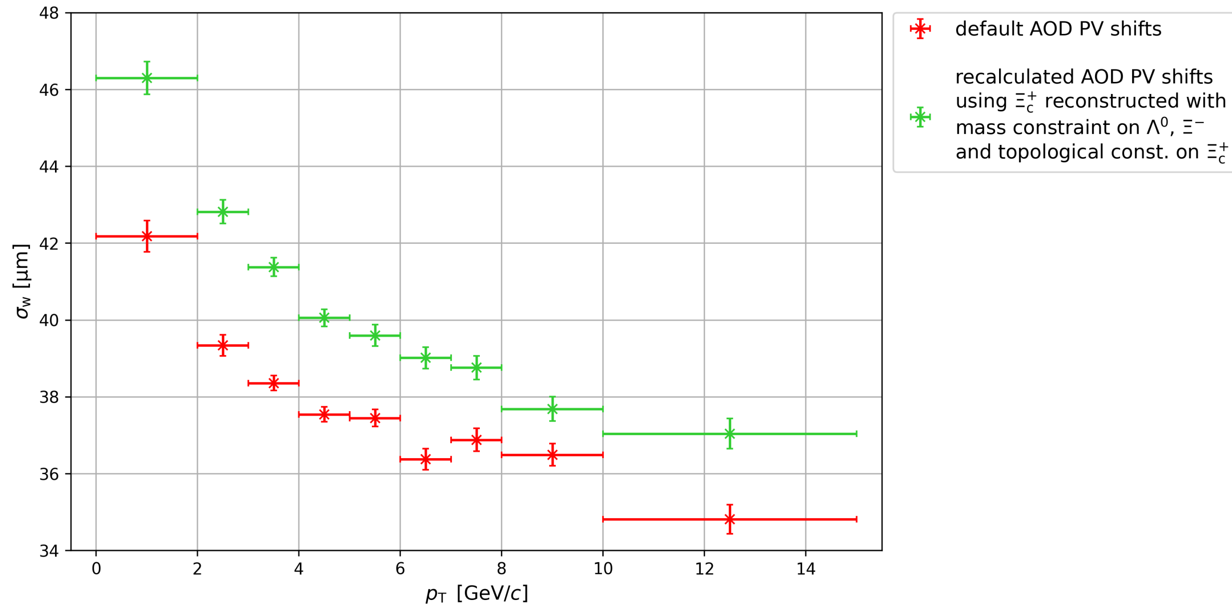

Figure 20: Standard deviation of the PV shifts obtained from double-Gaussian fits as a function of the transverse momentum of the Ξ_c^+ baryon.

6.4 Secondary vertex resolution

The secondary vertex resolution is analysed for all three coordinate axes. The discussion in this section is mainly restricted to the residual and pull distributions along the x-axis, i.e. transverse to the beamline. The corresponding analysis for the y- and z- axis can be found in the appendix.

In fig. 21 one can see that the mean value of the SV residuals is consistent with 0 within the uncertainties. For the cases 5 and 6 with the topological constraint on the Ξ^- to the PV, the mean values of the SV residual distribution are shifted systematically to larger negative values with increasing transverse momentum.. However, this trend is not observed for the SV residuals along the y- and z-axis (see fig. 34 and 34 in the appendix)

The width of the SV residual distribution for all different instances of the reconstructed Ξ_c^+ baryon is depicted in fig. 22. There is no significant difference in the SV resolution for the cases 0-3 in table 3. Therefore, applying successively the mass constraints on the Λ^0 and Ξ^- baryons and the topological constraint on the Ξ_c^+ to the PV does not change the width of the SV residual distribution compared to the case when no physical constraints are applied. However, applying the topological constraint on the Λ^0 baryon to the Ξ^- decay vertex yields a worse SV resolution for every p_T interval. This effect is compensated and the SV resolution is improved significantly with regards to all previous instances of the Ξ_c^+ baryon (cases 0-4) by adding the topological constraint of the Ξ^- baryon to the PV (cases 5-6). The width of the SV residuals decreases from approximately 250 μm averaged over all p_T intervals to approximately 200 μm for high transverse momentum and up to 100 μm for the low p_T intervals. Adding the topological constraint on the Ξ_c^+ to the PV (case 6 in table 3) leads to a slightly narrower SV residual distribution for every p_T interval compared to the case where only the topological constraint on the Ξ^- baryon is added (case 5 in table 3). Although the improvement is significant only for the low p_T intervals, the Ξ_c^+ reconstructed with all possible constraints applied seems to provide overall the best resolution of the SV.

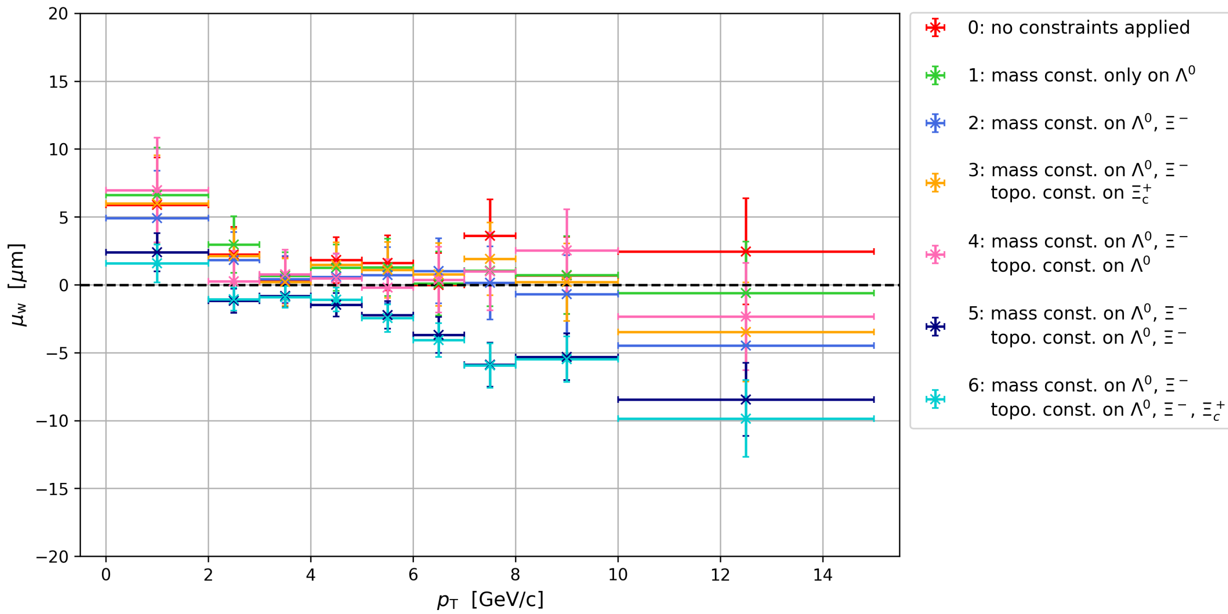

Figure 21: Weighted mean of the SV residual distribution along the x-axis obtained from triple-Gaussian fits as a function of the transverse momentum of the Ξ_c^+ baryon.

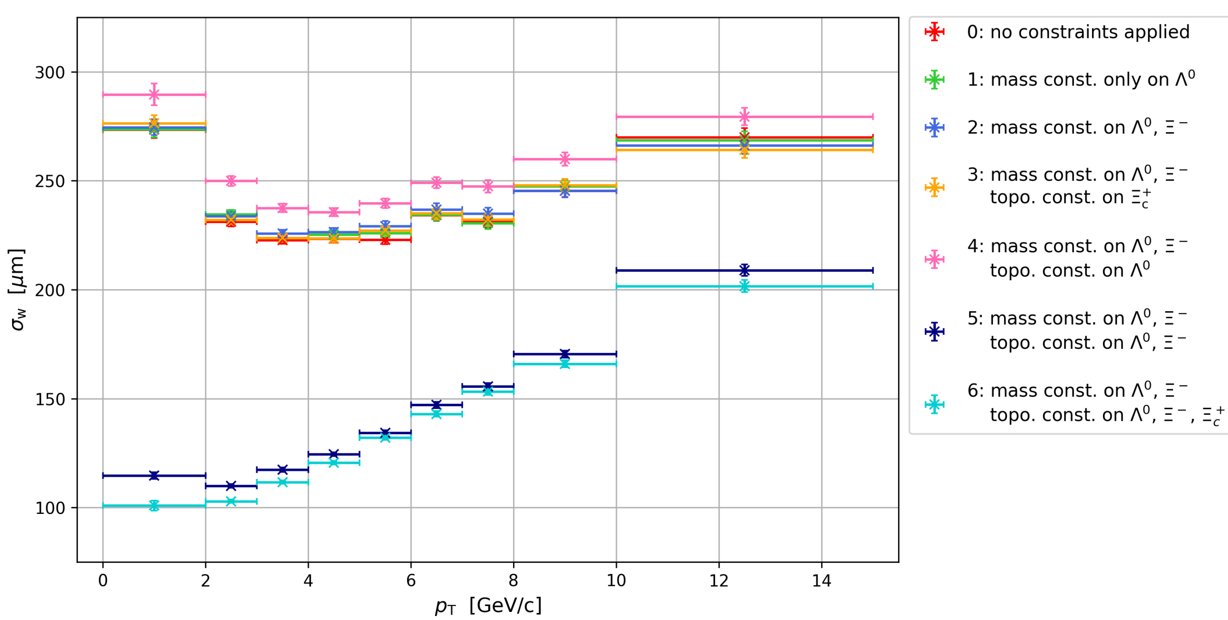

Figure 22: Weighted standard deviation of the SV residual distribution along the x-axis obtained from triple-Gaussian fits as a function of the transverse momentum of the Ξ_c^+ baryon.

The resolution of the SV decreases for low and high transverse momenta of the Ξ_c^+ baryon. On the one hand, the increase of the weighted standard deviation for high p_T is due to the fact that for higher momentum of the mother particle, the daughter particles themselves possess higher momenta and are therefore more boosted. As a result, the tracks of the daughter particles lie closer together in the laboratory frame and the region where their trajectories intersect within their uncertainties becomes larger leading to a poorer vertex resolution. For low transverse momenta of the mother particle on the other hand, the daughter particles themselves have lower momenta and are therefore more affected by multiple scattering. Thus, the uncertainties of the reconstructed decay vertex and track parameters of the mother particle increase due to the larger errors of the daughter tracks. This can be the case for the two pions originating directly from the decay of the Ξ_c^+, but is more likely for the other two pions and the proton further down the decay chain since they carry in total only the momentum of the Ξ^- baryon. By constraining the Ξ^- to the PV, its parameters are improved significantly and the decrease of the SV resolution is (almost) completely mitigated: For both instances of the Ξ_c^+ reconstructed with the topological constraint on the Ξ^- (case 5-6), the weighted standard deviation of the first p_T intervals increases slightly or remains approximately constant with regards to the medium p_T range (compare with fig. 35, 39).

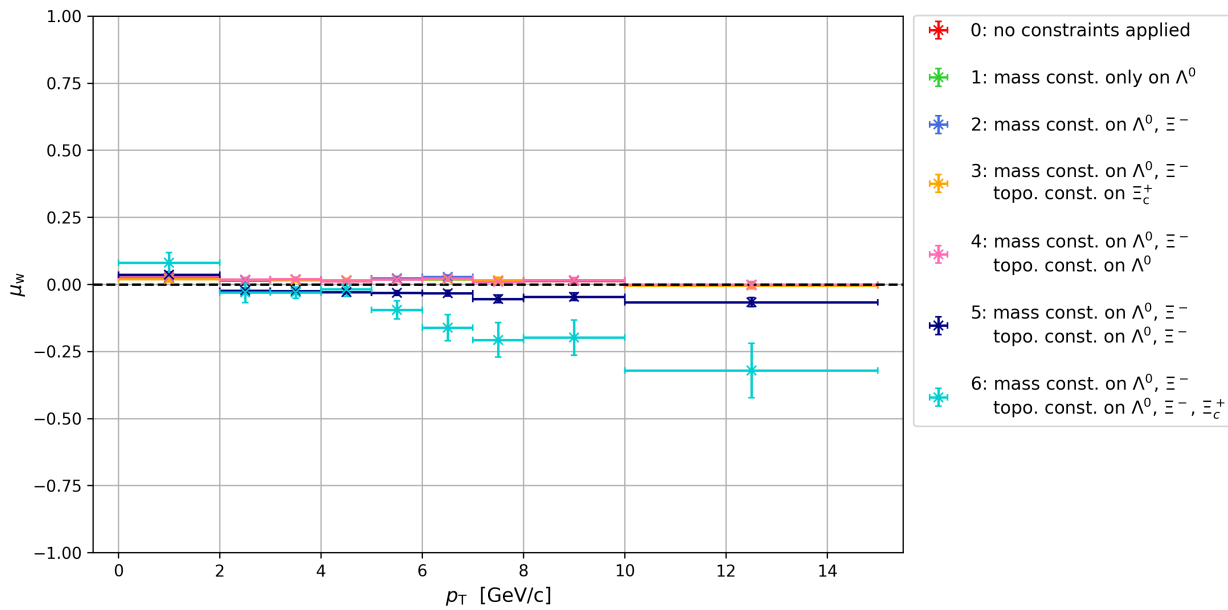

Figure 23: Weighted mean of the SV pull distribution along the x-axis as a function of the transverse momentum of the Ξ_c^+ baryon. A double-Gaussian fit function was used for the cases 0-5 and a triple-Gaussian fit function for case 6 in table 3.

The pull distributions of the cases 0-4 in table 3 follow a standard normal distribution, as their mean values are consistent with 0 (see fig. 23) and their standard deviation is consistent with 1 (see fig. 24). However, it can be concluded that for both cases with the topological constraint on the Ξ^- baryon (cases 5-6) the pull distributions do not follow a standard normal distribution: The mean values in fig. 23 are systematically shifted to negative values and deviate significantly from 0 for increasing transverse momentum. In addition to that, the weighted standard deviation increases in both cases for higher p_T. Thus, the uncertainty of the reconstructed SV position is underestimated. This is acceptable for case 5 as the width of the pull distribution increases only up to 1.4, but the deviation is not negligible for case 6 where the standard deviation of the pull distribution ranges from 3 up to 8 in fig. 24. The dramatic increase of the width of the pull distribution when adding the topological constraint on the Ξ_c^+ is probably caused by constraining both the Ξ^- and the Ξ_c^+ baryon to the PV, which is mathematically strictly speaking wrong. As a result, in order to improve the SV resolution significantly and estimate the errors as good as possible at the same time, case 5 in table 3 should be used for the reconstruction of the Ξ_c^+.

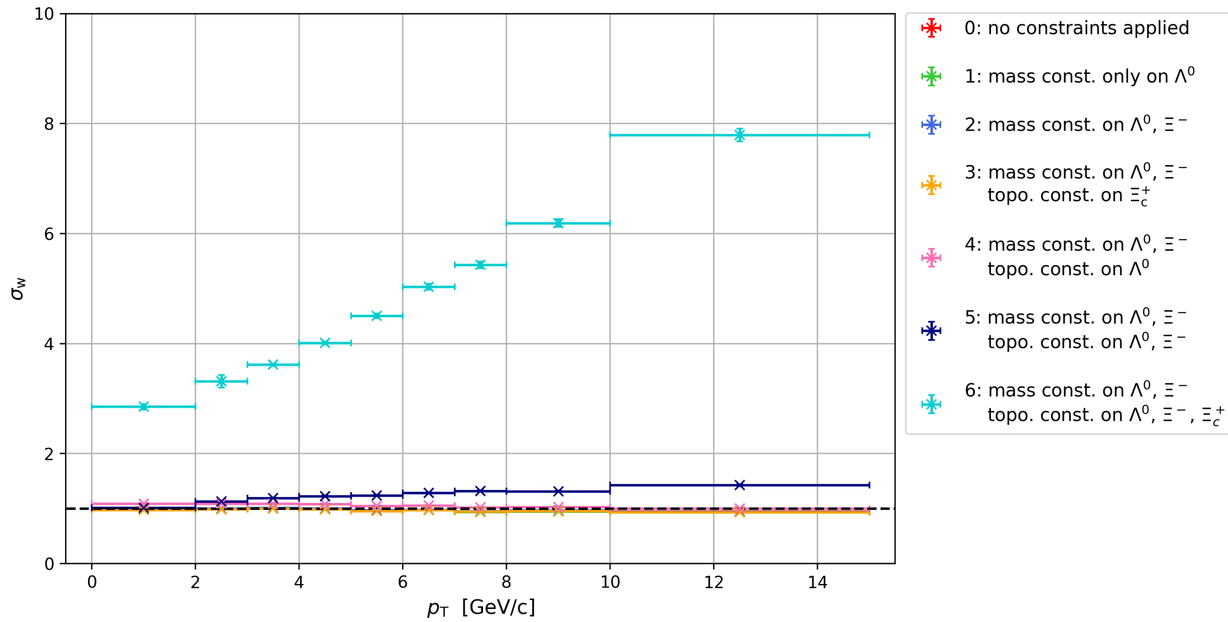

Figure 24: Weighted standard deviation of the SV pull distribution along the x-axis as a function of the transverse momentum of the Ξ_c^+ baryon. A double-Gaussian fit function was used for the cases 0-5 and a triple-Gaussian fit function for case 6 in table 3.

In figure 25 the SV resolution along the different coordinate axes is shown. As for the PV, the SV resolution is slightly better for the y-axis than for the x-axis. In contrast to the resolution of the AOD PV in minimum-bias and charm-enriched MC data, the SV resolution along the z-axis is better than for the x- and y-axis respectively.

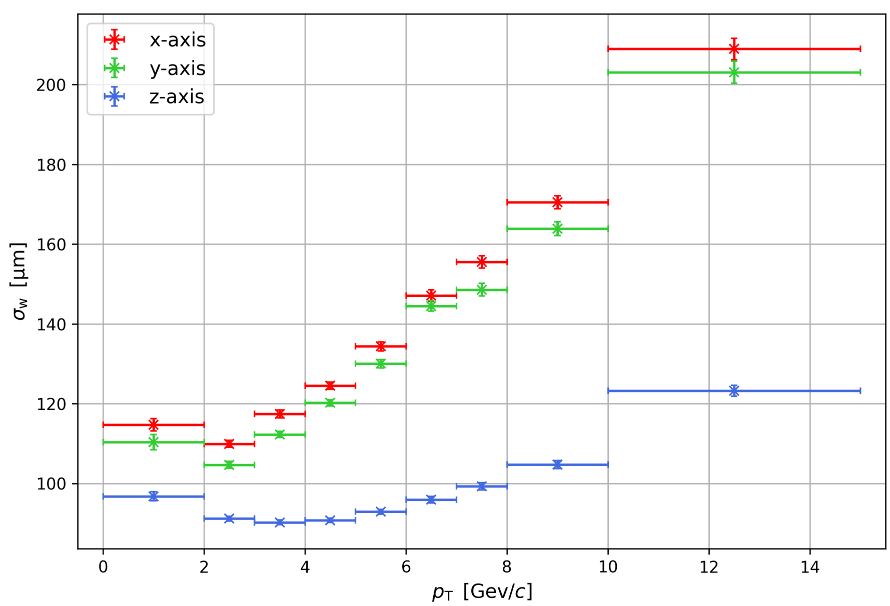

Figure 25: Comparison of the SV resolution for the different coordinate axes for the reconstructed Ξ_c^+ baryons corresponding to case 4 in table 3.

6.5 Mass resolution

When mass constraints on the Λ^0 and Ξ^- are applied, the FWHM of the mass distribution depicted in fig. 26 decreases and therefore the mass resolution of the Ξ_c^+ baryon improves. When the topological constraint on the Λ^0 to the decay vertex of the Ξ^- is added (case 4), the mass resolution decreases again compared to the case when only the mass constraints on both daughter particles are applied. On the contrary, additionally constraining the Ξ_c^+ baryon to the PV (case 3) results in further improvement of the mass resolution compared to all the cases where none or only mass constraints are applied (cases 0-2). The optimal mass resolution however is obtained when the Ξ^- is constrained to the PV. Since there is no difference between the cases 5 and 6 in fig. 26 apart from minor statistical fluctuations for two p_T intervals, the topological constraint on the Ξ^- appears to be the decisive contribution for the improvement of the mass resolution and the additional topological constraint on the Ξ_c^+ does not further impact its mass distribution. The uncertainties of the FWHM are basically constant over the entire p_T range as they are dominated by the (maximum) uncertainty of the Kielkopf approximation in eq. (57).

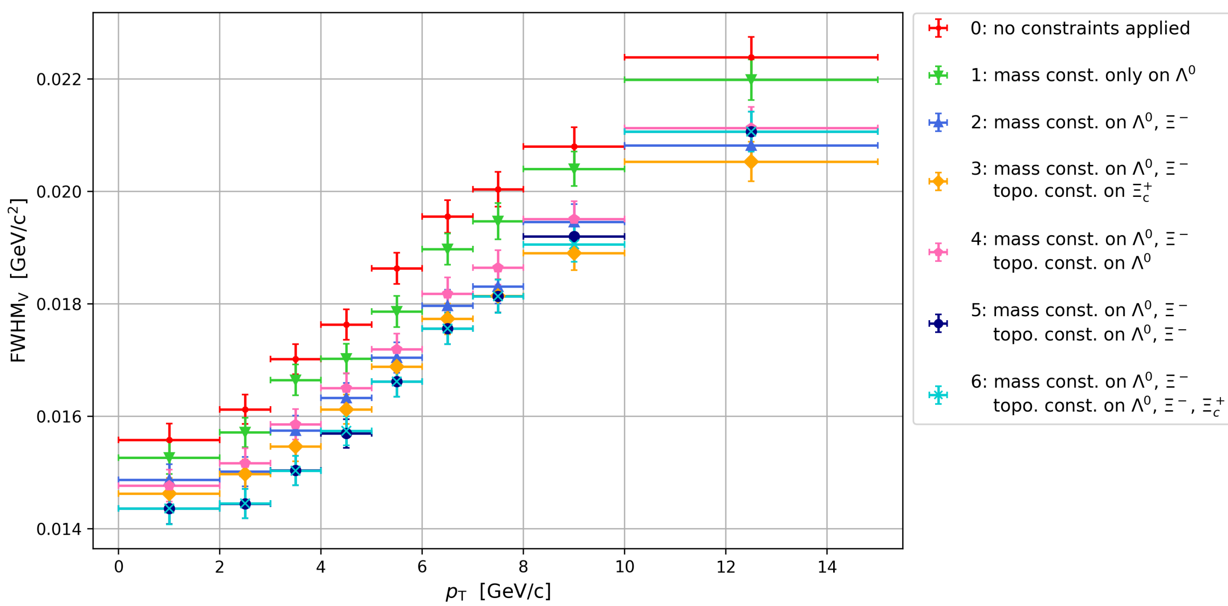

Figure 26: FWHM of the Voigt profile fitted to the mass distribution of the Ξ_c^+ baryon as a function of its transverse momentum.

The centre of the fitted Voigt profile μ_V shown in fig. 27 shifts systematically to lower mass values for the cases 1-4 compared to case 0. The centre of the Voigt profiles for the cases 5 and 6 are shifted significantly to lower mass values with respect to all other instances of the reconstructed Ξ_c^+ over the entire p_T range. The deviations of the centre of the Voigt profile for the cases 0-4 from the PDG measurement of the Ξ_c^+ mass are not significant since they lie within or overlap its the 3σ error band. However, the deviation is significant for the Ξ_c^+ baryons reconstructed with the topological constraint on the Ξ^-, cases 5 and 6, for the $2 \leq p_T < 3\,\mathrm{GeV}/c$ and $3 \leq p_T < 4\,\mathrm{GeV}/c$ intervals. All in all, μ_V has a similar p_T dependence for all cases of the reconstructed Ξ_c^+, but adding mass and topological constraints shifts the centre of the Voigt profile μ_V to lower mass values, especially when the Ξ^- baryon is constrained to the PV.

To sum up, the instance of the Ξ_c^+ corresponding to case 5 in table 3 provides the optimal mass resolution. In order to avoid introducing a significant shift with respect to the PDG mass, it might be preferable to use case 3 with the topological constraint on the Ξ_c^+ to the PV, for which the FWHM is only slightly larger.

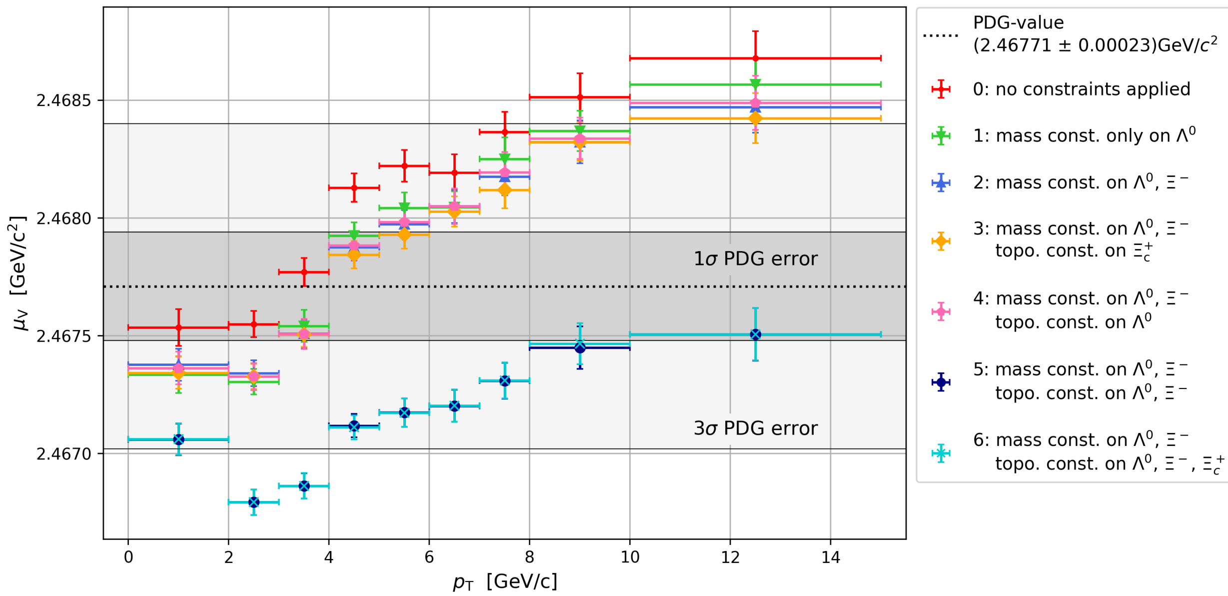

Figure 27: Centre of the Voigt profile μ_V fitted to the mass distribution of the Ξ_c^+ baryon as a function of its transverse momentum. The PDG value of the mass of the Ξ_c^+ baryon and the corresponding 1σ- and 3σ-error bands are indicated.

6.6 p_T-resolution

Since the uncertainty of the reconstructed transverse momentum of the Ξ_c^+ is not stored in the data sets, only the p_T-residual distribution is analysed in the following.

The mean values of the p_T residual distribution increase for higher transverse momentum for all different instances of the reconstructed Ξ_c^+ (see fig. 28) as expected according to eq. (6). As the mean values ranging from $+2\,\mathrm{MeV}/c$ to approximately $+10\,\mathrm{MeV}/c$ are always positive, the transverse momentum is on average slightly overestimated. The mean p_T residuals for the Ξ_c^+ baryons reconstructed with the topological constraint on the Ξ^-, cases 5 and 6, seem to be slightly increased for low p_T intervals. Looking at the ratio of the mean p_T residual with respect to the average for all different cases in each transverse momentum interval in fig. 29, this increase is however not statistically significant.

As for the mean values, the weighted standard deviation of the p_T-residual distribution in fig. 30 increases with increasing $p_{T,MC}$ as expected. Apart from statistical fluctuations for the first $p_{T,MC}$ interval with a small number of candidates, the p_T resolution is best for the Ξ_c^+ baryon reconstructed without any constraints over the entire p_T range. However, the transverse momentum resolution does not significantly differ for the other cases of the reconstructed Ξ_c^+ except for case 4, for which the width of the p_T residual distribution deviates significantly for large $p_{T,MC}$. Since case 4 with the topological constraint only applied on the Λ^0 has been identified as problematic before and will therefore not be recommended for the analysis, this is not concerning.

All in all, the transverse momentum distribution is not significantly affected by the application of mass an topological constraints. This can be motivated by the fact that the event kinematics do not change dramatically and the (transverse) momentum is mainly determined by the measured momentum of the long-lived daughter particles.

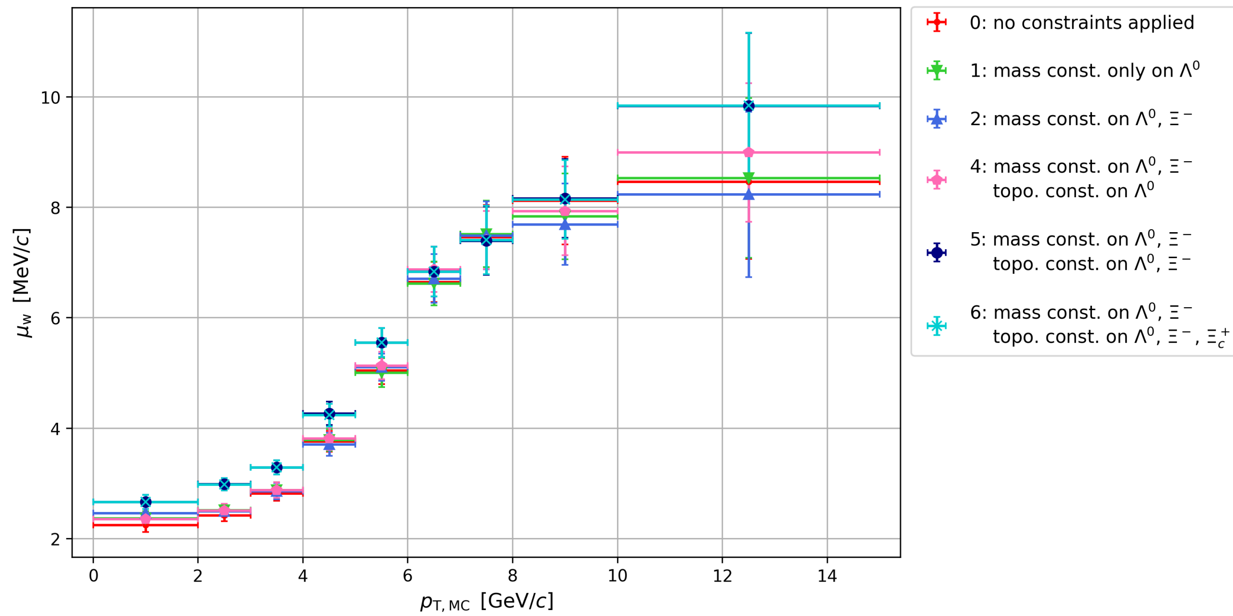

Figure 28: Weighted mean of the p_T-residual distribution obtained from a double-Gaussian fit as a function of the MC transverse momentum of the Ξ_c^+ baryon.

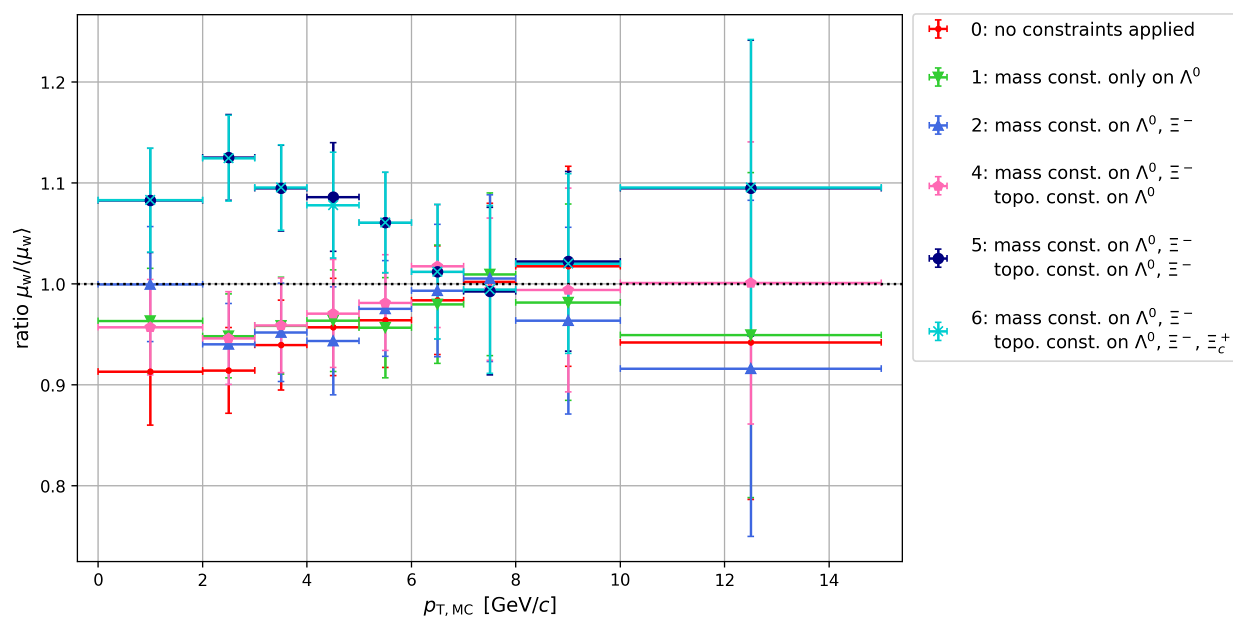

Figure 29: Weighted mean of the p_T-residual distribution normalised to the average of the weighted means of all different instances of the Ξ_c^+ for every bin.

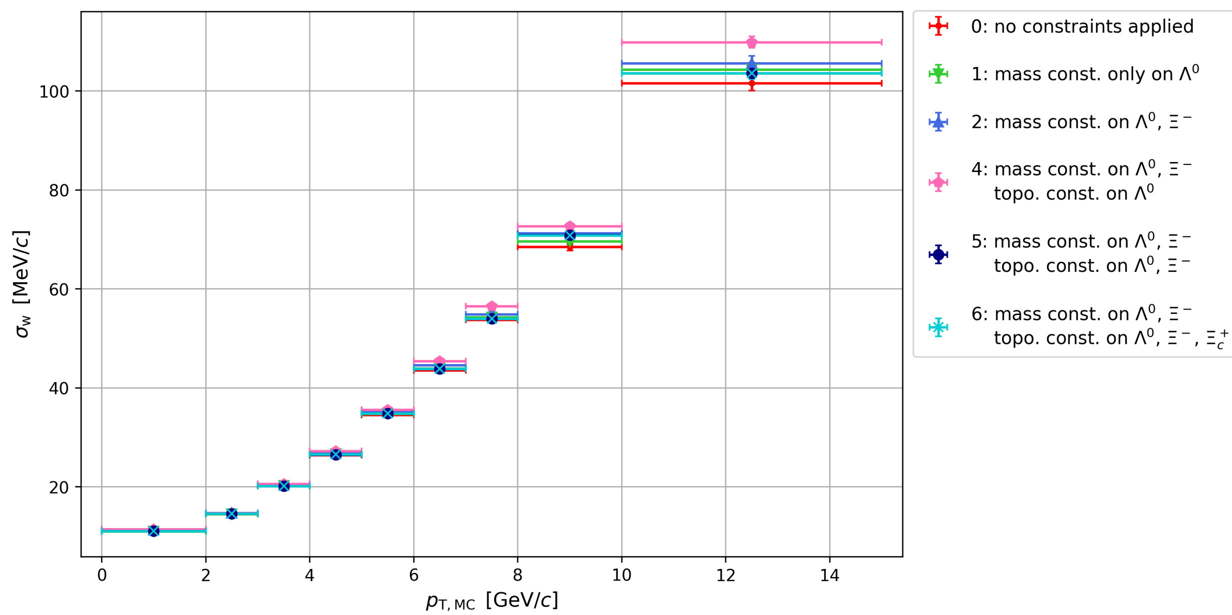

Figure 30: Weighted standard deviation of the p_T-residual distribution obtained from a double-Gaussian fit as a function of the MC transverse momentum of the Ξ_c^+ baryon.

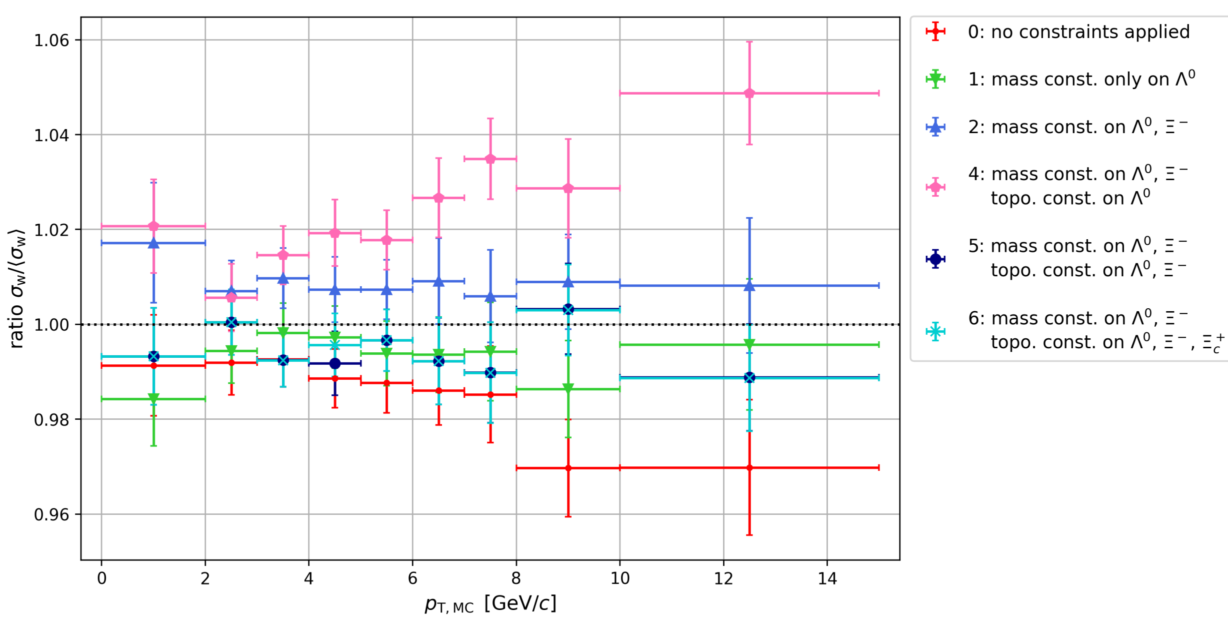

Figure 31: Weighted standard deviation of the p_T-residual distribution normalized to the average of the weighted standard deviations of all different instances of the Ξ_c^+ for every bin.

7 Conclusion and Outlook

In this thesis, the effects of applying mass and topological constraints in the reconstruction of a heavy-flavour hadron with the KF Particle package were investigated. Using Monte Carlo data for the decay of $\Xi_c^+ \to \Xi^-\pi^+\pi^+$ in pp-collisions at $\sqrt{s} = 13\,\text{TeV}$ in ALICE, the secondary vertex, mass and p_T resolution for different instances of the reconstructed Ξ_c^+ baryon were determined by comparing the reconstructed parameters to their corresponding Monte Carlo generated values. It was found that the reconstruction of the Ξ_c^+ baryon can be improved significantly with the KF Particle package by applying mass constraints on both short-lived daughter particles, the Λ^0 and Ξ^-, and by constraining the Ξ^- to the primary vertex.

In general, the transverse momentum resolution is not affected by applying mass and topological constraints since the event kinematics do not change overall. The mass constraints on the daughter particles Λ^0 and Ξ^- improve the mass resolution, but do not significantly change the secondary vertex resolution. The topological constraint applied on the Λ^0 to the decay vertex of the Ξ^- should not be applied at all since it always deteriorates the secondary vertex and mass resolution, even partly mitigating the improvement of previously applied mass constraints. This can be motivated by the fact that the decay vertex of the Ξ^- is fitted only from one directly measured particle, the π^-, and one reconstructed short-lived particle, the Λ^0. As the pion and the daughters of the Λ^0 are typically only measured up until the outer layers of the ITS, the track parameters especially of the Λ^0 are not as precise compared to primary tracks. Thus, the resolution of the decay vertex of the Ξ^- baryon is rather poor and a topological constraint to this vertex introduces an error in the reconstruction of the decay chain. This is also supported by the fact that only the application of the topological constraint on the Λ^0 significantly decreases the p_T resolution for high transverse momenta. On the contrary, the addition of the topological constraint on the Ξ^- to the primary vertex improves the secondary vertex resolution by a factor of up to 2.7 and results in an even better mass resolution. However, the Ξ^- and Ξ_c^+ baryons should not be constrained to the primary vertex simultaneously as the uncertainty of the secondary vertex is then dramatically underestimated while there is, apart from the secondary vertex resolution at low p_T, no significant improvement of the reconstructed parameters. Only adding the topological constraint on the Ξ_c^+ in addition to the mass constraints on both daughter particles does not improve the resolution of the secondary vertex as the lever arm, i.e. distance travelled in the laboratory frame, is too short. However, one obtains a mass resolution similar to the cases including the topological constraint on the Ξ^-, but without the significant shift to lower mass values. As a result, it might be preferable to use the instance of the Ξ_c^+ reconstructed with mass constraint on Λ^0 and Ξ^- and topological constraint on the Ξ_c^+ for precise mass measurements.

To sum up, topological constraints aligning a decayed mother particle to its production vertex should only be applied when the production vertex is known to a good precision and the lever arm is sufficiently long. If the distance travelled by the primary mother particle can not be resolved by the detector, its daughter particles should be constrained to the primary vertex instead. On the contrary, a mass constraint should generally be applied on all decayed daughter particles. This combination of constraints might then provide the desired increase of the signal-to-background ratio for low transverse momentum regions, very high track densities in heavy-ion collisions and extremely rare signals like multi-charm baryons with long decay chains (e.g. $\Xi_{cc}^{++} \to \Xi_c^+\pi^+$).

Using simulated minimum-bias triggered pp-collisions at $\sqrt{s} = 13\,\text{TeV}$ as reference, the resolution of the primary vertex obtained from the standard reconstruction employed in ALICE is found to be unaffected by the presence of the charmed hadron. The uncertainties of all primary vertex coordinates are slightly overestimated. In contrast to the expectation of cylindrical symmetry, the resolution of the primary vertex is systematically different for the x- and y-axis. However, this might be a specific feature of the Monte Carlo samples used in this analysis and is subject to further verification with other simulations. Furthermore, the reconstructed primary vertex coordinates are intrinsically biased in the order of a few microns, which is negligible with regards to the detector resolution. The KF Particle package was used to recalculate the primary vertex obtained from the standard reconstruction in ALICE by adding the Ξ_c^+ baryon as a measurement and removing its daughter particles from the vertex fit. Thus, it could be tested whether the primary vertex is systematically biased in the direction of the charmed hadron, as its daughter particles might contribute to the primary vertex fit. However, no clear evidence of a primary vertex shift caused by the daughter particles of the Ξ_c^+ baryon is found. Nevertheless, this analysis can be improved by taking the number of removed daughter particles and different instances of the reconstructed Ξ_c^+ into account.

Instead of using the primary vertex from the standard ALICE reconstruction, it could also be refitted with the KF Particle package using directly the track estimates and the beam position as an additional constraint. Although the primary vertex resolution is not expected to improve drastically, the refitted primary vertex might provide an unbiased vertex position with properly estimated uncertainties.

Appendix

A.1 Uncertainty of the weighted parameters of a triple-Gaussian distribution

The uncertainty for the weighted standard deviation of a triple-Gaussian is calculated in the following way:

$$
\begin{aligned}
s_3 &= A_1 + A_2 + A_3 \\
w_3 &= A_1\sigma_1 + A_2\sigma_2 + A_3\sigma_3 \\
s_3^4 \cdot \left(\Delta\sigma_w^{\mathrm{TG}}\right)^2 &= (\Delta A_1)^2 \cdot [A_2 \cdot (\sigma_1 - \sigma_2) + A_3 \cdot (\sigma_1 - \sigma_3)]^2 \\
&+ (\Delta A_2)^2 \cdot [A_1 \cdot (\sigma_1 - \sigma_2) + A_3 \cdot (\sigma_3 - \sigma_2)]^2 \\
&+ (\Delta A_3)^2 \cdot [A_1 \cdot (\sigma_1 - \sigma_3) + A_2 \cdot (\sigma_2 - \sigma_3)]^2 \\
&+ 2\ \mathrm{cov}(A_1, A_2) \cdot [w_3 - s_3 \cdot \sigma_1] \cdot [w_3 - s_3 \cdot \sigma_2] \\
&+ 2\ \mathrm{cov}(A_1, A_3) \cdot [w_3 - s_3 \cdot \sigma_1] \cdot [w_3 - s_3 \cdot \sigma_3] \\
&+ 2\ \mathrm{cov}(A_2, A_3) \cdot [w_3 - s_3 \cdot \sigma_2] \cdot [w_3 - s_3 \cdot \sigma_3] \\
&+ s_3^2 \cdot \big[(A_1 \cdot \Delta\sigma_1)^2 + (A_2 \cdot \Delta\sigma_2)^2 + (A_3 \cdot \Delta\sigma_3)^2 \\
&\qquad + 2A_1A_2 \cdot \mathrm{cov}(\sigma_1, \sigma_2) + 2A_1A_3 \cdot \mathrm{cov}(\sigma_1, \sigma_3) + 2A_2A_3 \cdot \mathrm{cov}(\sigma_2, \sigma_3)\big] \\
&- 2s_3 \cdot \Big\{\ A_1 \cdot \big[\mathrm{cov}(A_1, \sigma_1) \cdot (w_3 - s_3 \cdot \sigma_1) + \mathrm{cov}(A_2, \sigma_1) \cdot (w_3 - s_3 \cdot \sigma_2) \\
&\qquad\qquad + \mathrm{cov}(A_3, \sigma_1) \cdot (w_3 - s_3 \cdot \sigma_3)\big] \\
&\qquad + A_2 \cdot \big[\mathrm{cov}(A_1, \sigma_2) \cdot (w_3 - s_3 \cdot \sigma_1) + \mathrm{cov}(A_2, \sigma_2) \cdot (w_3 - s_3 \cdot \sigma_2) \\
&\qquad\qquad + \mathrm{cov}(A_3, \sigma_2) \cdot (w_3 - s_3 \cdot \sigma_3)\big] \\
&\qquad + A_3 \cdot \big[\mathrm{cov}(A_1, \sigma_3) \cdot (w_3 - s_3 \cdot \sigma_1) + \mathrm{cov}(A_2, \sigma_3) \cdot (w_3 - s_3 \cdot \sigma_2) \\
&\qquad\qquad + \mathrm{cov}(A_3, \sigma_3) \cdot (w_3 - s_3 \cdot \sigma_3)\big]\Big\}
\end{aligned}
\tag{59}
$$

The error for the weighted mean is calculated by replacing $\sigma_i \leftrightarrow \mu_i$.

A.2 Fits vs. numerical estimators

Instead of using multi-Gaussian fits, the mean μ and standard deviation σ of the residual and pull distributions under consideration could also be determined with their corresponding maximum likelihood estimators. For n measurements of a variable x distributed according to a Gaussian with average μ and standard deviation σ, the maximum likelihood estimate for the mean $\hat{\mu}$ and its uncertainty $\sigma_{\hat{\mu}}$ are given by:

$$
\begin{aligned}
\hat{\mu} &= \frac{1}{n}\sum_{i=1}^{n} x_i \\
\sigma_{\hat{\mu}} &= \frac{\sigma}{\sqrt{n}}
\end{aligned}
\tag{60}
$$

The maximum likelihood estimator for the Gaussian variance

$$
\hat{\sigma^2} = \frac{1}{n}\sum_{i=1}^{n}(x_i - \hat{\mu})^2 \tag{61}
$$

tends to underestimate the variance and therefore the unbiased estimate is obtained by applying the following correction:

$$
\hat{\sigma^2}_{\text{unbiased}} = \frac{n}{n-1} \cdot \hat{\sigma^2} = \frac{1}{n-1} \cdot \sum_{i=1}^{n}(x_i - \hat{\mu})^2 \tag{62}
$$

An estimator for the standard deviation is obtained by taking the square root of eq. (62) [4].

However, the estimator of the standard deviation of the SV residuals in fig. 33 provides up to 20% larger values than the weighted standard deviation calculated from a triple-Gaussian fit. This is due to the fact that the underlying distribution is rather a superposition of three individual Gaussian distributions centred around zero and the single-Gaussian assumption does not hold: Approximately a quarter of candidates is associated to a Gaussian distribution with a standard deviation of $\sigma = 50\,\mu$m and half of the candidates to one with $\sigma = 124\,\mu$m. Only another quarter of the candidates is associated to a Gaussian distribution with a standard deviation of $\sigma = 246\,\mu$m which is larger than the weighted standard deviation (see fig. 32). Therefore, the candidates associated to this Gaussian contribution distort the estimator.

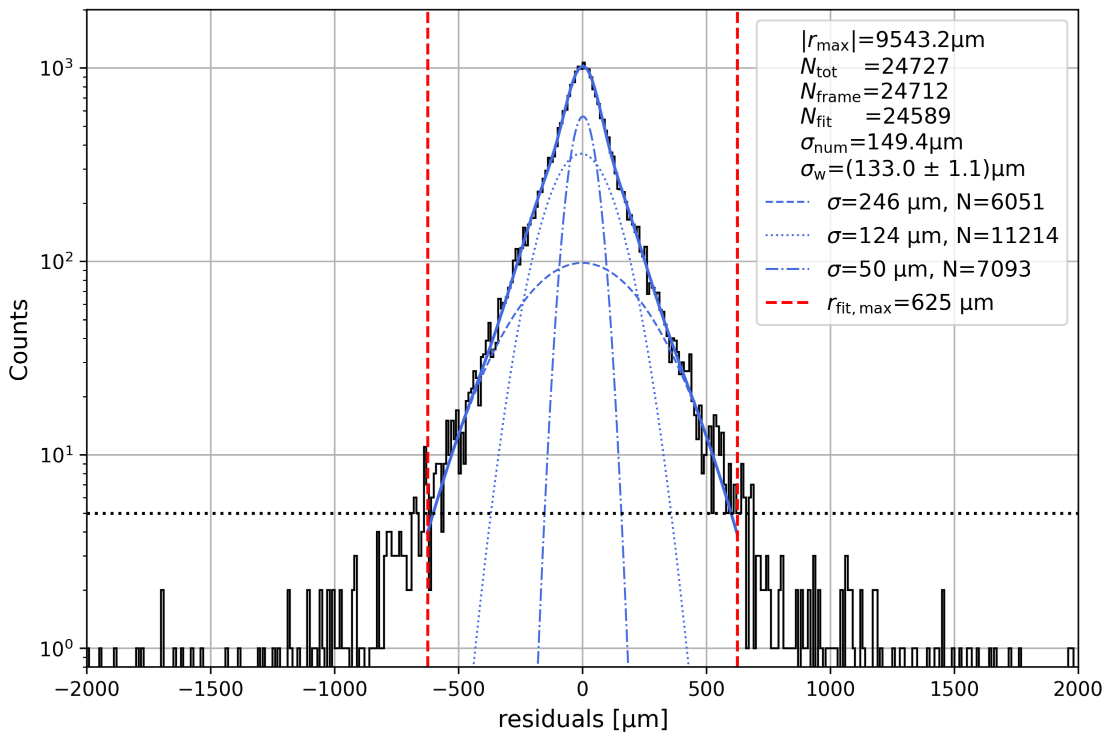

Figure 32: SV residual distribution of reconstructed Ξ_c^+ baryons corresponding to case 5 in table 3 with transverse momentum $5 \leq p_T < 6\,\mathrm{GeV}/c$. There are in total $N_{\mathrm{tot}} = 24.727$ candidates stored for this particular case and p_T-bin with SV residuals of up to $|r_{\max}| \approx 9.5\,\mathrm{mm}$, from which $N_{\mathrm{frame}} = 24.727$ candidates are visible in the plotted range of the residuals. A triple-Gaussian function was fitted to the histogram for residuals up to $|r_{\mathrm{fit,max}}| = 625\,\mu$m. The value of the numerical estimator of the standard deviation $\sigma_{\mathrm{num}} = 149.4\,\mu$m is approximately 10% larger than the weighted standard deviation $\sigma_w = 133.0\,\mu$m obtained from the triple-Gaussian fit. The number of events N and standard deviation σ associated to each single Gaussian from the triple-Gaussian fit function is given in the legend.

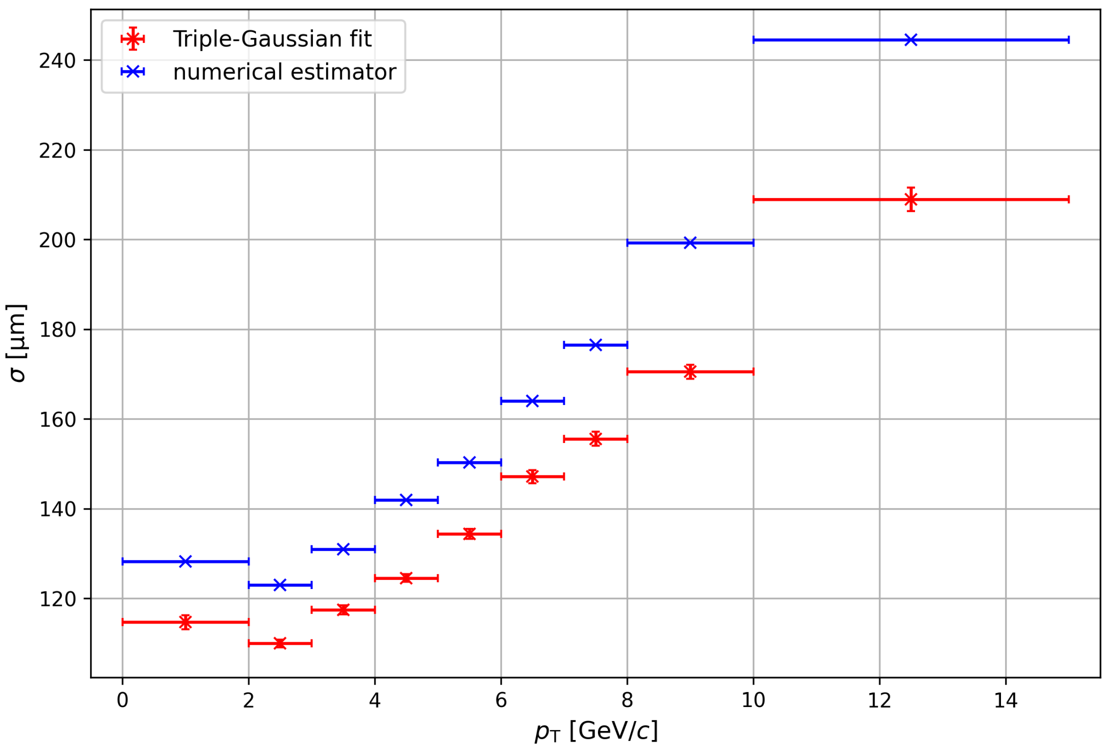

Figure 33: Comparison of the values for the standard deviation of the SV residuals along the x-axis obtained from a triple-Gaussian fit and from the numerical estimator for the instance of the Ξ_c^+ baryon corresponding to case 5 in table 3.

A.3 Parameters of the SV residual and pull distribution in y- and z-direction

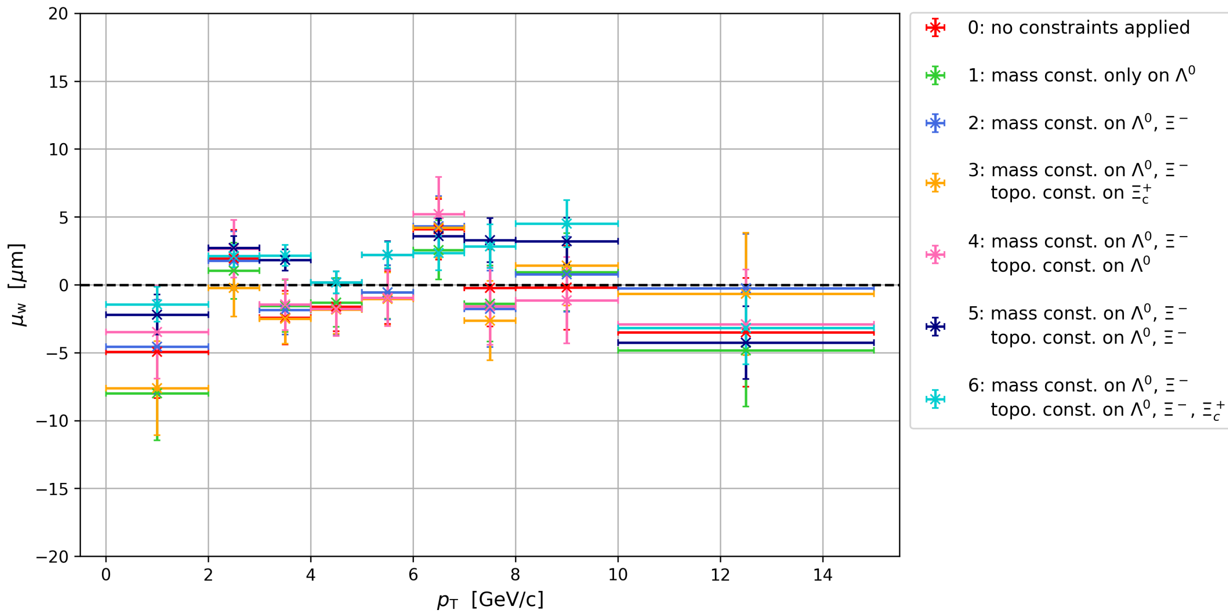

Figure 34: Weighted mean of the SV residual distribution along the y-axis obtained from triple-Gaussian fits as a function of the transverse momentum of the Ξ_c^+ baryon.

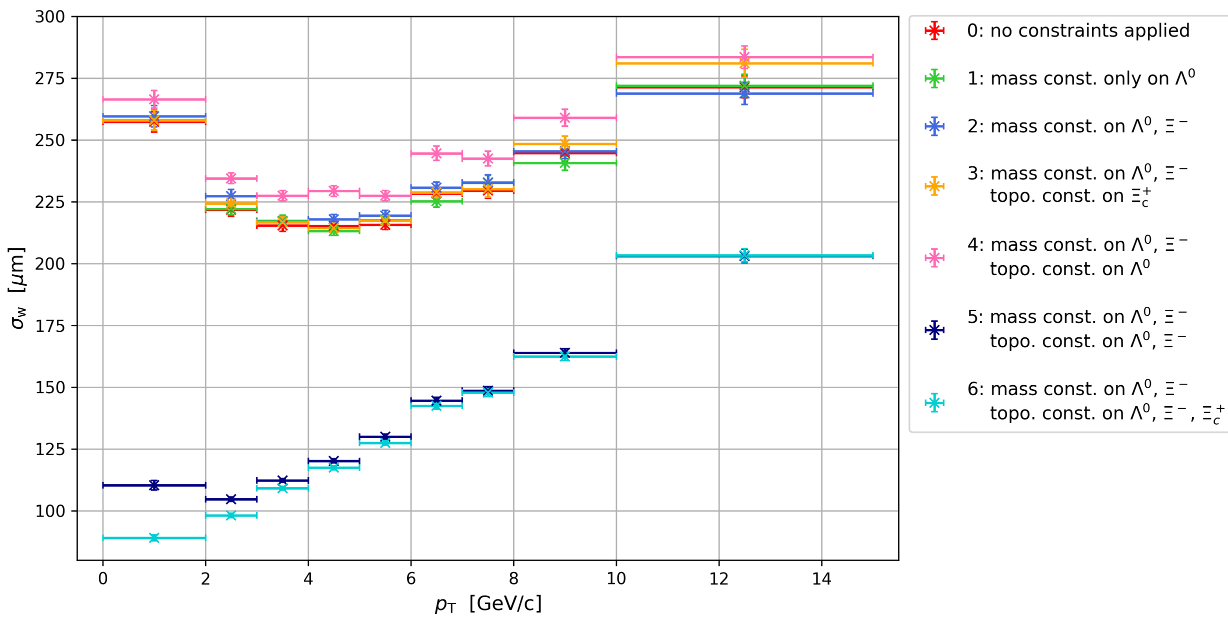

Figure 35: Weighted standard deviation of the SV residual distribution along the y-axis obtained from triple-Gaussian fits as a function of the transverse momentum of the Ξ_c^+ baryon.

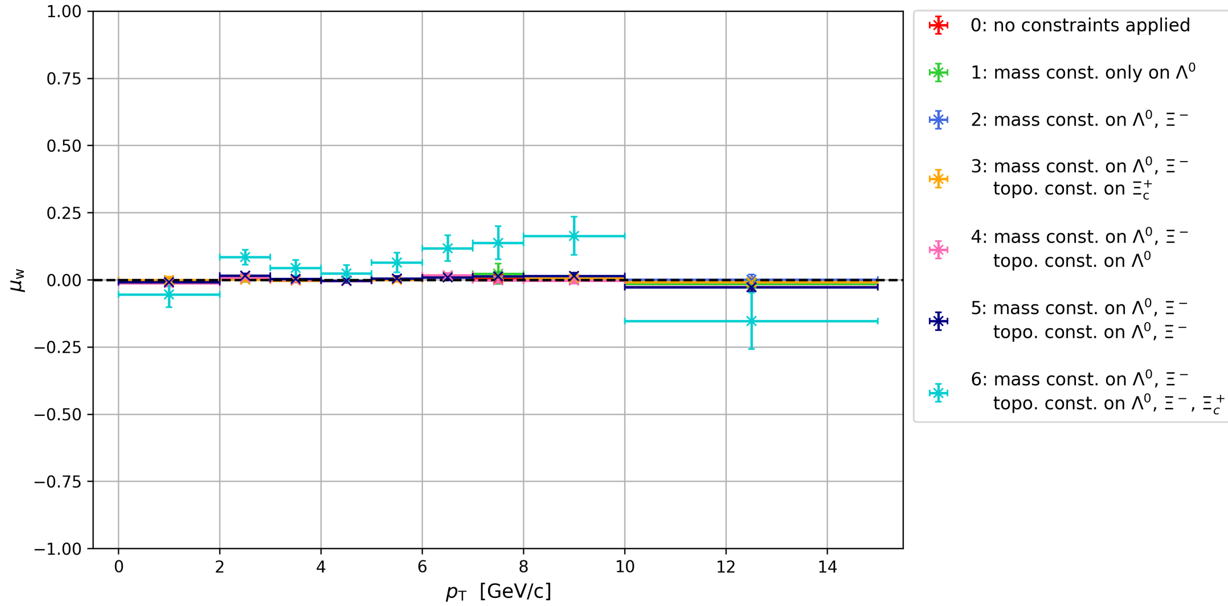

Figure 36: Weighted mean of the SV pull distribution along the y-axis as a function of the transverse momentum of the Ξ_c^+ baryon. A double-Gaussian fit function was used for the cases 0-5 and a triple-Gaussian fit function for case 6 in table 3.

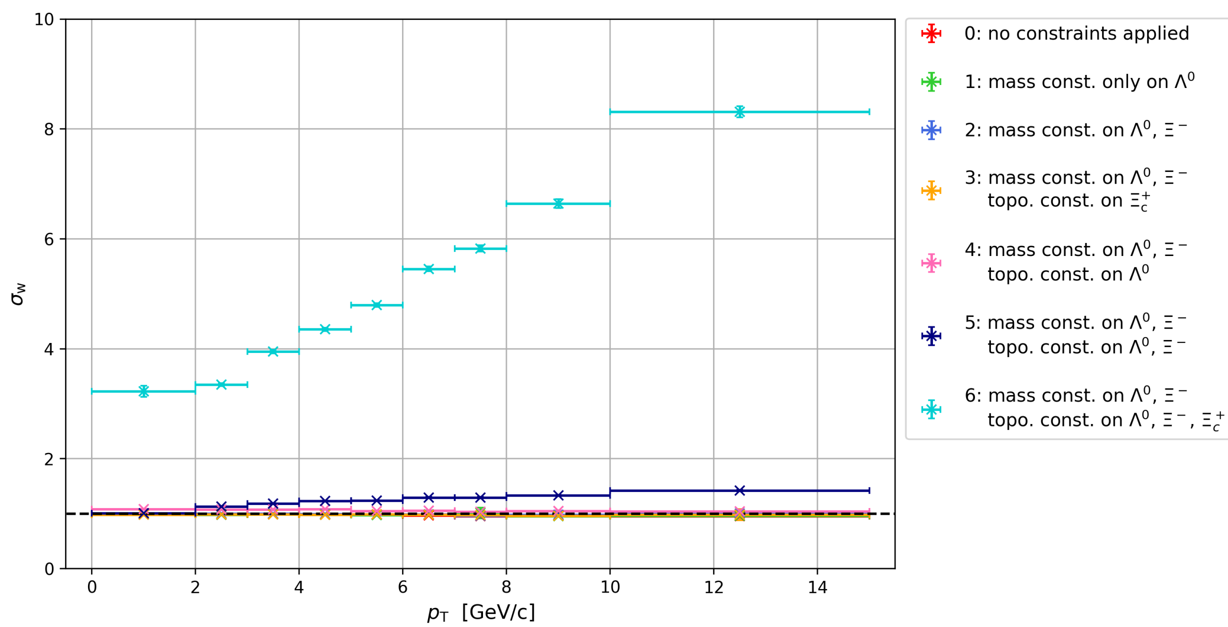

Figure 37: Weighted standard deviation of the SV pull distribution along the y-axis as a function of the transverse momentum of the Ξ_c^+ baryon. A double-Gaussian fit function was used for the cases 0-5 and a triple-Gaussian fit function for case 6 in table 3.

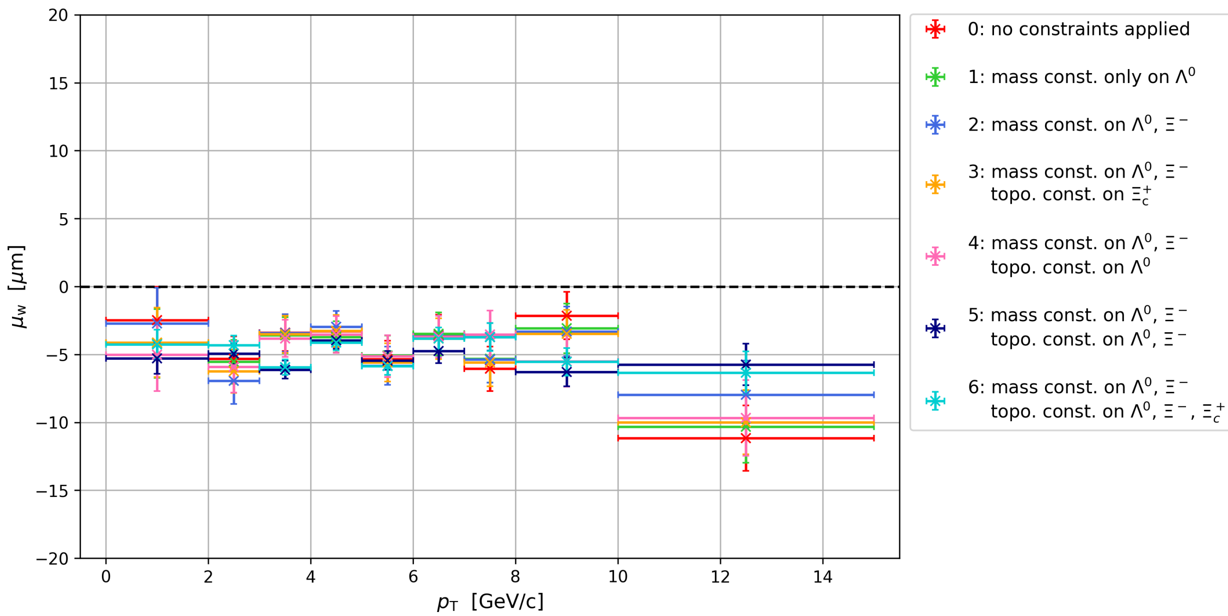

Figure 38: Weighted mean of the SV residual distribution along the z-axis obtained from double-Gaussian fits as a function of the transverse momentum of the Ξ_c^+ baryon.

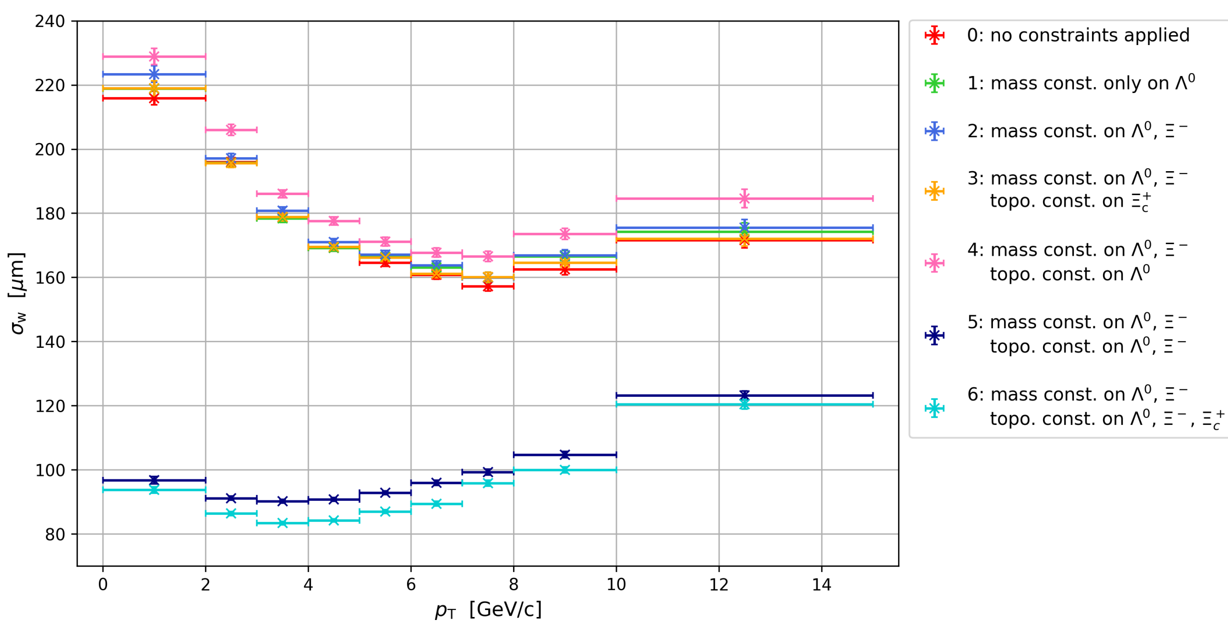

Figure 39: Weighted standard deviation of the SV residual distribution along the z-axis obtained from double-Gaussian fits as a function of the transverse momentum of the Ξ_c^+ baryon.

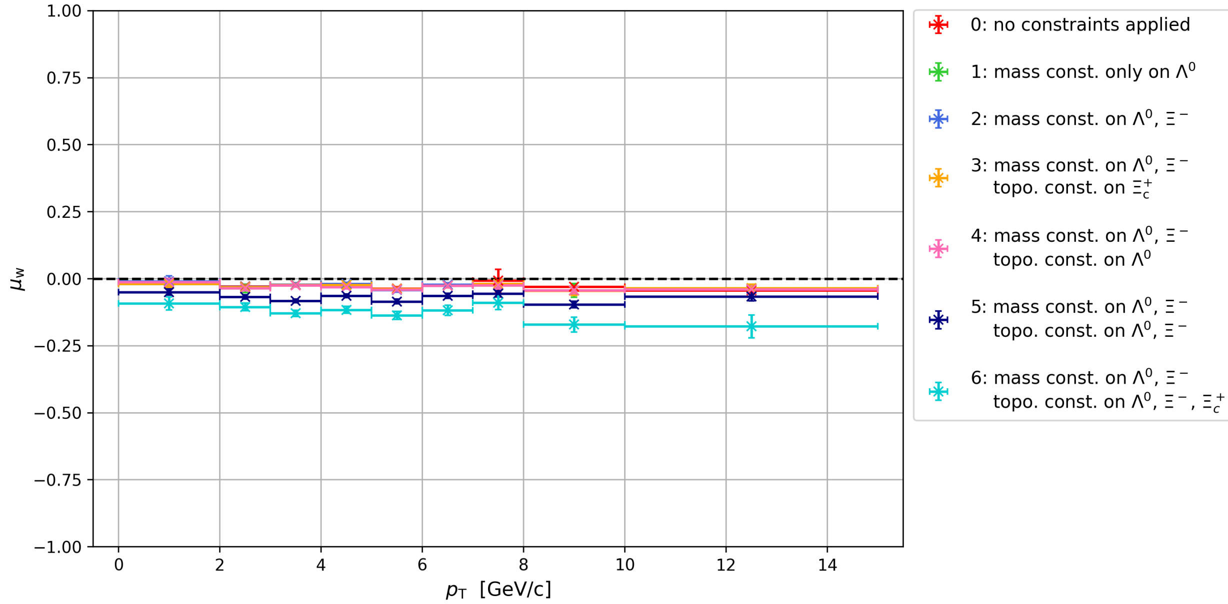

Figure 40: Weighted mean of the SV pull distribution along the z-axis obtained from double-Gaussian fits as a function of the transverse momentum of the Ξ_c^+ baryon.

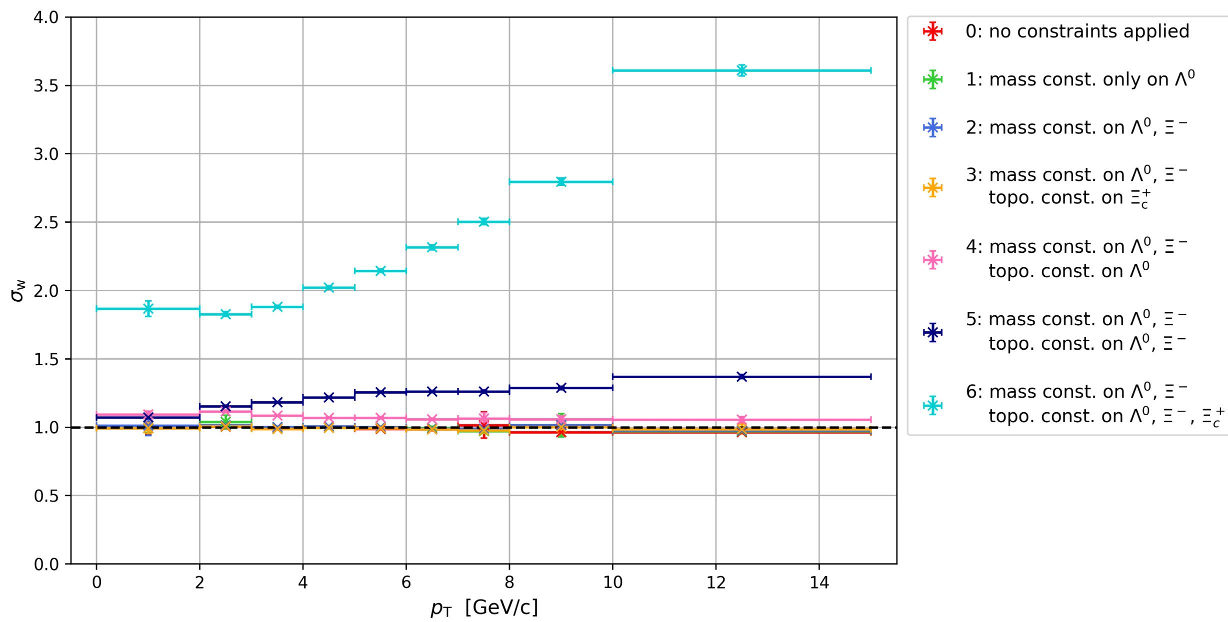

Figure 41: Weighted standard deviation of the SV pull distribution along the z-axis obtained from double-Gaussian fits as a function of the transverse momentum of the Ξ_c^+ baryon.

References

[1] The ALICE Collaboration. "The ALICE experiment at the CERN LHC". In: *Journal of Instrumentation* 3.08 (Aug. 2008), S08002. DOI: 10.1088/1748-0221/3/08/S08002. URL: https://dx.doi.org/10.1088/1748-0221/3/08/S08002.

[2] Sergey Gorbunov. "On-line reconstruction algorithms for the CBM and ALICE experiments". doctoralthesis. Universitätsbibliothek Johann Christian Senckenberg, 2013, pp. 104, 9.

[3] Hermann Kolanoski and Norbert Wermes. "373Track reconstruction and momentum measurement". In: *Particle Detectors: Fundamentals and Applications*. Oxford University Press, June 2020. ISBN: 9780198858362. DOI: 10.1093/oso/9780198858362.003.0009. eprint: https://academic.oup.com/book/0/chapter/365034718/chapter-pdf/50271257/oso-9780198858362-chapter-9.pdf. URL: https://doi.org/10.1093/oso/9780198858362.003.0009.

[4] Luca Lista. *Statistical Methods for Data Analysis in Particle Physics*. 2nd ed. Vol. 941. Lecture Notes in Physics. Springer Cham. DOI: https://doi.org/10.1007/978-3-319-62840-0.

[5] J.J. Olivero and R.L. Longbothum. "Empirical fits to the Voigt line width: A brief review". In: *Journal of Quantitative Spectroscopy and Radiative Transfer* 17.2 (1977), pp. 233–236. ISSN: 0022-4073. DOI: https://doi.org/10.1016/0022-4073(77)90161-3. URL: https://www.sciencedirect.com/science/article/pii/0022407377901613.

[6] "Performance of the ALICE experiment at the CERN LHC". In: *International Journal of Modern Physics A* 29.24 (2014), p. 1430044. DOI: 10.1142/S0217751X14300440. eprint: https://doi.org/10.1142/S0217751X14300440. URL: https://doi.org/10.1142/S0217751X14300440.

[7] Carolina Reetz. "Measurement of Ξ_c^+ in proton–proton collisions at $\sqrt{s} = 13\,\mathrm{TeV}$ with the ALICE detector". masterthesis. Department of Physics and Astronomy, University of Heidelberg, 2022. URL: https://www.physi.uni-heidelberg.de/Publications/MasterThesis_CarolinaReetz_wo.pdf.

[8] Carolina Reetz. "Reconstruction of the Hadronic Decay of the Ξ^0_c Baryon with the ALICE Detector – Investigation of Charm Production and Validation of the KF Particle Package". bachelorthesis. Department of Physics and Astronomy, University of Heidelberg, 2019. URL: https://www.physi.uni-heidelberg.de//Publications/BachelorThesis_CarolinaReetz.pdf.

[9] F. Schreier. "The Voigt and complex error function: A comparison of computational methods". In: *Journal of Quantitative Spectroscopy and Radiative Transfer* 48.5 (1992). Special Issue Conference on Molecular Spectroscopic Databases, pp. 743–762. ISSN: 0022-4073. DOI: https://doi.org/10.1016/0022-4073(92)90139-U. URL: https://www.sciencedirect.com/science/article/pii/002240739290139U.

[10] Kyrre Skjerdal and (forthe ALICE collaboration). "Photoproduction of ρ^0 in ultra–peripheral nuclear collisions at ALICE". In: *Journal of Physics: Conference Series* 455.1 (Aug. 2013), p. 012010. DOI: 10.1088/1742-6596/455/1/012010. URL: https://dx.doi.org/10.1088/1742-6596/455/1/012010.

[11] R. L. Workman et al. "Review of Particle Physics". In: *PTEP* 2022 (2022), p. 083C01. DOI: 10.1093/ptep/ptac097.

[12] Maksym Zyzak. “Online selection of short-lived particles on many-core computer architectures in the CBM experiment at FAIR”. doctoralthesis. Universitätsbibliothek Johann Christian Senckenberg, 2016, p. 165.

Declaration of authorship

Ich versichere, dass ich diese Arbeit selbstständig verfasst und keine anderen als die angegebenen Quellen und Hilfsmittel benutzt habe.

Heidelberg, den 12.06.2023.

Acknowledgements

I want to thank Prof. Dr. Silvia Masciocchi for her excellent supervision and especially for enabling me to present the results of my bachelor thesis at the SMuK23 conference of the Deutsche Physikalische Gesellschaft (DPG) in Dresden, March 2023. Special thanks go to Carolina Reetz for her great support throughout the entire course of my thesis. I also want to thank Jianhui Zhu in particular, who implemented the KF Particle package in the analysis task used for the reconstruction of the MC data. Without his continuous updates of this analysis task in the scope of this thesis, my work would not have been possible. Finally, I want to thank Andrea Dubla for proofreading my thesis.